Bergische Universität Wuppertal

Fakultät für Elektrotechnik, Informationstechnik und Medientechnik

Semitransparent Electrodes for Opto-Electronic Device Applications

zur Erlangung des akademischen Grades eines Doktors der Ingenieurwissenschaften (Dr.-Ing.) eingereichte

Dissertation

von M.Sc. Tobias Gahlmann

Chair of electronic devices

Erstgutachter: Prof. Dr. rer. nat. Thomas Riedl
Zweitgutachter: Prof. Dr.-Ing. Patrick Görrn

Eingereicht am: 22.10.2021
Mündliche Prüfung am: 28.01.2022

The PhD thesis can be quoted as follows:

urn:nbn:de:hbz:468-20220317-104029-4
[http://nbn-resolving.de/urn/resolver.pl?urn=urn%3Anbn%3Ade%3Ahbz%3A468-20220317-104029-4]

DOI: 10.25926/b38v-0r73
[https://doi.org/10.25926/b38v-0r73]

Vorwort/Preface

Die vorliegende Arbeit entstand im Rahmen einer Tätigkeit als wissenschaftlicher Mitarbeiter am *Lehrstuhl für elektronische Bauelemente* an der Bergischen Universität Wuppertal. Die Arbeit basiert in Teilen auf den Projektinhalten zum BMBF-Projekt *EPOS*, der ZIM Projekte *Transparente und leitfähige Elektroden auf Basis metallischer Nanodrähte für Elektrolumineszenz-Folien* und *Innovative Bauelementarchitekturen für effiziente und vielseitig einsetzbare Elektrolumineszenz-Folien.* Darüber hinaus sind Teile dieser Arbeit im Vorfeld in wissenschaftlichen Veröffentlichungen sowie auf internationalen Konferenzen präsentiert worden.

An erste Stelle möchte ich meinem Doktorvater Prof. Dr. rer. nat. Thomas Riedl für die Möglichkeit zur Anfertigung dieser Dissertation danken. Erst durch seine fachliche Betreuung sowie seiner wertvollen Ratschläge war es möglich, die wissenschaftlichen Veröffentlichungen und letztendlich diese Dissertation abzuschließen. Vielen Dank! Prof. Dr.-Ing. Patrick Görrn danke ich für die Übernahme des Korreferats und die Anfertigung des Gutachtens. Ein besonderer Dank gilt allen aktuellen und ehemaligen Mitarbeitern des Lehrstuhls für die konstruktive und fruchtbare Zusammenarbeit in den letzten Jahren und das angenehme Arbeitsumfeld. Namentlich zu nennen sind hierbei Herr Dr. Detlef Theirich und Herr Dr. Andreas Behrendt, welche mich während des Studiums für eine Mitarbeit an diesem Lehrstuhl motivierten und damit die Grundlage für meine wissenschaftlichen Arbeiten am Lehrstuhl legten. Andreas Behrendt danke ich darüber hinaus für die hervorragende Betreuung während meiner Bachelor- und Masterarbeit und die damit verbundende Anleitung zum wissenschaftlichem Arbeiten. Weiterhin bedanken möchte ich mich bei Kai Brinkmann für die intensive Zusammenarbeit bei der Arbeit an perovskitbasierten Solarzellen und den damit verbundenen Ergebnissen. Ebenfalls danken möchte ich Herrn Dr. Ralf Heiderhoff für die konstruktiven Diskussionen der wissenschaftlichen Ergebnisse und das kritische Hinterfragen von aufgestellten Thesen. Tim Becker, Lukas Hoffmann, Tobias Haeger, Florian Zimmermann, Cedric Kreusel, Manuel Theissen, Karsten Brennecke, Manuel Runkel, Kordula Kraus, Timo Maschwitz, Eva Grimberg, Dr. Sara Trost, Dr. Kirill Zilberberg, Dr. André Räupke, Tim Hasselmann, Christian Tückmantel, Bujamin Misimi und Andreas Makris danke ich für für die angenehme gemeinsame Zeit am Lehrstuhl. Darüber hinaus möchte ich mich bei allen studentischen und wissenschaftlichen Hilfskräften sowie bei Bachelor- und Masterstudenten bedanken, die mich mit ihrer Arbeit in meiner Forschung unterstützt haben bedanken. Ebenfalls bedanken möchte ich mich bei Dr. Tina Keller (*Lehrstuhl für Makromolekulare Chemie, Uni Wuppertal*), für die

gute Zusammenarbeit am EPOS Projekt und die gemeinsamen Reisen zu den Projekttreffen, Ivan Shutsko (*Lehrstuhl für großflächige Optoelektronik, Uni Wuppertal*) für die optischen Analysen der Schichten, sowie Tobias Tschorn und Dr. Georg Grötsch (*InovisCoat GmbH)* für die gemeinsame Projektarbeit an Elektrolumineszenzfolien. Ein großer Dank geht natürlich an meine Frau Theresa, sowie meiner Familie, Sabine, Reinhold, Katharine, Sandra und Joachim, für die anhaltende Unterstützung und den Rückhalt während der gesamten Zeit. Danke!

Abstract

Semitransparent electrodes are an essential part in every optoelectronic device to allow the in- or outcoupling of light. Several specialized applications of optoelectronic devices demand a semitransparent top electrode; for example in the case of thin film solar cells, to afford top-illumination or even entirely see-through devices. The main focus of this work are silver nanowires as electrode material for opto-electronic device applications. Silver nanowires show excellent electrical properties and can be deposited by various techniques, such as slot die coating or spray coating, and are therefore inherently roll-to-roll processable. Furthermore silver nanowires enact as key material for semitransparent electrodes that combine low sheet resistance and high transmittance with low temperature deposition at atmospheric pressure. Moreover silver nanowires can be dispersed in water which is environmentally friendly and requires less safety measures, i.e. explosion prevention in case of alcoholic dispersions. This work presents the use of silver nanowires, casted from aqueous dispersions on top of several optoelectronic devices. In addition to the general application of silver nanowires in alternate current electroluminescent devices, a new device architecture, enabled by the processing of silver nanowires on top of an electroluminescent device, is introduced which allows to stack two emissive layers and operate them individually. Hereby a color tunable device is achieved, which allows to vary the emitted colour based on the voltage applied to the individual sub-devices. Moreover, semitransparent thin film solar cells with silver nanowire top-electrodes are presented. The deposition of silver nanowires from aqueous dispersions on top of perovskite solar cells is hereby enabled by an atomic layer deposition grown SnO_x barrier, which was unprecedented at that time. Problems related to unfavourable electronic alignment with adjacent metal-oxide layers are unravelled and workarounds to mitigate Schottky barriers are presented. As a brief outlook for future prospects, the use of ALD-grown indium oxide is introduced as a semitransparent, conductive gas diffusion barrier.

Contents

1 Introduction **1**

2 Physical fundamentals **6**

2.1 Semitransparent Electrodes and Deposition Techniques 6

2.1.1 Figure of Merit for Semitransparent Electrodes 7

2.1.2 Indium Tin Oxide as Transparent Electrode 7

2.1.3 Silver Nanowire Electrodes 8

2.2 Deposition Techniques 9

2.2.1 Mayer Rod Coating 9

2.2.2 Ultrasonic Spray Coating 10

2.3 Alternating Current Electroluminescent Devices 13

2.3.1 Emission Principle 13

2.3.2 Determination of Emitted Colors 15

2.4 Solar Cells 17

2.4.1 Solar Cell Characteristics 18

2.4.2 External Quantum Efficiency 20

2.5 Thin Film Solar Cells 21

2.5.1 Non-Fullerene Organic Solar Cells 21

2.5.2 Perovskite Solar Cells 23

3 Experimental **25**

3.1 Fabrication of Semitransparent Electrodes 25

3.1.1 Nanowire Electrodes via Mayer Rod Coating 25

3.1.2 Ultrasonic Spray Coating 29

3.1.3 Indium Tin Oxide Electrodes 34

3.2 Alternating Electroluminescent Devices 35

3.2.1 Device Materials and Preparation 35

3.2.2 Device Characterization . . . 36
3.3 Thin Film Solar Cells . . . 36
3.3.1 Characterization of Solar Cells . . . 36
3.3.2 Non-Fullerene Organic Solar Cells . . . 37
3.3.3 Perovskite Solar Cells . . . 37

4 Electroluminescent Devices **39**
4.1 Key Requirements for Semitransparent Electrodes in Alternating Current Electroluminescent Devices . . . 40
4.2 New Electrode Materials for Alternating Current Electroluminescent Devices . . . 43
4.2.1 Inverted Layer Sequence on Aluminum Substrates . . . 43
4.2.2 Bifacial Device Architecture . . . 45
4.3 Tandem Alternating Current Electroluminescent Devices . . . 47
4.3.1 Green/Green Tandem Devices on Aluminum Substrate . . . 48
4.3.2 Green/Green, Bifacial Tandem Devices . . . 48
4.3.3 Orange/Blue, Bifacial Tandem Devices . . . 51
4.4 Conclusion . . . 56

5 Semitransparent Organic Solar Cells **57**
5.1 Evaporated Molybdenum Oxide and Liquid Processed PEDOT:PSS . . . 58
5.2 Semitransparent Solar Cells Using Molybdenum Oxide . . . 59
5.3 Fully Solution Processed Semitransparent Solar Cells . . . 61
5.4 Conclusion . . . 64

6 Semitransparent Perovskite Solar Cells **65**
6.1 Influence of Water on $FACsPbI_3$ Perovskite Layer . . . 67
6.2 Comparison of Semitransparent Silver Nanowire Electrodes and ITO . . . 68
6.3 Ag-NW Based Electrodes for $FACsPbI_3$ Solar Cells . . . 69
6.4 Conclusion . . . 80

7 ALD-Grown Indium Oxide as Semitransparent Conductive Gas Diffusion Barrier **81**

8 Conclusion **87**

A Appendix **90**

List of Figures

2.1 Schematic drawing of the Mayer Rod coating technique 9
2.2 Schematic drawing of the flat head nozzle 11
2.3 Schematic drawing of the spray head 11
2.4 Influence of the permittivity of the materials on the electric field in the EL-device. 14
2.5 Schematic device architecture of an ACEL device 15
2.6 Image of the CIE diagram with the black body curve and the reference white point and Color matching functions of the standard observer . . . 16
2.7 Equivalent circuit and J/V characteristics of a solar cell 18
2.8 Exemplary EQE Graph with integrated current density 21
2.9 Progress of fullerene-based and non-fullerene organic solar cells over the past 34 years 23
2.10 ABX_3 perovskite structure 24

3.1 Sheet resistance, transmittance and figure of merit vs. nanowire concentration for mayer rod coated nanowire electrodes 27
3.2 SEM images of mayer rod deposited electrodes from different nanowire concentrations 27
3.3 Sheet resistance, transmittance and figure of merit for mayer rod coated nanowire electrodes in the literature 29
3.4 Illustration of the Coffee stain effect 30
3.5 Schematic drawing of the prevention of the coffee stain effect 30
3.6 Illustration of the drying effects on spray coated nanowire electrodes . . 31
3.7 SEM images of nanowire electrodes deposited from 1mg/ml dispersion . 32
3.8 SEM images of nanowire electrodes deposited from 0.5 mg/ml dispersion 32
3.9 SEM images of nanowire electrodes deposited from 0.25 mg/ml dispersion 33

3.10 Sheet resistance, transmittance and figure of merit for mayer rod and spray coated nanowire electrodese 34
3.11 Transmittance and reflectance spectra of the Ag-NW and the ITO electrodes 35

4.1 Equivalent circuit diagram and simulation of the large ACEL device . . 40
4.2 Capacity measurement for single ACEL-devices 41
4.3 Luminance of ACEL-devices in relation to the distance to the busbar of the device 42
4.4 Comparison between an conventional ACEL-device and an inverted layer sequence 44
4.5 Comparison of an inverted ACEL-device with Ag-Graphite electrode and an ACEL-device on aluminum substrate. 44
4.6 Comparison of either side of the bifacial device with two Ag-NW electrodes, the cumulated luminance of the bifacial ACEL-device and the ACEL-devices with opaque aluminum or Ag-Graphite electrode 45
4.7 Transmittance,reflectance and absorbance of the dielectric and the EL-Layer 46
4.8 Photograph of the bifacial ACEL-device 46
4.9 Emission spectra of both sides of the bifacial EL-device 47
4.10 Layer sequence and Luminance vs. voltage characteristics of the tandem device on aluminum substrate 48
4.11 FIB-cut crossection of the bifacial tandem device 49
4.12 Layer sequence and Luminance vs. voltage characteristics of the bifacial tandem device with all electrodes made from Ag-NW 50
4.13 Schematic and plots for all operation modes of the bifacial tandem device, operation only one sub-device and measuring from either side 50
4.14 Bifacial tandem device with blue and orange emitting layer 52
4.15 Bifacial tandem device with blue and orange emitting layer 52
4.16 Luminance of the bifacial blue/orange tandem device measured from either side 53
4.17 CIE Diagram of the blue/orange tandem ACEL-device 54
4.18 Spectrum of the blue/orange tandem ACEL-device at certain white emitting parameters 55
4.19 Photographs of the blue/orange tandem ACEL-device at certain voltage ratios 55

5.1 Schematic drawing of the non-fullerene solar cell stack 58

5.2 J/V and EQE characteristics of opaque organic solar cells using PEDOT:PSS and $eMoO_3$ as extraction layer 59
5.3 J/V and EQE characteristics of opaque and semitransparent organic solar cells using $eMoO_3$ as extraction layer 60
5.4 J/V and EQE characteristics of semitransparent organic solar cells using PEDOT:PSS as extraction layer 61
5.5 J/V characteristics of opaque and semitransparent organic solar cells . . 62
5.6 Transmittance spectra and photograph of the semitransparent device . . 63
5.7 Comparison of semitransparent organic solar cells in the literature . . . 64

6.1 J/V and EQE characteristics of a reference perovskite solar cell with 100 nm thermal evaporated silver electrode 66
6.2 Illustration of the influence of water on the perovskite solar cell stack and XRD measurement 68
6.3 Layer sequence and characteristics of a PSC with a spray coated Ag-NW top electrode. 69
6.4 Optical simulation of the loss of current in the PCBM/AZO/SnO_x/ITO ETL and the Nanowire electrode. 70
6.5 Schematic illustration and J/V characteristics of test devices in darkness and under AM1.5 illumination of a test stack used to investigate the SnO_x/Ag-NW interface. 71
6.6 J/V characteristics of test devices with an evaporated silver electrode with and w/o PVP interlayer. 72
6.7 J/V characteristics of a representative test device ITO/SnO_x/Ag-NW test devices kept in darkness after AM1.5 illumination. 72
6.8 J/V characteristics and the resulting rectification ratios of Ag-NW test devices based on SnO_x with varied charge carrier density 73
6.9 Layer sequence and J/V characteristics of the PSC with a spray coated Ag-NW top electrode and a thin ITO interlayer. 75
6.10 Optical simulation of the loss of current in the PCBM/AZO/SnO_x/ITO ETL and the nanowire electrode for top side illumination. Published in [97]. 76
6.11 EQE data, transmittance spectra and stabilized power output of semitransparent perovskite solar cells. 76
6.12 Pictures of the wrinkling and delaminating ITO electrode 77
6.13 J/V characteristics of stored PSC of the semitransparent perovskite solar cell 78

7.1 ALD growth of Indiumoxide on ALD-SnO_x 82
7.2 Reflectance, transmittance and absorbance spectra of a 100 nm InO_x layer. 83
7.3 Change of optical transmittance of calcium pads (thickness 150 nm), encapsulated with 100 nm SnO_x and 100 nm InO_x 84
7.4 Sheet resistance, transmittance and figure of merit of electrodes, shown in this work 84
7.5 Layer sequence and J/V characteristics of $MAPbI_3$ perovskite solar cells using evaporated silver or ALD-layer as electrode 85

A.1 Emission spectra of all operation modes of the multicolor tandem ACEl device 90
A.2 CIE diagram of the tandem ACEL device measured from the blue side of the device 91
A.3 Schematic drawing of the modelation for the transfer Matrix 91
A.4 Resulting transfer matrix for the schematic in Figure A.3 92

List of Tables

3.1 Nanowire concentration and density for mayer Rod coating 26
3.2 Electrical and optical properties for mayer rod coated nanowire electrodes 28

4.1 Figure of merit for all electrodes used in Figure 4.3 42

5.1 Full device characteristics of opaque organic solar cells using PEDOT:PSS and $eMoO_3$ as extraction layer 59
5.2 Full device characteristics of opaque and semitransparent organic solar cells using $eMoO_3$ as extraction layer 60
5.3 Full device characteristics of opaque and semitransparent organic solar cells using PEDOT:PSS as hole extraction layer 61

6.1 Full device characteristics of a reference perovskite solar cell with 100 nm thermal evaporated silver electrode. 66
6.2 Cell characteristics of representative solar cells with Ag-NW top electrodes. 70
6.3 Carrier density in dependence of temperature and oxygen source for different ALD-grown SnO_x layer. 73
6.4 Full characteristics of semitransparent PSCs with ITO and Ag-NW electrodes 79

7.1 Properties of ALD-grown InO_x 83
7.2 Cell characteristics of representative solar cells with Ag-NW top electrodes processed from water on solar cell stacks 85

Abbreviation	Description
AC	Alternating current
ACEL	Alternating current electroluminescent
Ag-NW	Silver nanowire
ALD	Atomic layer deposition
AM 1.5	Air Mass 1.5
AZO	Aluminum doped zinc oxide
$CaTiO_3$	Calcium titanate
CB	Conduction band
CCT	Correlated color temperature
CIE	International Commission on Illumination
CpIn	Cyclopentadienylindium(I)
D	Drop size, Electric displacement field
DMF	N,N-dimethylformamide
eAg	Thermal evaporated silver
EEL	Electron extraction layer
EL	Electro luminescent
EQE	External quantum efficiency
$FACsPbI_3$	Formamidinium caesium lead iodide
FF	Fill factor
FIB	Focussed ion beam
FOM	Figure of merit
H_2O	Water
HEL	Hole extraction layer
In_2O_3	Indium oxide
ITIC	N-type acceptor molecule $C_{94}H_{82}N_4O_2S_4$
ITO	Indium Tin Oxide
LED	Light emitting diode
$MAPbI_3$	Methylammonium lead iodide
Mn	Manganese
MoO_3	Molybdenum oxide
NP	Nanoparticle
NMP	N-methyl-pyrrolidone
O_2	Oxygen

Abbreviation	Description
O_3	Ozone
OSC	Organic solar cell
Pb	Lead
PBDB-T	Organic semiconducting polymer $(C_{68}H_{78}O_2S_8)n$
PbI_2	Lead iodide
PCBM	Phenyl-C61-butyric acid methyl ester
PCE	Power conversion efficiency
PEDOT:PSS	poly(3,4-ethylenedioxythiophene) polystyrene sulfonate
PET	Polyethylen terephthalat
PSC	Perovskite solar cell
PVP	Polyvinylpyrrolidone
RC	Resistor capacitor
RF	Radio frequency
RMS	Root mean square
SnO_x	Tin oxide
TDMA-Sn	Tetrakis(dimethylamino)tin(IV)
TiO_2	Titanium-oxide
USC	Ultrasonic spray coating
VB	Valence band
ZnO	Zinc oxide
ZnS	Zinc sulfide
ZnS:Cu	Zinc sulfide doped with copper
$ZnS:TbF_3$	Zinc sulfide doped with terbium(III) fluoride

Symbol	Description
c	Speed of light
d	Thickness
ε	Vacuum permittivity
ε_x	Relative permittivity
ε_λ	Attenuation coefficient
e	Elementary charge
E_λ	Absorbance for certain wavelength λ
L_D	Debye length
J	Current density
J_{EQE}	External quantum efficiency current density
J_{Ph}	Photo current density
J_S	Reverse dark saturation current density
J_sc	Shortcut current density
M	Molarity
n	Carrier density, Amount of substance
n_{pn}	Ideality factor of the Schockley equation
P	Power
Φ_{TC}	Figure of merit of the semitransparent conductor
ρ	Concentration, specific resistance
Q	Volumetric flow rate
R_p	Parallel resistance
R_s	Series resistance
R_{sh}	Sheet resistance
t	Time
T	Temperature, Transmittance
U	Voltage
U_T	Thermal voltage
V	Voltage
V_{oc}	Open circuit voltage

1

Introduction

Optoelectronic devices, that detect emit or control light have become an indispensable part of our daily life. Examples include photodiodes/solar cells, to light emitting diodes (LEDs), organic LEDs (OLEDs) and alternating current electroluminescent devices (ACEL). Typical thin film opto-electronic devices consist of functional layers that are monolithically integrated whereby the generation of charge carriers or photons takes place in a so called active layer or at the interface of two layers [1, 2]. No matter in which direction the photon/electron conversion takes place in the device it is essential, that photons can reach the active layer or leave the device without being absorbed by functional layers. Therefore at least one electrode of the device must be semitransparent for photons at least in a spectral range, that is relevant for the specific application. For lighting applications the range of transmittance should cover the visible region, i.e., $420 - 750\,nm$, while for solar cells a transmittance extending into the adjacent UV and IR regions would be desired [2, 3].

To enhance the field of applications for opto-electronic devices, semi-transparency of the devices is of interest. Thereby it is possible to integrate opto-electronic devices in windows or glasses and potentially open up completely new areas of application. Examples are solar cells in glass fronts of large buildings and light emitting windows [4, 5]. By integrating solar cells in urban architecture, the tremendous potential of

photovoltaics can be used in a more efficient way. While most thin film semiconductors are semitransparent by default [6], either because of their wide band gap or just due to their overall low thickness, common electrodes made from thermally evaporated metals tend to be highly reflecting which renders the whole device opaque. Therefore, in order to achieve a fully semitransparent device, both electrodes of the device have to be semitransparent.

Until today Indium tin oxide (ITO) is the state of the art transparent conductive material for all opto-electronic devices [2, 7] that use visible light, due to its excellent transmittance in the visible spectrum exceeding 90% with a relatively low sheet resistance of $15\,\Omega/sq$ (for a 100 nm thick layer). In order to achieve these outstanding properties, ITO requires a thermal treatment at elevated temperature ($> 400°C$) [8–10]. However, the requirements for opto-electronic devices and the deposition techniques are pushed towards large area, low temperature, high throughput and low cost roll-to-roll production, which states a serious challenge for ITO [11]. An alternative to ITO, that is able to fill all the requirements for these applications, are silver nanowires. Silver nanowires are microscopic wires made from silver ranging from 10 to a few 100 nanometers in diameter and up so several microns length [12]. Nanowires are mostly dispersed in solvents like alcohols or water and therefore by default roll-to-roll printable. First reports on semitransparent electrodes that use silver nanowires date back to 2008 [13]. Based on the pioneering work of Lee et al. silver nanowire meshes have been developed into a promising material system for semitransparent electrodes. While in the beginning a simple drop casting technique was used to deposit the silver nanowire dispersions, more and more publications describing roll-to-roll processing can be found in the literature [14–18].

Especially in regards to the growing demand for regenerative energy it is necessary to realise low cost production for solar cells. Hereby silver nanowires can make a decisive contribution. The intrinsic low temperature roll-to-roll processability of silver nanowire networks on plastic foils at atmospheric pressure is a significant advantage compared to the common ITO, as discussed earlier. To realise semi transparent devices it is necessary to render both electrodes of electrodes of the device semitransparent which can be enabled by silver nanowires. To further increase the efficiency of a solar cell it is possible to construct a so called tandem-cell. In this architecture two solar cells with different active materials are stacked, and therefore the spectral bandwidth for the absorption is increased. For example perovskite silicon tandem solar cells are reported in the literature to exceed the 29% mark for power conversion efficiency [19]. In this architecture, a perovskite solar cell (PSC) with an absorption from 380 to 780 nm is

stacked onto a silicon solar cell, which is able to absorb the infrared light, transmitted by the perovskite solar cell. Hereby, the efficiency of the solar cell is increased and the incident optical power of the sunlight is used in a more efficient way. For a functional tandem stack it is necessary that both electrodes, and therefore the whole upper solar cell, are semitransparent (transparent for the spectral range to be absorbed by the lower sub-cell).

The aim of this work is to demonstrate novel architectures for opto-electronic devices based on roll-to-roll suitable, semitransparent electrodes, mostly silver nanowires networks. The main focus hereby is on the possibility to process the semitransparent electrode on top of an already existing device with a transparent bottom electrode, and therefore, by replacing the opaque top electrode with a semitransparent one, rendering the whole device semitransparent. Hereby, semitransparent devices can be realised and potential platforms for new use cases are given. In the first part of this work, alternating current electroluminescent devices are introduced. By the use of silver nanowires as electrode material it is possible to enhance the overall light output of the devices. Furthermore, a new device architecture is shown that is enabled by the usage of semitransparent electrodes. Hereby, two individual electroluminescent devices are stacked, sharing a joint middle electrode, resulting in a three terminal tandem. In the literature two approaches for white emitting devices are given. Hrabal et al. used a mix of blue and orange emitting particles [20]. By the mix ratio of particles they were able to tune the emitted color from orange to white to blue. Hereby the color was predetermined by the chosen ratio, and therefore no color tuning can be achieved. Opposed to that in the three-terminal tandem device the ratio can be tuned individually by changing the amplitude of the sub devices. Zuo et al. report a different approach. Similar to the devices in this work, they stacked two emission layer (blue and orange) on top of each other, using a PET/ITO substrate and Ag-NW as top electrode. In this approach the emitted color is tuned by the applied electric field [21]. In this work, two individual devices using orange and blue emission zones are stacked on top of each other, achieving a tunable device with orange - white - blue emission. This stacking of individual devices is enabled by the silver nanowire electrode on top of the bottom device, surpassing the flexibility in luminance and color compared to the reported approaches. In the second part of this work, semitransparent thin film solar cells with nanowire electrodes deposited from aqueous dispersions are discussed. As perovskite solar cells are extremely susceptible to degradation in the presence of water it was not possible to perform aqueous processing on top of perovskite solar cells without damaging the perovskite severely [22–24]. Since water is a favourable dispersing medium for industry production, due to the fact that no explosion prevention measures are necessary op-

posed to alcoholic dispersions, it is necessary to protect the perovskite material against the devastating influence of such an aqueous process. Although metal oxide barriers, grown by atomic layer deposition (ALD) were previously used to protect susceptible devices [25, 26], water processing on top of perovskite solar cells was never shown in the literature. This work work shows impermeable electron transport layers, based on ALD grown tin oxide, that enable the deposition of semitransparent AgNW electrodes from green aqueous dispersions on top of the perovskite cell without damage. The polyvinylpyrrolidone (PVP) capping agent of the AgNWs is found to cause a work function shift and an energy barrier between the AgNWs and the adjacent ETL. Thus, a high carrier density ($\approx 10^{18}\, cm^{-3}$) in the ETL is required to achieve well-behaved J/V characteristics free of s-shapes. Ultimately, semitransparent PSCs are demonstrated that provide an efficiency of 17.4%, which was the highest efficiency of semitransparent p-i-n perovskite solar cells with an AgNW top electrode at that time. Finally a brief outlook for future applications of ALD grown indium oxide layers on top of perovskite solar cells is given. In general this work lays ground for highly efficient, roll-to-roll processable, robust and semitransparent perovskite solar cells.

Parts of thesis parts of this thesis have been published in scientific journal articles and conferences.

Publications

1. T. Gahlmann, T. Tschorn, T. Maschwitz, L. Gomell, T. Haeger, G. Grötsch, R. Heiderhoff, and T. Riedl: Bi-facial Color-Tunable Electroluminescent Devices *ACS Appl. Mater. Interfaces, 13, 24, 28514-28520 (2021)*

2. T. Gahlmann, K. O. Brinkmann, T. Becker, C. Tückmantel, C. Kreusel, F. van gen Hassend, S. Weber, and T. Riedl: Impermeable charge transport layers enable aqueous processing on top of perovskite solar cells *Adv. Energy Mater. 10, 1903897 (2020)*

Conference contributions

1. K. O. Brinkmann, T. Gahlmann, J. He, C. Tückmantel, M. Theisen, T. Becker, J. Bahr, J. Song, J. Qu, and T. Riedl: Intrinsic ALD Barriers Enable Processing on Top of Perovskite Solar Cells from Environmentally Friendly Solvents *Proceedings of nanoGe Fall Meeting 19 (NGFM19), Berlin (Germany) (2019)*

2. T. Gahlmann, K. O. Brinkmann, C. Tückmantel, T. Becker, J. He, J. Bahr, C. Kreusel, and T. Riedl: Aqueous processing of Ag-nanowire electrodes on top of semi-transparent perovskite solar cells *SPIE Optics and Photonics, San Diego (USA), 110940D (2019)*

3. K. O. Brinkmann, J. Zhao, T. Hu, N. Pourdavoud, T. Gahlmann, R. Heiderhoff, S. Olthof, K. Meerholz, A. Polywka, B. Cheng, Y Chen, P. Görrn and T. Riedl: Self-Encapsulating Air-Resilent Semitransparent Perovskite Solar Cells with Superior Thermal Stability Beyond 2000h *MRS Spring Meeting, Phoenix (USA) ES1.2.10 (2017)*

4. K. O. Brinkmann, J. Zhao, T. Hu, T. Becker, N. Pourdavoud, S. Olthof, K. Meerholz, L. Hoffmann, T. Gahlmann, R. Heiderhoff, M. Oszajca, D. Rogalla, N. A. Lüchinger, Y. Chen, B. Cheng, T. Riedl: Pushing the lifetime of perovskite solar cell beyond 4500 h by the use of impermeable tin oxide electron extraction layers *SPIE Optics and Photonics, San Diego (USA) 10363-32 (2017)*

2

Physical fundamentals

This chapter aims to explain the basic device characteristics and the general properties as well as key indicators for the semitransparent electrodes used in this work. Furthermore the most important material properties as well as the opto-electronic functionality of the devices used in this work are explained.

2.1 Semitransparent Electrodes and Deposition Techniques

In the following, the basic parameters of semitransparent electrodes are explained. Hereby a general overview of the requirements in transparency and sheet resistance is given, as well as a figure of merit that is used in the literature to compare different semitransparent materials. In addition, the deposition techniques used in this work are elaborated.

2.1.1 Figure of Merit for Semitransparent Electrodes

The choice of semitransparent electrode materials is based on the desired parameters for the device application. Ideally, the electrode shows a minimum in sheet resistance with a maximum in transmittance. Unfortunately these parameters influence each other in a negative relationship. To reduce the sheet resistance by 50 % without changing the material the deposited layer has to be twice as thick ($R_{sh} = \rho/d$ with d being the thickness of the layer), which directly lowers the transmittance exponentially according to Lambert Beer [27] ($I = I_0 \cdot exp(-\alpha(\lambda)d)$ and therefore the absorbance as $1 - \frac{I}{I_0} = 1 - exp(-\alpha(\lambda)d)$ with $\alpha(\lambda)$ being the absorption coefficient that describes the intensity attenuation of light passing through a specific material at the wavelength λ and d being the thickness). Therefore, a trade off calculation between sheet resistance and transmittance has to be introduced. In 1976, G. Haacke reported a new figure of merit (FOM) to compare semitransparent electrodes with different material parameters [28]. Haake introduced the figure of merit:

$$\Phi_{TC} = \frac{T^{10}}{R_{sh}}. \tag{2.1}$$

2.1.2 Indium Tin Oxide as Transparent Electrode

Indium Oxide (In_2O_3) mostly shows a high conductivity due to its high amount of oxygen defects in its crystal structure, and therefore a high concentration of free electrons [29, 30]. It is possible to achieve ALD grown In_2O_3, that has also been shown to offer high charge carrier densities around $10^{20}\,cm^{-3}$ even at deposition temperatures around 80 °C [31]. Libera et al. state, that for ALD grown In_2O_3 this high carrier concentration at low growth temperatures are due to the amorphous structure of the Indium Oxide which comes with a great number of defects, i. e. oxygen vacancies that donate charge carriers [31]. To further increase the charge carrier density and the conductivity In_2O_3 layers are typically doped with tin, resulting in the well known Indium tin oxide (ITO). Hereby Sn^{4+} are built into the lattice structure replacing indium atoms [32]. Ideally, all Sn atoms are ionized and replacing each one In atom, resulting in one free electron for conduction [33]. Commonly used ITO mostly consists of $(In_2O_3)_{0.9}(SnO_2)_{0.1}$. A common deposition technique employs radio frequency (RF) magnetron sputtering followed by an annealing step at temperatures around $350 - 550\,°C$ to force tin atoms

to diffuse from grain boundaries or interstitial lattice locations into the In_2O_3 lattice locations where they function as dopants (donors) [34]. This doping and annealing can increase the carrier concentration to up to $10^{21}\,cm^{-3}$. Uekusa et al. investigated the influence of the post deposition annealing on sputtered indium tin oxide film characteristics [8] and stated that the overall properties of ITO can be changed drastically by the increase of the annealing or deposition temperature compared to a deposition at room temperature [8, 9, 34]. Kim et al. performed an in depth analysis on the influence of doping concentration and growth temperature on resistivity and carrier density of pulsed laser deposited ITO films [35]. Therefore Indium Tin Oxide (ITO) is one of the most used electrode materials for opto-electronics [36] due to its low absorption coefficient for visible wavelengths and its low electric resistivity ($\approx 10^{-4}\,\Omega cm$).

2.1.3 Silver Nanowire Electrodes

Silver nanowire (Ag-NW) networks have been reported in the literature in a variety of applications [37, 38]. They tend to outperform even indium tin oxide thin films, regarding optical, electrical, and mechanical properties as well as stability and flexibility. They appear more and more in transparent and flexible applications in all fields of optoelectronic devices. Since Ag-NWs are typically dispersed either in water or alcohols they are inherently suitable for a wide range of casting techniques. The possible deposition techniques for nanowire network fabrication include lab scale applications such as spin coating or drop casting, and large area techniques, such as spray coating [39] or doctor blade/meyer rod coating. Even roll-to-roll slot die coating is possible to deposit nanowires, which is the most desired deposition technique in regards to low cost, large area, high throughput production [15, 40]. Already in 2014 Ag-NWs were used as semitransparent top electrode for organic solar cells, paving the way for liquid processed, semitransparent, thin film solar cells [41]. The inherent flexibility of silver nanowire networks enable the usage even in flexible devices. In 2015 Guo et. al realised fully printed organic tandem solar cells and showed the enormous potential of silver nanowires for mass production of solar cells [42]. In 2019 flexible non-fullerene organic solar cells have been reported by using silver nanowire networks as bottom electrode [43]. Also for electroluminescent devices there are various reports that show the usage of silver nanowires to realise flexible devices [44–48]. Therefore silver nanowires deliver the platform for large area, roll-to-roll processable semitransparent electrodes, and by that for all kinds of large area and flexible optoelectronic device applications.

2.2 Deposition Techniques

This section introduces the deposition techniques that were used to deposit the Ag-NW electrodes. For low cost, large area and high throughput production slot die coating is a desired deposition technique. At lab scale the slot die coating process can be replaced with a so called mayer rod coating process. As an additional scalable deposition technique, ultrasonic spray coating is introduced.

2.2.1 Mayer Rod Coating

The results of lab scale deposition techniques like drop casting or spin coating are not suitable for roll-to-roll production or can not be transferred to large scale production in general. Opposed to that, the principle of mayer rod coating is close to the desired slot die coating, and even the mayer rod coating itself can be used in roll-to-roll processes without major modifications. Therefore mayer rod coating was chosen to cast nanowire networks on PET-foils for usage in large area devices. A mayer rod, also called wire wound rod, is a rod, with a metal wire wrapped around as shown in Figure 2.1. With this technique any kind of ink can be deposited on a substrate.

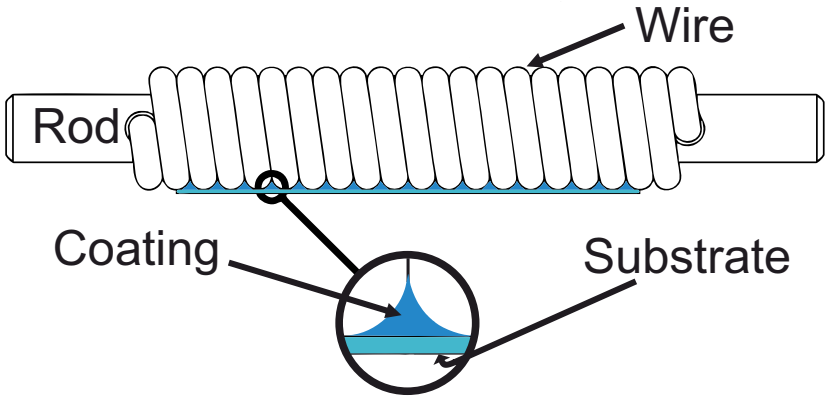

Figure 2.1: *Schematic drawing of the Mayer Rod coating technique. The area between the rounding of the wire defines the amount of liquid that is spread on the substrate while excess material is pushed by the rod.*

In the literature mayer rod coating is widely used for deposition of nanowire electrodes on flexible foil substrates for a decade [49]. Hereby the mayer rod is placed on the substrate, and an amount of ink is applied in front of the rod. Next, the rod is is pulled over the substrate thereby spreading the ink on the substrate, removing excess

ink. The diameter of the wire determines the space between the wires and thus the wet layer thickness as pictured in Figure 2.1. Trivially for nanowire electrodes the amount of nanowires remaining on the substrate defines the transmittance and sheet resistance of the resulting electrode. To vary the amount of nanowires it is possible to either tune the concentration of nanowires in the applied ink, or change the diameter of the wires and therefore the wet layer thickness. Due to the wide availability of different rod sizes, this coating method can be used for various applications.

2.2.2 Ultrasonic Spray Coating

The ultrasonic spray coating (USC) technique offers several advantages over the conventional casting techniques [50] by enabling the nebulization of liquids and dispersions of nanoparticles or nanowires; hence it is considered a "low impact" deposition technique. Characteristic for the USC is the low diameter of the atomized drops of $13\text{-}70\,\mu m$. This affords highly controllable spray patterns and reliable, consistent results.

The USC is based on the ultrasonic atomization phenomena first reported by Lord Rayleigh in his work "The Theory of Sound" in 1877 [51]. If a flat surface, that is wetted with a film of liquid, is forced into perpendicular vibration, the liquid absorbs the vibrational energy and forms a stationary wave (capillary wave). The capillary waves are forming rectangular grid patterns with alternating vertices. With a higher amplitude of vibration, the amplitudes of the capillary waves are rising accordingly, thus the vertices are getting higher and narrower. At a critical point the vertices are too high and can no longer be stabilized by capillary forces. Therefore the waves collapse and small drops are released perpendicular to the surface as shown in Figure 2.2 [52].

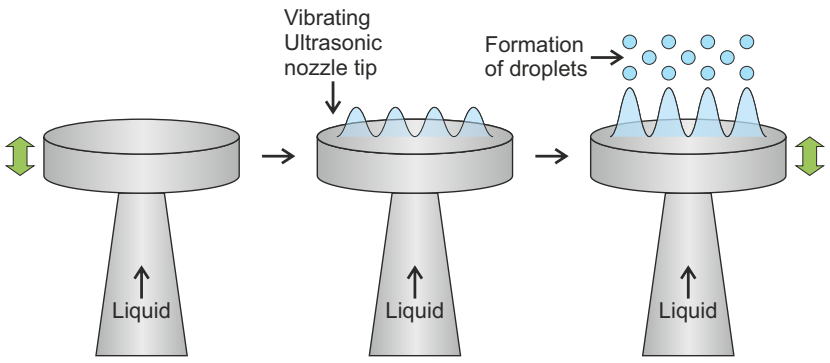

Figure 2.2: *Schematic drawing of the atomization process using a flat head nozzle as used in this work. The liquid is pushed on the flat head and forms into a film. A capillary wave forms on top of the vibrating ultrasonic nozzle tip. With higher amplitudes droplets form and atomize from the nozzle tip. Illustration inspired by [53].*

In this work the commercially available "SonoTek Exacta Coat" spray coating system utilizing an "impact EDGE Air Shaping system" and a "120 kHz flat head nozzle" is used. Main part of this system is the ultrasonic spray nozzle. Inside of the stainless steel casing, two ceramic piezoelectric transducers are located that transform electric energy into mechanical vibration energy. Two cylinders, coupled to the transducers, form a liquid feed channel from the hose system to the atomization surface. Figure 2.3 shows a schematic drawing of the ultrasonic spray head.

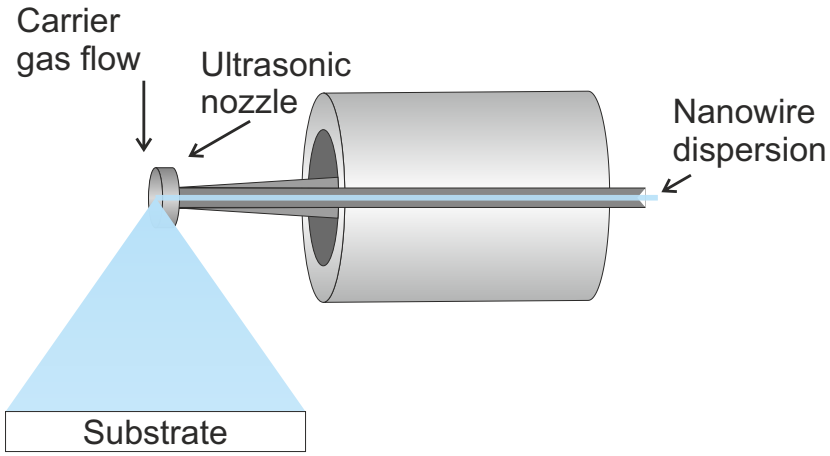

Figure 2.3: *Schematic drawing of a spray head used in this work. The carrier gas flow is located 90° to the ultrasonic nozzle. The distance to the substrate is hereby adjusted to the substrate area to ensure a homogeneous covering.*

The nozzle and the piezo electric transducers are optimized to excite a transversal static wave along the nozzle with its maximum at the atomization surface. The liquid that

is pushed through the channel absorbs the vibration energy and forms the capillary wave at the nozzle head, and thus gets atomized. The vibration energy influences the amplitude and thus the atomization of the liquid. The atomized liquid is then pushed towards the substrate by an impact air jet that is placed in an angle of 90° to the spray nozzle. The drop size is depending mainly on the frequency of the ultrasonification, the surface tension and the density of the atomized ink. The frequency is defined by the design of the spray nozzle. The drop size (D) is inversely proportional to the frequency to the power 2/3 [52–55]:

$$D \sim f^{-2/3}. \tag{2.2}$$

The literature divides the inks in "single component inks", "true solutions" and "mixtures with undissolved particles".

In this work, dispersions with silver nanowires, belonging to the third type of ink, mixtures with undissolved particles, are used. The mixtures with undissolved particles or solids such as nanowires are limited by particle size and concentration of the solids. Hereby, the particle size is critical. With a size larger than one-tenth of the medial drop size, the dispersion will not atomize properly [53]. Furthermore, the flow rate for all liquids is limited due to the atomization area of the nozzle and the oscillation frequency.

Using water, instead of ethanol, isopropyl alcohol or other alcohols eliminates the necessity of explosion prevention techniques, which is desirable for industrial manufacturing.

The optimal nozzle power for water is specified by the manufacturer with 2 W for the flat head nozzle used in this work. As reported, the concentration of the dispersed materials has a major influence on the atomization of the dispersion and thus of the homogeneity of the spray results. The amount of deposited material (n) is dependent on the concentration in the dispersion ρ [mg/ml], the flow rate Q [ml/min], and the deposition time t [s]:

$$n = \frac{\rho \cdot Q}{t}. \tag{2.3}$$

2.3 Alternating Current Electroluminescent Devices

Opposed to light emitting diodes (LEDs), which are driven by the injection of a direct current (DC), alternating current (AC) electroluminescent (EL) devices provide some notable advantages. In contrast to organic LEDs, ACEL-devices are less susceptible to degradation in the presence of oxygen and water [56]. This alleviates the need for costly high-performance gas permeation barrier technology. Furthermore, ACEL-devices can be prepared via slot-die coating, Mayer rod coating or screen printing techniques on large-area substrates (up to square meters) without the need to carefully control the particle levels in the production environment [57, 58]. ACEL-devices are even compatible with cost efficient, high throughput roll-to-roll production processes. While mechanical flexibility is still a challenge for a number of LED technologies, ACEL-devices are typically prepared on polymer substrates, such as polyethylene terephthalate (PET), which renders them inherently flexible and robust towards bending and rolling [45–48, 59]. Their flexibility and durability afford a wide area of application scenarios even under demanding outdoor conditions [60]. Even stretchable and wearable ACEL functionalities have been discussed, recently [61, 62].

2.3.1 Emission Principle

Light emission in ACEL-devices is based on the emission of doped zinc sulfide ZnS particles in an alternating electric field as reported in various publications [63–66]. In 1984 G. O. Müller discussed the various processes in an operated ACEL-device [63] and distinguished three kinds of processes. First, electrical processes were described which include the release and acceleration of electrons driven by the applied electric field. In a second process, the luminescent center is excited. Optical processes represent a third process category, the radiative and non radiative deexitations of the center of the ZnS particles. P. Benalloul found that the dominant excitation mechanism in rare-earth-doped ZnS(ZnS:TbF_3) thin films is a direct impact excitation by energetic electrons [64]. Maxia et al. evidenced that at low frequencies the brightness depends linearly on the frequency [65]. When the the frequency exceeds certain values the brightness becomes saturated at a level, which is dependent on the amplitude of the applied voltage. "The saturation of brightness occurs when, by increasing the frequency, the generation rate of the electron-hole pairs overcomes their recombination rate."[65] Allieri et al. reported spectroscopic characterization of ACEL-devices based on ZnS:Cu particles [66] and showed, that the wavelength characteristics of the emitted light in

ACEL-devices are not only dependent of the voltage, but also on the frequency. The wavelength of the emitted light is therefore dependent on the frequency of the applied voltage while the amplitude of the applied voltage only influences the emission intensity [67]. Based on this principle it is possible to design an electroluminescent device. To do so, it is necessary to apply an alternating electrical field to the doped ZnS particles. A frequently used architecture of an ACEL-device resembles that of a capacitor. In the most simple approach, a light emitting layer that is based on doped ZnS particles [67–71], and a dielectric interlayer to prevent short circuits are sandwiched between two electrodes. Due to the general characteristics of a capacitor ($E = \frac{U}{d}$) the electric field is dependent on either the applied voltage or the distance of the electrodes. In case of a capacitor with different dielectric materials, the electric field is not homogeneous between the plates, while the electric displacement field D is constant between the capacitor plates and can be described as $D = \varepsilon \cdot E$. In case of two different dielectrics the electric field is dependent on the permittivity of the materials and can be described as shown in Figure 2.4. This implies for EL-device, that a higher permittivity in the dielectric (ε_1) compared to the permittivity of the EL-particles (ε_2) results in a higher electrical field at the EL-particles (E_2) in otherwise unchanged geometries and material sequences.

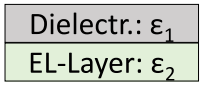

$$D = \varepsilon_1 \cdot E_1 = \varepsilon_2 \cdot E_2 \Rightarrow \frac{E_1}{E_2} = \frac{\varepsilon_2}{\varepsilon_1} \Rightarrow \varepsilon_1 \uparrow ;\ E_2 \uparrow$$

Figure 2.4: *Influence of the permittivity of the materials on the electric field in the EL-device.*

Therefore, by using high-k materials, the electric field in the ZnS particles, and therefore the light emission, can be enhanced [57]. For this work the device architecture shown in Figure 2.5 as reported by Schmidt et al. was used [72].

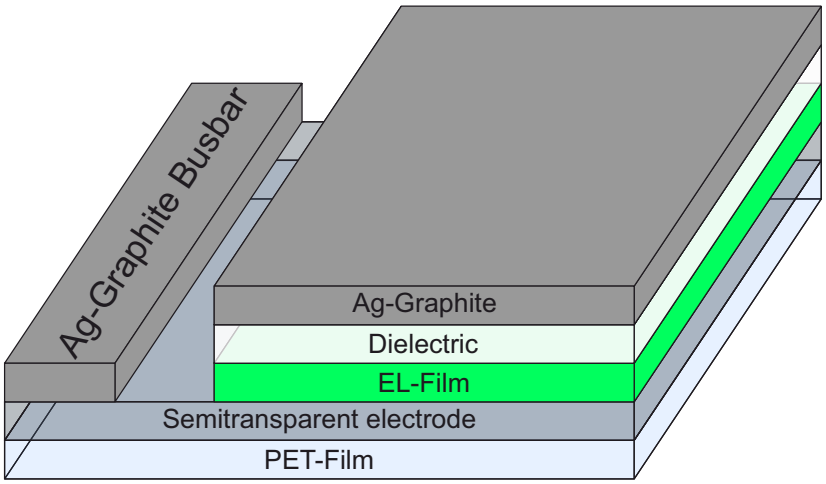

Figure 2.5: *Schematic device architecture of an ACEL device. The bottom electrode is contacted with an opaque busbar to ensure a homogeneous voltage distribution. The voltage is hereby applied between the Ag-Graphite Busbar and the Ag-Graphite top electrode. The device emits light in the direction of the PET-Film.*

In the context of this work, the layer sequence were altered, which is discussed in chapter 4.

2.3.2 Determination of Emitted Colors

For the characterization and comparison of light emitting devices the luminance $[cd/m^2]$ as well as the emitted spectrum can be measured and the spectral emission can be compared. With the spectrum it is possible to calculate the color coordinates according to the Commission Internationale de l'Éclairage (CIE / engl. International Commission on Illumination) and place them in the so called horseshoe diagram. Figure 2.6 shows a CIE diagram, with both the black body curve marked as a black line, and the reference white point $x = y = 1/3$ highlighted as a star.

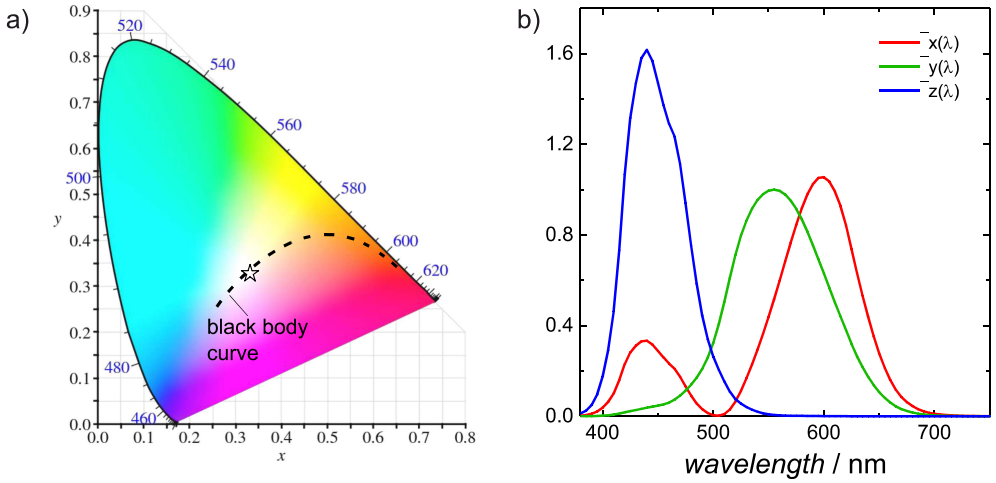

Figure 2.6: *a) CIE diagram. The black body radiation curve is illustrated as well as the reference white point x = y = 1/3 (marked with a little star). b) Color matching functions $\bar{x}(\lambda)$, $\bar{y}(\lambda)$ and $\bar{z}(\lambda)$ to model human eye. These CIE-normed sensitivity curves correspond to the sensitivity of the three color receptors of the human eye $\bar{x}(\lambda)$ (red), $\bar{y}(\lambda)$ (green) and $\bar{z}(\lambda)$ (blue).*

The parameters x and y of the chromaticity in the CIE color space can be calculated in order to determine the physiologically perceived colors in human color vision. To obtain these coordinates at first the color matching functions that correspond to the sensitivity of the three color receptors and model the chromatic response of the human eye ($\bar{x}(\lambda)$ (red), $\bar{y}(\lambda)$ (green) and $\bar{z}(\lambda)$ (blue)) are used.

With these color matching functions (Figure 2.6 b)) its possible to calculate a set of tristimulus values, X, Y and Z from a certain power spectrum $P(\lambda)$:

$$X = \int P(\lambda)\bar{x}\, d\lambda, \tag{2.4}$$

$$Y = \int P(\lambda)\bar{y}\, d\lambda, \tag{2.5}$$

$$Z = \int P(\lambda)\bar{z}\, d\lambda. \tag{2.6}$$

The values X, Y and Z are representing the actual response of different types of cone cells in the human eye to perceive the colors green, blue and red. To normalize the values, they are divided by their sum which eliminates the information about the lu-

minance [73].

$$x = \frac{X}{X+Y+Z} \tag{2.7}$$

$$y = \frac{Y}{X+Y+Z} \tag{2.8}$$

$$z = \frac{Z}{X+Y+Z} = 1 - x - y \tag{2.9}$$

Therefore only two parameters, namely **x** and **y** are necessary to describe the chromaticity (color) of the analysed spectrum and place it in the CIE color space.

For emission near the planck locus it is possible to calculate the correlated color temperature (CCT) to compare emission especially for white emission applications. According to McCamys approximation a color temperature can be derived from the CIE coordinates with a certainty of 2 degree using the following formula [74]:

$$n = \frac{x - 0.3320}{0.1858 - y} \tag{2.10}$$

$$CCT = 437 \cdot n^3 + 3601 \cdot n^2 + 6861 \cdot n + 5517 \tag{2.11}$$

Hereby, emissions of different light sources can be compared with one another and with the black body emission.

2.4 Solar Cells

The principle of energy conversion in solar cells is based on an active material, typically a semiconductor, in which electron-hole pairs are created when absorbing a photon. An important property of a semiconductor for the absorption of a photon is the forbidden gap between the valence band (VB) and the conduction band (CB), the so called band gap. If an electron is exited by absorption of a photon with an energy at least as high as the band gap energy, it is exited from the valence band to the conduction band. In the case of a solar cell the excitation occurs by the absorption of a photon. Electron hole pairs that are generated by this excitation process travel through the solar

cell stack until they either recombine or, which is the desired case, can be separated into individual charges and ultimately extracted. The number of absorbed photons is directly proportional to the generated electron hole pairs, and therefore the resulting current (apart from minor effects like recombination, two photon absorption, free carrier absorption or the auger effect). The band gap defines the spectral transmission characteristics of a solar cell.

2.4.1 Solar Cell Characteristics

In general, a solar cell is a diode, adding an additional photocurrent J_{Ph} caused by generation of free charge carriers induced by absorbed photons. In addition to the theoretical Shockley type of behaviour of the solar cell, a series (R_s) and a parallel R_p resistance cause parasitic losses. Therefore the current density (J) of a solar cell with a certain area (A) can be expressed as [75]:

$$J = \frac{1}{1 + R_s/R_p}\left(J_S\left(exp\left(\frac{V - JR_sA}{n_{pn}k_BT/e}\right) - 1\right) - \left(J_{Ph} - \frac{V}{R_pA}\right)\right). \tag{2.12}$$

In this equation J_S is expressing the reverse (bias) dark saturation current density of the solar cell, with V being the voltage. The ideality factor (n_{pn}) describes the deviation of the measured diode characteristic from an ideal one. Figure 2.7 shows a simplified equivalent circuit of a solar cell and the influence of parallel (R_p) and series (R_s) resistances on the J/V characteristics of a thin film solar cell under illumination.

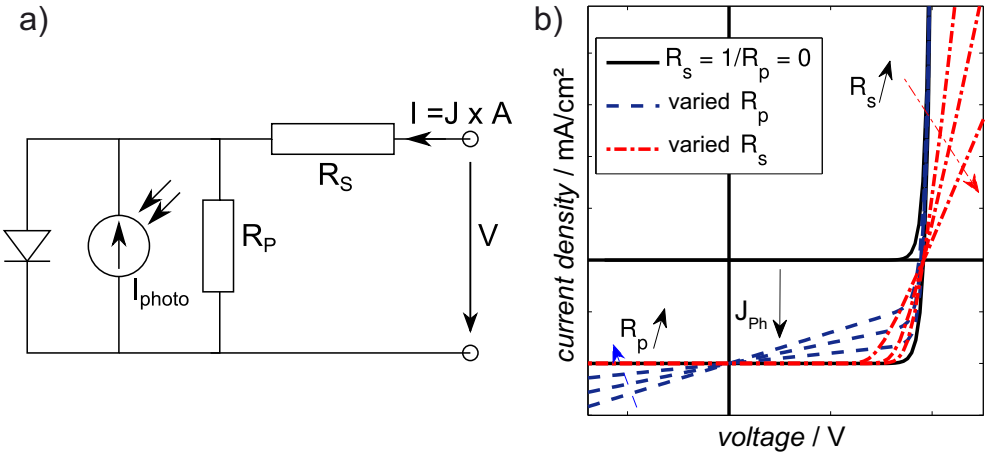

Figure 2.7: *a) Equivalent circuit and b) The influence of the parallel (R_p) and series resistance (R_s) on the J/V characteristics of a solar cell under illumination, adapted from [76].*

The main difference between the characteristic solar cell curve and the one of a p-n-junction is the additional photo current density J_{Ph} due to the charge carrier generation under illumination. This current offset in the Shockley equation, expressed by the term $\left(J_{Ph} - \frac{V}{R_p A}\right)$, is also pictured in Figure 2.7. This simplified Shockley curve presents an ideal case without parasitic recombination. The maximum power (P) generated by a solar cell is the product of current (density) J and voltage V with a maximum area that is also shown in the figure in the third quadrant. Two of the three characteristics measured in a solar cell are short current density (J_{SC}) and open circuit voltage V_{OC}. While the short circuit current density represents the current density through the solar cell with a voltage equal zero across the solar cell ($V = 0$ when short circuited) the open circuit voltage represents the maximal potential difference when operated as an open circuit ($J = 0$). Furthermore as pictured in Figure 2.7, the maximum power output is of essence. Hereby, the fill factor (FF) is used to describe the ratio between the product of voltage and current density in the actual maximum power point (MPP) and the product of J_{SC} and V_{OC} [77]:

$$FF = \frac{J_{MPP} \cdot V_{MPP}}{V_{OC} \cdot J_{SC}}. \tag{2.13}$$

This fill factor takes into account all negative effects caused by device resistances (i.e. R_s and R_p as shown in Figure 2.7) and other parasitic losses in the device [41]. Ultimately the power conversion efficiency (PCE) of a solar cell can be determined. The PCE defined as the ratio of the extracted power (P_{out}) at the MPP of the device and the power (P_{in}) of the illumination:

$$PCE = \frac{P_{out}}{P_{in}} = \frac{J_{MPP} \cdot V_{MPP}}{P_{in}} = \frac{FF \cdot J_{SC} \cdot V_{V_{OC}}}{P_{in}}. \tag{2.14}$$

The solar cell characterization in this work was performed also with a Keithley 2400 SMU using AM1.5 simulated sunlight from a solar simulator (300 W Newport, model 91160, AM1.5G, $100\,mW/cm^2$) calibrated with a certified IEC 60904-9 compliant Si reference cell (Rera Systems). J/V characteristics were obtained using a voltage sweep with a scanning speed of 500 mV/s.

2.4.2 External Quantum Efficiency

In the measurement of the solar cell with a simulated AM 1.5 G spectrum from the solar simulator the short circuit current density is subject to uncertainty as the solar simulator uses Xenon and Metal-halide lamps, that infer a slight spectral mismatch compared to the actual AM 1.5 G solar spectrum and show characteristic peaks at certain wavelengths. This can cause an over- or underestimation of the current density of the solar cell. Therefore a spectrally resolved technique has to be applied to identify and correct spectral mismatch factors; the so called external quantum efficiency (EQE) has to be measured. Specifically a tunable light source consisting of a lamp and a monochromator is used to determine the short circuit current density at each wavelength for a well known power of incident light. The emitted light of the monochromator is chopped, to enable the use of a lock-in-amplifier to detect the low signal. At first the power output from the monochromator that illuminates the solar cell is measured for each wavelength, using a power meter, to calculate the wavelength dependent amount of incident photons. Next, the solar cell is illuminated, using the same chopped light, whose power output was determined before. Thereby it is possible to calculate the ratio between the amount of photons reaching the solar cell at each wavelength and the current output(number of extracted charges) of the solar cell. This ratio is used to calculate the external quantum efficiency (EQE). The EQE is now convoluted with the AM 1.5 G reference spectrum to compute the short circuit current density that would be expected if the solar cell would be illuminated with the AM 1.5 G solar spectrum:

$$\int EQE(\lambda) \cdot AM1.5G(\lambda) \cdot \frac{e}{h \cdot c} \cdot \lambda \, d\lambda \tag{2.15}$$

Figure 2.8 displays an exemplary EQE spectrum with the integrated photo current density.

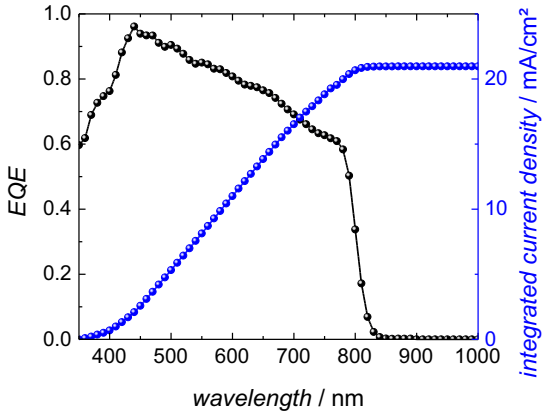

Figure 2.8: *Exemplary EQE Graph (black curve) with integrated current density (blue curve).*

2.5 Thin Film Solar Cells

All solar cells used in this work can be categorized as thin film solar cells. They are structured as follows: An ITO layer on a glass substrate is used as a transparent bottom electrode. On top of the ITO electrode, a charge extraction layer is deposited, followed by the active material, either an organic bulk-heterojunction or a perovskite layer, which will be elaborated later. The stack sequence is continued by another charge extraction layer, for the opposing charge carriers as the bottom extraction layer. At last a top electrode is deposited. Typical reference solar cells use 100 nm of thermally evaporated silver electrodes which renders them inherently opaque.

2.5.1 Non-Fullerene Organic Solar Cells

Organic solar cells have been a promising technology in the past years. In contrast to conventional solar cells, it is possible to cast them from liquid phase which makes them inherently suitable for high-throughput and low-cost roll-to-roll film manufacturing techniques [78]. The active layer in an organic solar cell is based on a so called bulk hetero junction consisting of donor and acceptor molecules. The charge separation takes place at the junction between the donor and the acceptor phase of the bulk hetero junction. Classical organic solar cells use Phenyl-C61-butyric acid methyl ester (PCBM) as the acceptor molecule [79]. With the introduction of the non-fullerene acceptor molecule *3,9-bis(2-methylene-(3-(1,1-dicyanomethylene)-indanone))-5,5,11,11-tetrakis(4-hexylphenyl)-dithieno[2,3-d:2',3'-d']-s-indaceno[1,2-i:5,6-b']dithiophene*

(ITIC), [80] in a bulk hetero junction with the donor polymer *Poly[(2,6-(4,8-bis(5-(2-ethylhexyl)-2-yl)-benzo[1,2-b:4,5-b']dithiophene))-alt-(5,5-(1',3'-di-2-thienyl-5',7'-bis(2-ethylhexyl)benzo[1',2'-c:4',5'-c']dithiophene-4,8-dione)]* (PBDB-T or PCE12) the efficiency of organic solar cells got boosted into new levels reaching new heights, due to the complementary absorption spectra of the two materials. Furthermore the offset between the Highest occupied molecular orbitals (HOMO) or Lowest unoccupied molecular orbitals(LUMO) of donor and acceptor can be tuned to below 0.2 eV which reduce voltage loss, and increases efficiency [81]. This material system got new attention as material system for semitransparent solar cells. Based on that groundbreaking work, the slightly modified polymer donor *Poly[(2,6-(4,8-bis(5-(2-ethylhexylthio)-4-fluorothiophen-2-yl)-benzo[1,2-b:4,5-b']dithiophene))-alt-(5,5-(1',3'-di-2-thienyl-5',7'-bis(2-ethylhexyl)benzo [1',2'-c:4',5'-c']dithiophene-4,8-dione)]* (PBDB-T-SF) and a new small molecule acceptor *3,9-bis(2-methylene-((3-(1,1-dicyanomethylene)-6,7-difluoro)-indanone))-5,5,11,11-tetrakis(4-hexylphenyl)-dithieno[2,3-d:2',3'-d']-s-indaceno[1,2-b:5,6-b']dithiophene* (IT-4F) were synthesized reaching a high efficiency of 13.1 % [82], only one year later. In the following years the achieved efficiencies were constantly rising. In 2019 Fan et al. exceeded 15 % (15.7 %) with the PBDB-T modification *Poly[(2,6-(4,8-bis(5-(2-ethylhexyl-3-fluoro)thiophen-2-yl)-benzo[1,2-b:4,5-b']dithiophene))-alt-(5,5-(1',3'-di-2-thienyl-5',7'-bis(2-ethylhexyl)benzo[1',2'-c:4',5'-c']dithiophene-4,8-dione)] (PBDB-T-2F)* [83] and the highly conjugated molecule *2,2'-((2Z,2'Z)-((12,13-bis(2-ethylhexyl)-3,9-diundecyl-12,13-dihydro-[1,2,5]thiadiazolo[3,4-e]thieno[2",3":4',5']thieno[2',3':4,5]pyrrolo [3,2-g]thieno[2',3':4,5]thieno[3,2-b]indole-2,10-diyl)bis(methanylylidene))bis(5,6-difluoro-3-oxo-2,3-dihydro-1H-indene-2,1-diylidene))dimalononitrile* (BTP-4F or Y6). In 2020 Liu et al. first surpassed the 18 % efficiency using a new polymer *Poly[(2,6-(4,8-bis(5-(2-ethylhexyl-3-fluoro)thiophen-2-yl)-benzo[1,2-b:4,5-b']dithiophene))-alt-5,5'-(5,8-bis(4-(2-butyloctyl)thiophen-2-yl)dithieno[3',2':3,4;2",3":5,6]benzo[1,2-c][1,2,5]thiadiazole)] (D18 or PCE18)* and Y6 [84]. Perdigón-Toro et al. state, that the electrostatic interfacial field for Y6 is large enough to compensate the Coulomb dissociation barrier for charge carrier state dissociation [85]. This remarkable progress brought back the attention to organic photovoltaics and shows the immense potential of this material class [86]. Figure 2.9 shows the progress in organic solar cells over the last years.

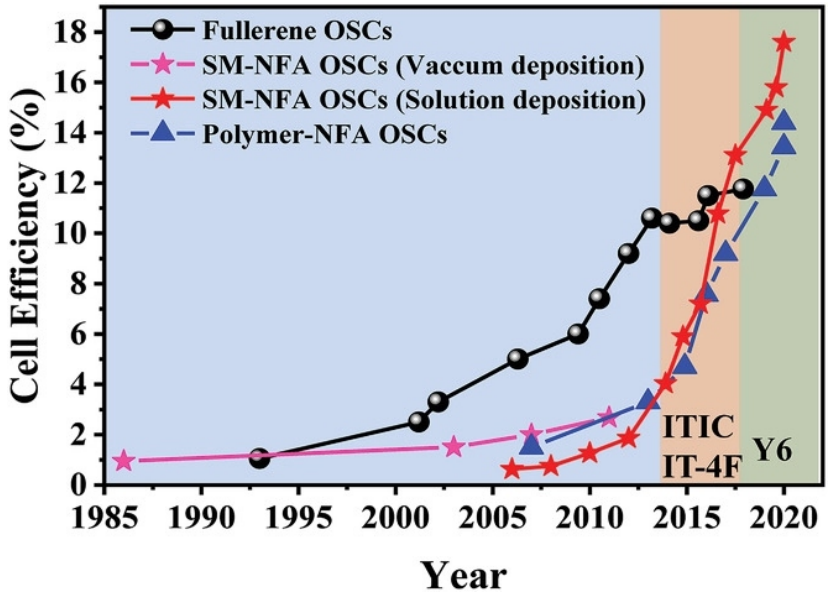

Figure 2.9: *Progress of fullerene-based and non-fullerene organic solar cells over the past 34 years [81].*

In context of this thesis PBDB-T:ITIC was used as active material, which provided the highest efficiencies at the time this work has been conducted.

2.5.2 Perovskite Solar Cells

Metal-halide perovskites are used in the literature for optoelectronic applications especially as thin film solar cells since 2009 [87, 88]. The efficiency limit predicted for perovskite solar cells based on methylammonium lead iodide ($MAPbI_3$) is around 31 % [89]. This figure is based on the Shockley-Queisser limit, as the upper limit for efficiency of unfocused sunlight. Until now the efficiencies of perovskite solar cells rose continuously. In 2021 single-junction perovskite solar cells with a PCE of 25.6% were reported [90]. Beyond their high PCEs, Perovskite solar cells combine the high PCE of silicon based solar cells and allow their production at low fabrication temperatures and material costs as well as the possible deposition on flexible roll-to-roll compatible substrates.

Perovskite structures used in optoelectronic applications are typically formed in an ABX_3-composition, with B representing a metal cation, mostly lead (Pb) and X being the respective anion, with B at the center of the octahedron and X in the corners,

typically formed by halides like chlorine, bromine or iodine. This BX_6 octahedron is part of an extended three-dimensional lattice where all corners are connected. The cubo-octahedral site of the BX_6 is hereby occupied by the larger A cation, as shown in Figure 2.10

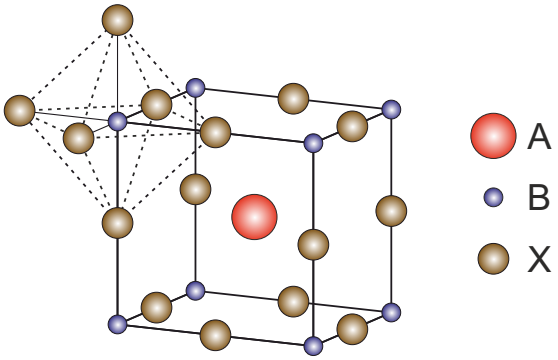

Figure 2.10: *ABX_3 perovskite structure: The larger A cation is based in the cubo-octohedral site of the octohedral BX_6 structure. Based on [91].*

In perovskite photovoltaics $CH_3NH_3PbI_3$ ($MAPbI_3$) is frequently replaced by $FACsPbI_3$ which offers higher PCEs and larger thermal stability [92]. In these kinds of solar cells the methyl ammonium ion ($CH_3NH_3^+$) or the formamidinium ion ($CH_5N_2^+$) represents the organic part of the solar cell. In contrast to organic semiconductors which have no continuous band structure and offer charge transport via hopping, perovskites offer a crystal structure and therefore enable band transport.

3

Experimental

This chapter introduces the deposition techniques used to fabricate the devices and electrodes. Furthermore the experimental details for the characterization are elaborated.

3.1 Fabrication of Semitransparent Electrodes

This section elaborates the fabrication parameters and the resulting properties of the semitransparent electrodes. The resulting electrodes are examined in regards to sheet resistance, transmittance and homogeneity.

3.1.1 Nanowire Electrodes via Mayer Rod Coating

The nanowire dispersions, provided by BASF, come with an initial concentration of 10 mg/ml and a nanowire diameter of $115 - 130\,nm$. Opposed to previous reports in the literature [49], where the nanowires are dispersed in alcohols, the formulation used in this work is dispersed in water, modified by "InovisCoat GmbH" for deposition on PET foil as described for other functional layers in [72]. To investigate the resulting

Ag-NW electrode in dependence on the concentration of the nanowires, multiple electrodes were deposited on PET with different concentrations by diluting the nanowire dispersion from $2\,mg/ml$ to $5\,mg/ml$ keeping the wet layer thickness at $50\,\mu m$ (which was previously evaluated as optimal wet layer thickness for IPA based dispersions and where therefore chosen as base for the follow up studies for water based dispersions) [49]. A wet layer thickness of $50\,\mu m$ equals $5 \cdot 10^{-3} ml/cm^2$ of liquid. Therefore, the nanowire density on the substrate is controlled by the concentration in the dispersion as shown in Table 3.1. Post deposition annealing below the glass transition temperature of PET (75 °C) has shown no influence on the sheet resistance.

Table 3.1: *Comparison between the concentration of the nanowire dispersion and the nanowire density remaining on the substrate using a* $50\,\mu m$ *mayer rod*

Concentration $[mg/ml]$	2	3	4	5
Nanowire mass/area covering $[\mu g/cm^2]$	10	15	20	25

Figure 3.2 shows the SEM images of the mentioned electrodes on PET foil. As marked in the images for low concentrations of 2 mg/ml, certain areas remain with a lower (up to no) covering of Ag-NWs (as marked in Figure 3.2 for 2 mg/ml). For high concentrations above 4.0 mg/ml agglomerates of nanowires occur (as marked in Figure 3.2 for 4 and 5 mg/ml). These agglomerates lower the overall transmittance of the electrode without lowering sheet resistance significantly as shown in Figure 3.1, which was also observed in the literature [93]. The sheet resistances for all electrodes were measured in the van-der-Pauw geometry in a homebuilt setup using a Keithley 2400 source measure unit (SMU) as current source and a Keithley 182 voltmeter.

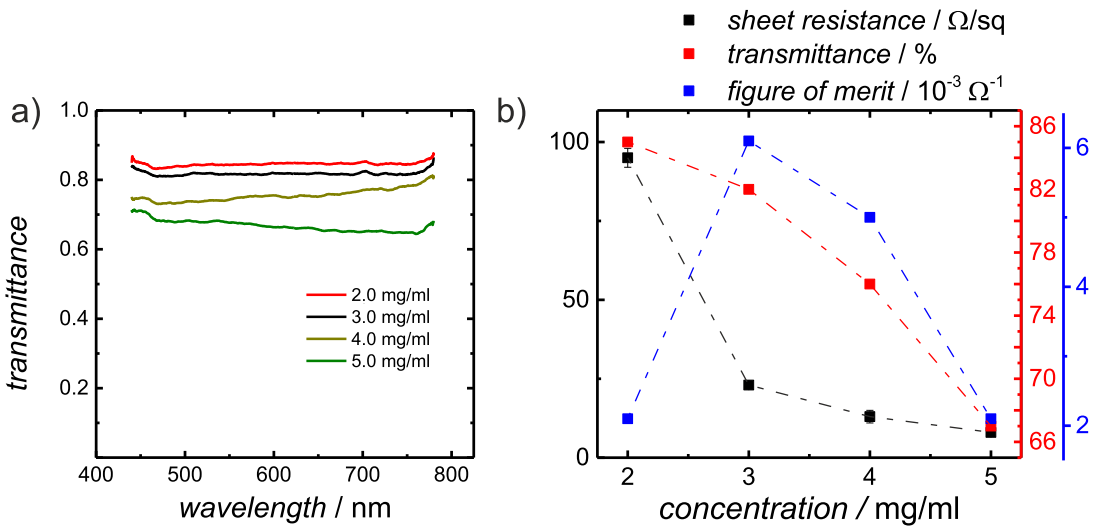

Figure 3.1: *a) Transmittance spectra and b) Sheet resistance, transmittance and figure of merit vs. nanowire concentration for mayer rod coated nanowire electrodes. It can be clearly shown, that the sheet resistance is not changing significantly using nanowire concentrations exceeding 3 mg/ml, as the figure of merit is maximised at 3 mg/ml. The lines are meant as a guide to the eye.*

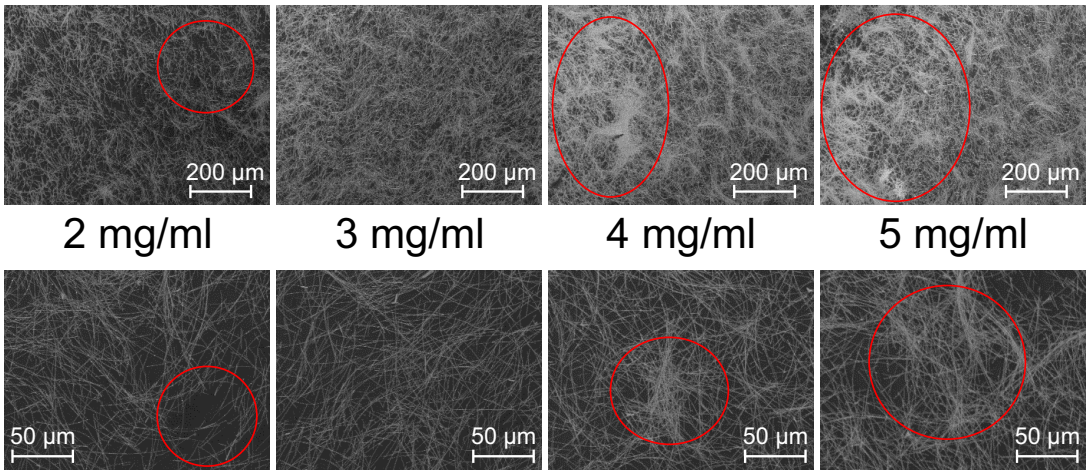

Figure 3.2: *SEM images of mayer rod deposited electrodes deposited from different nanowire concentrations. Electric and optical properties are shown in Table 3.2. Large gaps and agglomerates in the nanowire electrodes are marked with red circles.*

As already mentioned in section 2.1.1 the figure of merit is depending on sheet resistance and transmittance. As the images suggest, films casted from dispersions with a concentration of 3 mg/ml lead to the most homogeneous layers, and thus to a perfect trade off as confirmed by the figure of merit. As shown in Table 3.2 and Figure 3.1, the figure of merit is at its maximum at 3 mg/ml.

Table 3.2: *Electrical and optical properties for mayer rod coated nanowire electrodes. Obviously sheet resistance and transmittance are inversly proportional. Nevertheless the figure of merit shows a maximum at a concentration of* $3\,mg/ml$.

Concentration [mg/ml]	**Sheet resistance** [Ω/sq]	**Average transmittance** [%]	**Figure of merit** [Ω^{-1}]
2	95 ± 3	85	$2.1 \cdot 10^{-3}$
3	23 ± 1	82	$6.1 \cdot 10^{-3}$
4	13 ± 2	76	$5.0 \cdot 10^{-3}$
5	9 ± 0.5	67	$2.1 \cdot 10^{-3}$

In contrast to the literature, the electrodes in this work are not casted from nanowires dispersed in IPA but based on aqueous dispersions. In 2011 Liu et al. first reported mayer rod coated nanowire electrodes on flexible foil substrates, with a sheet resistance of $175\,\Omega/sq$ and a transmittance of 75 % [49]. Later in 2013 Kumar et al. showed electrodes with a higher transmittance of 90 % but also with a higher sheet resistance of $300\,\Omega/sq$ [94] which results in a slightly higher figure of merit. Compared to these results the electrodes in this work surpass the previously reported ones as can be derived from Figure 3.3. To further increase the figure of merit, in 2018 Kim et al. reported a "redox-welding and embedding method" pushing the sheet resistance from $43\,\Omega/sq$ to $11\,\Omega/sq$ with a high transmittance of 90 % [95] and Zhang et al. in 2019 developed a dynamic heating technique welding the nanowire interfaces, and thereby reducing the sheet resistance from around $40\,\Omega/sq$ to $24\,\Omega/sq$ with a transmittance of 91 % [93], by lowering the contact resistance at the nanowire interfaces. The electrodes presented in this work offer a high figure of merit without laborious post treatment, comparable to the literature. Opposed to the literature the nanowire electrodes in this work are casted from aqueous dispersion which is highly desired as discussed earlier. The post treatment options in the literature show the enormous potential for further increase in figure of merit to even surpass the reported records in the future.

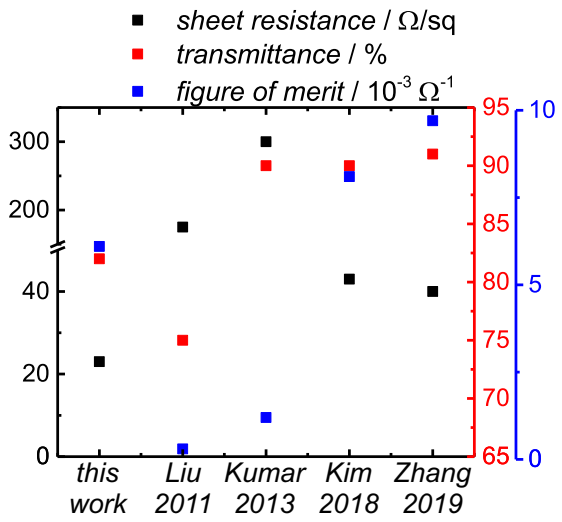

Figure 3.3: *Sheet resistance, transmittance and figure of merit for mayer rod coated nanowire electrodes in the literature, without post treatment, compared to the best electrodes in this work (see Table 3.2).*

3.1.2 Ultrasonic Spray Coating

To achieve an overall low deposition time, either the concentration or the flow rate can be raised. Both parameters have severe influence on the homogeneity of the resulting electrode. Opposed to the mayer rod coating technique, the diameter of the nanowires are of relevance. Due to the fact, that the nanowires with a diameter of $115-130\,nm$ are clogging the nozzle, nanowires with a diameter of $20-30\,nm$ were used, also provided by BASF, dispersed in water with an initial concentration of $10\,mg/ml$.

High Flow Rate

When depositing a liquid on a substrate using a spray coater, a liquid film forms on the substrate and typical drying effects during the drying time occur, the so called "coffee stain effect" [96].

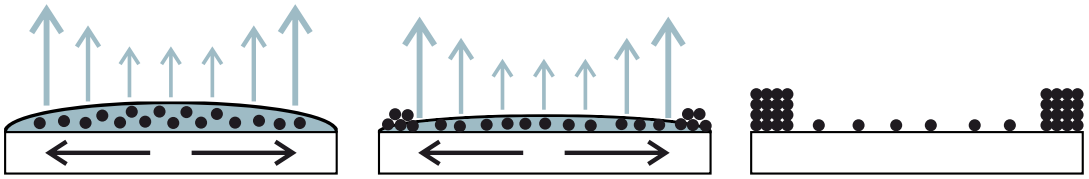

Figure 3.4: *Schematic drawing of the coffee stain effect occurring during the drying time of a dispersion. The liquid at the outsides of the substrate vaporizes faster, causing the material in the dispersion to diffuse to the edges.*

As shown in Figure 3.4 the capillary flow causes the formation of a ring around the edge of the substrate. As Deegan et al. report (1997) [96], this coffee ring effect can be prevented by modifying the viscosity of the liquid. A high viscosity prevents the particles from being pushed to the edges of the substrate. Therefore, a more homogeneous layer can be deposited, as shown in Figure 3.5.

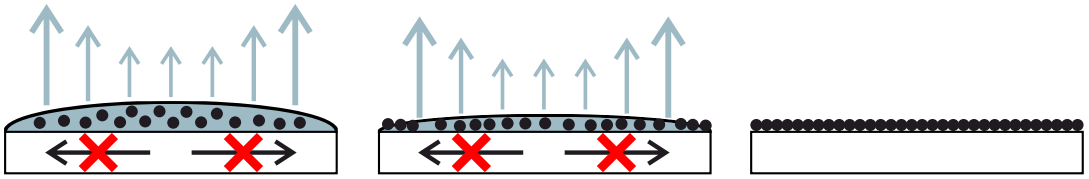

Figure 3.5: *Schematic drawing of the prevention of the coffee stain effect during the dry time of a dispersion. While the liquid at the edges is still drying faster, the high viscosity prevents the material in the dispersion from diffusing to the edges.*

When depositing silver nanowires, this coffee stain effect has a strong influence on the resulting layers. By using a heated hotplate, the dry time can be lowered but the capillary flow still causes the well known ring at the edges of the substrate (Figure 3.6 a). Using additives to enhance the viscosity of the liquid prevents this coffee ring effect (compare Figure 3.6 b). An SEM picture of the resulting electrode is also shown in Figure 3.6c. The thickening agents added to the ink to control the viscosity are propriety to InovisCoat.

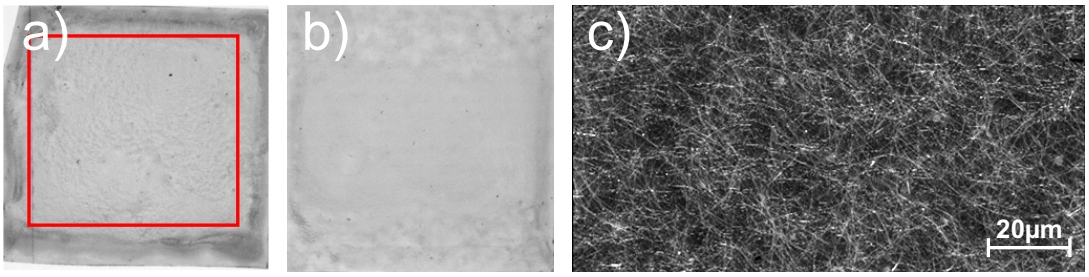

Figure 3.6: *Pictures of the dried nanowire electrodes. a) Coffee stain effect, clearly visible. Outside of the red rectangle the visible dark areas show the agglomerates of silver nanowires. b) Nanowire electrode casted from high viscosity dispersion. No dark ring of agglomerates visible. c) SEM image of the nanowire electrode shown in b)*

While the enhancement of the viscosity benefits the overall homogeneity, it is not desired for the spray coating process. Thickener agents remain on the substrate and enhance the sheet resistance of the nanowire junctions.
Therefore, the amount of liquid deposited on the substrate is lowered to a point where the dispersion drops hitting the substrate evaporate before the nanowires are able to diffuse to the edges of the substrate. Hereby no change in viscosity, and therefore no additives are necessary.

Low Flow Rates

To enhance the amount of nanowires at low flow rates, the concentration or the deposition time has to be increased. To prevent the nanowires from diffusing in a liquid film on the substrate, the flow rate was set to 0.25 ml/min and the substrate was heated to $60° C$ using a hotplate. Hereby no liquid film is forming on the substrate, but the drops hitting the substrate vaporize right after the impact. Due to the statistic nature of the spray coating process, the whole area of the substrate is covered with drops over time and a homogeneous deposition is achieved.

Dispersions with different concentrations of silver nanowires were deposited on top of heated glass substrates. The spray time as well as the concentration were taken into account to compare electrodes using the same amount of nanowires forming the conductive network.

At first, the concentration was set to $1\,mg/ml$ respectively $0.5\,mg/ml$ and electrodes were deposited. By varying the time, the same amount of nanowires of approximately

$25\,\mu g/cm^2$ were deposited to ensure a comparison of the homogeneity of the resulting electrodes.

As shown in Figure 3.7 electrodes deposited from $1\,mg/ml$ dispersions using a mass flow of $0.25\,ml/min$ for $1\,min$ show visible areas, coated with and areas without nanowires.

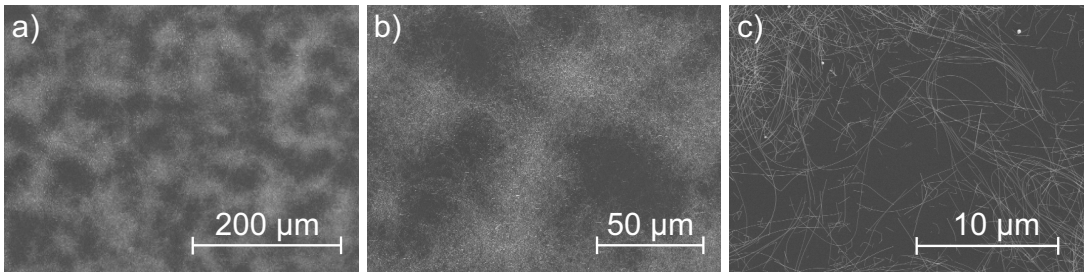

Figure 3.7: *SEM images of the dried nanowire electrodes from 1 mg/ml dispersion. a) Clearly visible areas of clumping and uncoated areas. Inhomogeneous covering (125x magnification). b) 500x magnification to show the macroscopic not covered areas. c) 2000 x magnification. Few nanowires in the uncoated areas, no full covering for homogeneous network.*

Figure 3.8 shows the resulting electrodes for $0.5\,mg/ml$ for a doubled deposition time. As visible in Figure 3.8 a) there are still areas with a high amount of nanowires and darker areas with a low amount of nanowires, caused by the material contrast of the silver nanowires to the glass substrate. Figure 3.8 c) shows that even at the dark areas a certain amount of nanowires is deposited and that the typical diameter of not covered gaps is reduced to around $1\,\mu m$.

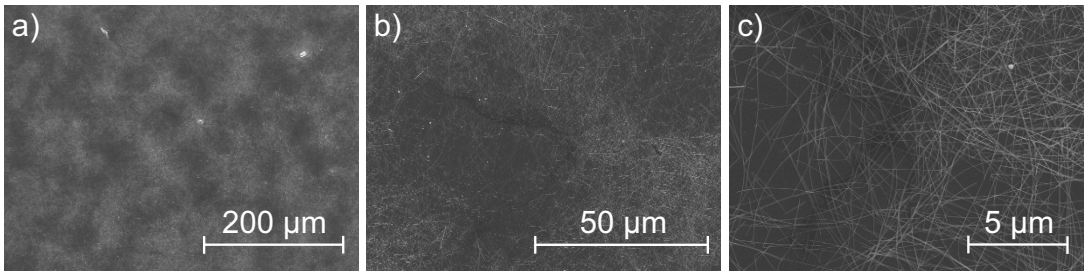

Figure 3.8: *SEM images of the dried nanowire electrode from 0.5 mg/ml dispersions. a) Clearly visible areas of clumping and uncoated areas, inhomogeneous covering (125x magnification). b) 500x magnification to show the macroscopic picture of not covered areas. c) 4000 x magnification. Few nanowires in the uncoated areas, still incomplete covering for homogeneous network.*

With further doubling in deposition time while halving the concentration of the dispersion the homogeneity of the electrode is increased to a point, where the not covered areas shrink further down as shown in Figure 3.9.

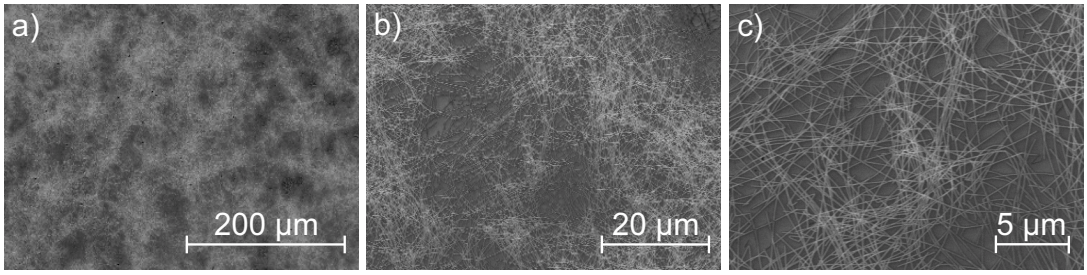

Figure 3.9: *SEM images of the dried nanowire electrodesfrom 0.25 mg/ml dispersion. a) Less clumping, and more homogeneous covering (125x magnification). b) 500x magnification of the apparently not covered areas. c) 4000 x magnification. Few nanowires in the uncoated areas, homogeneous network, gaps* $< 1\mu m$

All resulting electrodes offer a sheet resistance of around $12\,\Omega/sq$ with a transmittance of 87 % which is comparable to values reported in the literature [39]. This equals to a figure of merit of $2 \cdot 10^{-2}\Omega^{-1}$. When dispersions with a concentration of $0.25\,mg/ml$ are applied at a rate of 0.25 ml/min, a mass flow of $62.5\,\mu g/min$ of nanowires is deposited on the substrate. This equals a coverage of $6.65\,\mu g/min \cdot cm^2$. For the used 4 minutes of deposition time a total of $26.6\,\mu g/cm^2$ (which is equivalent to more than 1.5 million nanowires per mm^2) was applied to the substrate

Due to the same amount of nanowires, forming a percolated network for all deposition parameters, the sheet resistance and transmittance and thereby the Figure of merit is equal in all variants. However it was reported [41] that for applications like solar cells a homogeneous covering is necessary. Therefore, a longer deposition time with a low mass flow is necessary to ensure electrodes with not covered areas of a neglectable size are produced. It has to be noted that the transmittance of the silver nanowire electrode is solely resulting from the not covered areas since the single nanowires themselves are opaque.

Comparing the results of the two shown deposition techniques its clear, that the electrode casted by spray coating surpasses the ones, deposited by mayer rod coating. As pictured in Figure 3.10. This can most likely be attributed to the fact, that for the spray coated electrodes with low flow rates, no thickening agent was used.

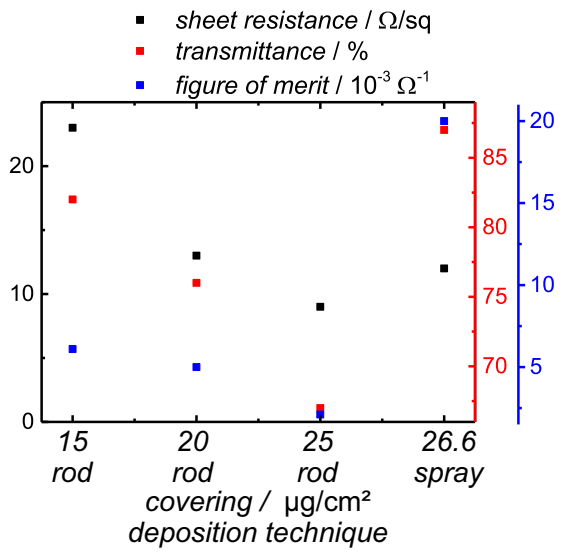

Figure 3.10: *Sheet resistance, transmittance and figure of merit for mayer rod and spray coated nanowire electrodes in this work. Note, that the rod coated electrodes are made from* $115 - 130\,nm$ *and the spray coated electrodes from* $20 - 30\,nm$ *diameter nanowires*

The different transmittance at similar covering ratios, can be explained due to the different geometry of the used nanowires. Bergin et al. state, that for highly connected nanowire networks, the ones with larger nanowire diameters will outperform those with smaller diameters, due to their larger conductance to extinction ratios [12]. Opposing to that assumption the $20\,\mu g/cm^2$ mayer rod coated electrode shows a similar sheet resistance at an even lower transmittance than the spray coated electrode. It has to be noted, that the dispersion used for the mayer rod coating, contains thickening agents to prevent drying effects such as the coffee ring effect, as discussed earlier. Nevertheless both deposition techniques bring their benefits for different applications. Furthermore results shown in this work are comparable, or even surpassing reported properties for silver nanowire electrodes [39, 49, 93–95] and are therefore appropriate for further studies in optoelectronic devices as strived for in this work.

3.1.3 Indium Tin Oxide Electrodes

ITO layers were sputtered in a previously established RF-sputtering process at room temperature using an ITO target (In_2O_3/SnO_2 90/10 wt%). The chamber pressure during sputter process was at $3{\cdot}10^{-4} mbar$ using 12.5 sccm Argon. The working distance was 6.5 cm, with a sputter power of $26\,W$ and a power density of $0.57\,W cm^{-2}$ resulting in a deposition rate of $1.3\,\text{Å}s^{-1}$. No post annealing was performed.

Figure 3.11 shows the transmittance and reflectance spectra of an unannealed ITO electrode and a spray coated Ag-NW electrode both with a sheet resistance of $\approx 12\,\Omega\,sq^{-1}$. The thickness of the ITO layer to achieve this sheet resistance was $\approx 400\,nm$.

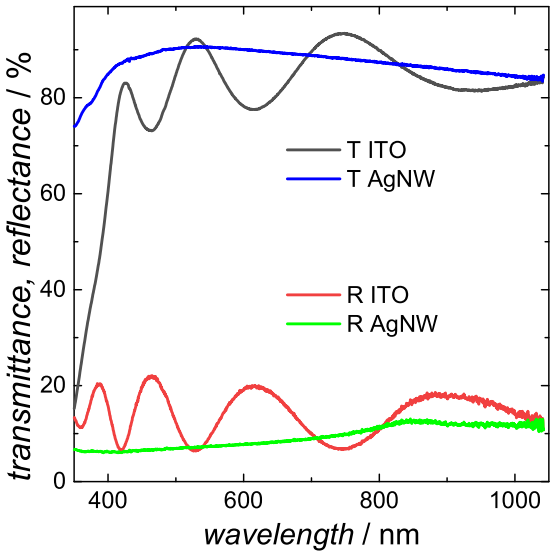

Figure 3.11: *Transmittance and reflectance spectra of the Ag-NW and the ITO electrodes with a sheet resistance of* $\approx 12\,\Omega\,sq^{-1}$. *Published in [97].*

It can be concluded, that silver nanowire electrodes surpass unannealed ITO electrodes in terms of transmittance, while offering the same sheet resistance. These results are promising for the use in optoelectronic devices.

3.2 Alternating Electroluminescent Devices

The preparation and characterization of the electroluminescent devices are introduced in the next two sections

3.2.1 Device Materials and Preparation

The device architecture used in this work is based on the materials reported by Schmidt et al. [72]. A $125\,\mu m$ thick PET foil was used as substrate. The active area of all devices was about $50\,cm^2$. All functional layers were prepared via mayer rod coating. Each layer was dried for 10 minutes under a hot air blower before the deposition of

the next layer. For the opaque back electrode a formulation of silver-graphite particles is used [98]. To enhance the transmittance and conductivity of the transparent electrode, silver nanowires (BASF SE), were used to replace the PEDOT:PSS electrode used previously by Schmidt et al. [72]. The results are shown in section 4.1. The ZnS particles to achieve either a green, blue or orange luminescence device were obtained from Leuchtstoffwerk Breitungen GmbH, Germany. Further details about the formulation of the ZnS dispersions used for the deposition of the light emitting layers can be found in the literature [72] (for a blue or green emission the ZnS is doped with different concentrations of copper (Cu), while for orange emission Manganese (Mn) is used as dopant). For the deposition of the dielectric layers a mixture of $35\,wt\,\%$ polyurethane (Tubicoat MEA from CHT R. Breitlich GmbH), $2wt\,\%$ dioctyl-sulfosuccinate-sodium-salt (Sigma Aldrich), and $5\,wt\,\%$ titanium-oxide dispersion (Kronos Titan GmbH) with $58\,wt\,\%$ H_2O to afford a wet layer thick-ness of $90\,\mu m$ was used.

3.2.2 Device Characterization

Standard sine waveforms ($500\,Hz$) supplied by a function generator (BMR, Folnet P and Folnet 1S) were used to operate the device. An additional $1\,kHz$ low pass filter allowed for a more precise measurement of the voltage supplied to the ACEL-devices. The luminance of the devices was measured with a luminance meter (Konica Minolta LS-110). The emitted spectrum was measured with a fiber coupled Ocean Optics HR4000 CG-UV-NIR high resolution spectrometer. The spectra were used to calculate the color coordinates of the emitted light in the CIE color. Cross sections were cut using a dual beam focused-ion-beam (FIB) instrument (FEI Helios Nanolab600i) equipped with a Ga-ion source. Cross sectional microstructural characterization were carried out by using a Phillips XL-30 SFEG scanning electron microscope.

3.3 Thin Film Solar Cells

3.3.1 Characterization of Solar Cells

The solar cells were characterized using a Keithley 2400 SMU and an AM 1.5 $100\,mWcm^{-2}$ simulated sunlight from a 300W Newport (Model 9116) solar simulator. The sunlight was calibrated with a certified IEC 60904-9 compliant reference silicon solar cell (Rera Systems). For measurements of the EQE spectra in this work a

homebuilt set-up was used. It contains a chopped tunable light source (LOT MSH 150) and a NF electronic instruments 5610B lock-in amplifier. For calibration, a Thorlabs PM100D power meter with a S130VC sensor head was used. The XRD measurements were performed with a Bruker D2 Phaser X-ray diffractometer using CuK_α radiation with a Lynx-Eye detector (step size 0.02° 2θ; integration time of 0.05 s).

3.3.2 Non-Fullerene Organic Solar Cells

The organic solar cells were soluion processed as reported in the literature [99]. The ZnO electron extraction layer was spin coated from ZnO nanoparticles (InfinityPV) on top of a cleaned ITO substrate. PBDB-T:ITIC (1:1 weight ratio) was diluted in 20 mg/ml chlorobenzene:DIO (99.5:0.5), and spin coated at 1000 rpm^{-1}. The MoO_3 and Ag layers were thermally evaporated at 10^{-6} $mbar$. The PEDOT:PSS (HTL-Solar, Heraeus) layers were spin coated at 3000 rpm^{-1}.

3.3.3 Perovskite Solar Cells

In the literature multiple robust process routes for perovskite solar cells are reported [100–103]. The devices used in this work up to the ALD layers have been entirely fabricated in a nitrogen filled glovebox. A PTAA (Sigma Aldrich) layer was deposited by spin-coating a 1.25 $mg\,mL^{-1}$ solution (in toluene) at 6000 rpm (750 $rpm\,s^{-1}$ acceleration) for 30 s followed by annealing at 120 °C for 30 min. The perovskite layer was deposited using the gas quenching procedure, as described in the literature [100]. Briefly, a solution of 0.9 M FAI (Greatcell), 0.06 M CsI (ultra-dry, Alpha Aesar), 1.05 M PbI_2 (ultradry, Alpha Aesar) and 0.1 M Thiourea (Sigma Aldrich, for seed management cite Hsieh2018) in 3:7 N-methyl-pyrrolidone (NMP): N,N-dimethylformamide (DMF) was spincoated at 3000 rpm (acceleration 300 $rpm\,s^{-1}$) for 120 s. After 20 s a nitrogen gas flow with 7 bar was directed at the substrate introducing the supersaturated phase, followed by a 20 min annealing step at 100 °C for the formation of the perovskite. Thereafter a PCBM (American Dye Source Inc.) solution 50 $mgmL^{-1}$ in chlorobenzene was spin coated at 1000 rpm (acceleration 750$rpms^{-1}$) for 30 s. An AZO nanoparticle dispersion (Avantama AG, N21x 2.5 $wt\%$ in a mixture of alcohols) was further diluted with isopropanol (ratio 1:2) and then spin coated at 4000 rpm (acceleration 700 $rpm\,s^{-1}$) for 30 s followed by a 30 min annealing step at 80 °C. For the depostion of the SnO_x layer, the solar cells were transferred into the ALD reactor (Beneq TFS-200) without inert break. The SnO_x layers were grown at 80 °C reactor tempera-

ture using tetrakis(dimethylamido)tin(IV) (Strem) from a 45 $^{\circ}C$ degree hot source and water from a liquid source at room temperature.

4

Electroluminescent Devices

This chapter describes the usage of Ag-NW in alternating current electroluminescent devices. A new device architecture is shown that is enabled by the usage of semi-transparent electrodes. I introduce a double-stacked ACEL-device layout that allows to operate the two emission zones of the devices individually. The resulting devices afford tunability of the emission color: orange - white - blue. By using semi-transparent bottom and top electrodes based on networks of Ag nanowires (Ag-NWs) a bifacial Janus-type emission of the devices is achieved, which adds a further degree of freedom in the design of ACEL applications. The main part of this chapter has been recently published in ACS Appl. Mater. Interfaces 2021, 13, 28514-28520 [104]. My contribution hereby was the conception and design of the experiments and the characterisation of the devices. The devices have been fabricated by "InovisCoat GmbH".

4.1 Key Requirements for Semitransparent Electrodes in Alternating Current Electroluminescent Devices

The layer structure of an ACEL-device is inherently suitable for large area, roll-to-roll processing on flexible substrates [45–48, 59]. While one of the electrodes can be made as an opaque electrode with any desired sheet resistance, the other electrode has to be semitransparent. The transmittance of the a semitransparent electrode is obviously important to maximize the light output of the device, whereas the sheet resistance requirement is depending on the dimensions of the device. The sheet resistance is less critical for small areas but crucial for large area devices.

Early roll-to-roll processed ACEL devices used PEDOT:PSS as semitransparent electrode material, which has some major disadvantages, such as acidity, hygroscopicity and batch-to-batch variation in electrical and physical properties [72, 105, 106]. At a sheet resistance of $300\,\Omega/sq$ the PEDOT:PSS layer offers a transmittance of only $55\,\%$. This still too high sheet resistance leads to an inhomogeneous luminance in larger area devices.

For the calculation of the electrical loss in the electrode due to the sheet resistance and thus the loss of luminance in the device, it is possible to describe the device as a series connection of RC circuits. As shown in Figure 2.5 the bottom electrode is contacted with an opaque busbar.

The ACEL-device can be considered to be homogeneous along the busbar. It can be described as a 1-dimensional device where a $1\,mm^2$ element represents one RC part. Figure 4.1 shows the equivalent circuit diagram of the large ACEL device as 1-dimensional device.

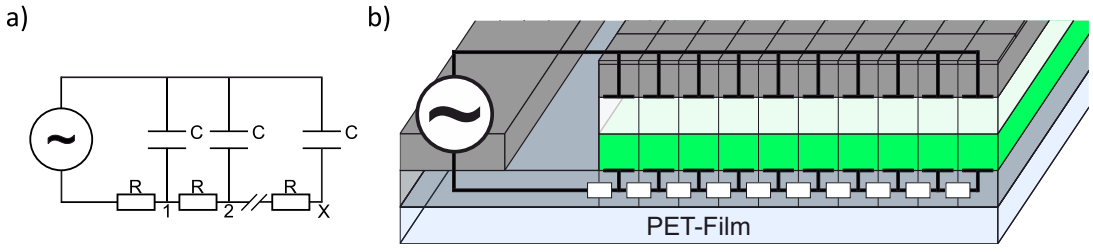

Figure 4.1: *a) Equivalent circuit diagram of the large ACEL device b) Drawn in the Structure of the device considered as 1-dimensional.*

Using this equivalent circuit, a simulation with the software *LTspice* can be carried out where X RC devices display the distance from the busbar in 1 mm steps. The resistance in this RC part is equal to the sheet resistance. The capacity was measured using an ACEL device with a precisely defined area.

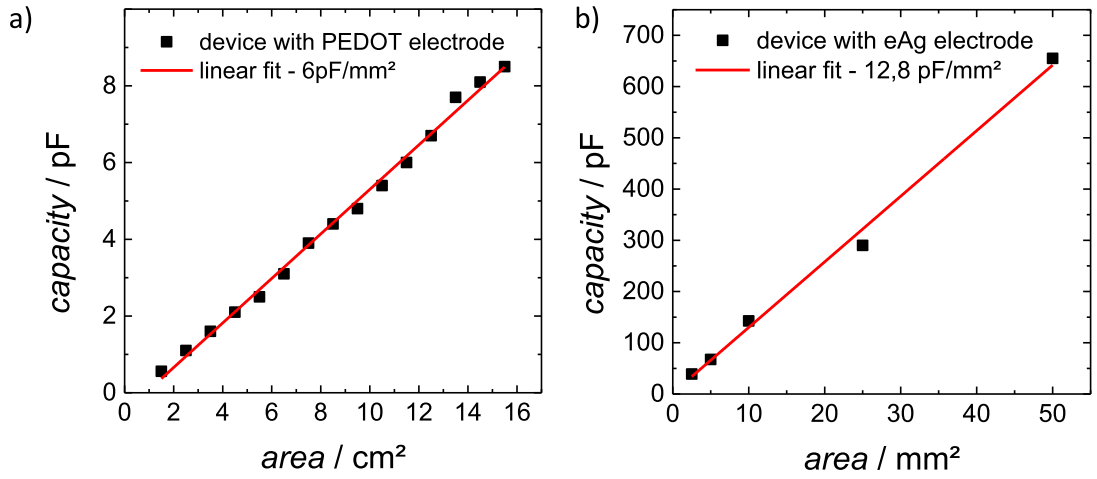

Figure 4.2: *Measurement of the ACEL devices with either a PEDOT:PSS or an evaporated silver electrode. The slope of the linear fit shows the capacity/mm^2 for the different setups. On average the ACEL device shows a capacity of* 10 pF/mm^2.

The capacity of an ACEL device with is between 6 and 12.8 pF/mm^2 as shown in Figure 4.2. Using the average of 10 pF/mm^2 for the 1 mm^2 large pieces it is possible to calculate the voltage at certain points in the device and therefore the voltage drop over the electrode and the drop in luminance, respectively. The results, shown in Figure 4.3, show that the sheet resistance of the device has a major impact on the voltage at the end of the device.

Due to the fact that the sheet resistance of PEDOT:PSS is relatively high even with a low transmittance of 55 %, it is desirable to use a different semitransparent electrode material. While ITO is mostly the material of choice when it comes to semitransparent electrodes, the deposition has to be done in a vacuum is not desired for large area, low cost roll-to-roll applications. In contrast, silver nanowires are highly compatible with roll-to-roll processes, and afford a wide window of sheet resistance/transmittance.

Figure 4.3 shows the luminance of the EL-device depending on the distance to the busbar at different voltages. As predicted in the simulation, the luminance for high sheet resistances decreases over the distance to the busbar. A device with an electrode with a high transmittance of 94 % shows significantly lower luminance than a device

with an electrode offering a lower transmittance but a lower sheet resistance as well. Furthermore, the luminance decreases by half with the course of 16 cm distance to the busbar. Even at the beginning of the device, 2 cm away from the busbar, the luminance is significantly lower. Notably the simulation predicts a higher drop in power and therefore in luminance. Nevertheless this simulation gives a general impression on the influence of sheet resistance for large area ACEL devices. For lower sheet resistances the luminance stays constant over the device. Therefore to aim at devices with a homogeneous luminance at higher areas the sheet resistance of the semitransparent electrode has to be lower than $100\,\Omega/sq$.

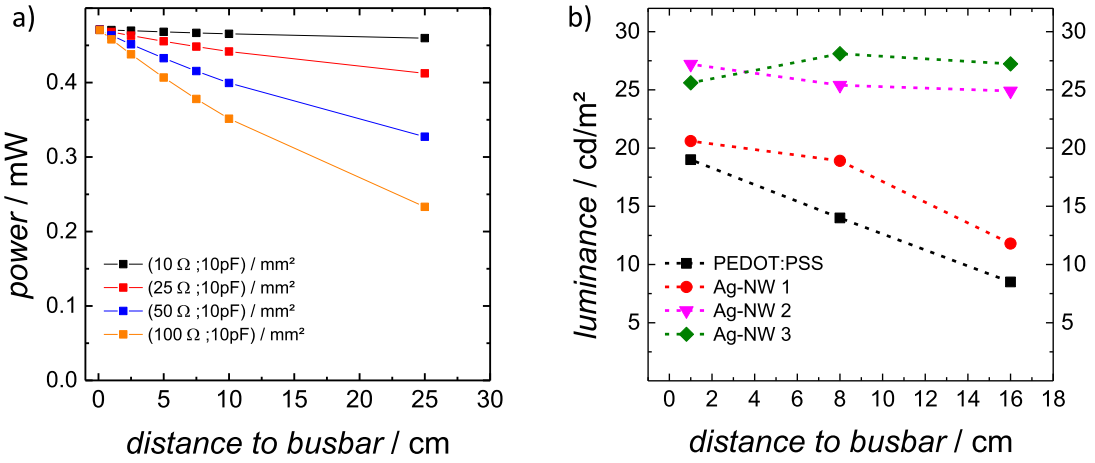

Figure 4.3: *a) Results for the simulation of the large area ACEL-device depending on the sheet resistance of the semitransparent electrode of the device. Plotted is the power ($U \cdot I$) in relation to the distance to the busbar of the device. b)Luminance of the ACEL-devices with different semitransparent electrodes in relation to the distance to the device of the device. Operated at 75 V 500 Hz.*

Table 4.1: *Figure of merit for all electrodes used in Figure 4.3.*

Electrode material	**Sheet resistance [Ω/sq]**	**Transmittance [%]**	**Figure of merit [Ω^{-1}]**
PEDOT:PSS	300 ± 10	55	$8.4 \cdot 10^{-6}$
Ag-NW 1	680 ± 30	94	$7.9 \cdot 10^{-4}$
Ag-NW 2	150 ± 15	88	$1.9 \cdot 10^{-3}$
Ag-NW 3	26 ± 2	73	$1.7 \cdot 10^{-3}$

The following investigations were conducted using the Ag-NW electrodes with a sheet resistance of $26\,\Omega/sq$ and a transmittance of 73 %.

4.2 New Electrode Materials for Alternating Current Electroluminescent Devices

To enhance the overall light output of an ACEL device, typical sources of loss have to be considered. Opaque electrodes based on silver-graphite particles absorb most of the light emitted towards them, due to their rough, dark surface. Therefore, two different approaches were carried out to mitigate such losses. The usage of an aluminium foil as a substrate offers a blank, reflecting surface and acts as a highly conductive electrode without any negative influence on the devices' homogeneity. With this reflecting electrode, a higher emission towards the semitransparent top electrode is expected. The second approach uses Ag-NW for both electrodes and therefore renders them both transparent. With this change the overall emission is expected to be doubled, due to the mitigated losses in the electrode or in the EL layer when reflected by the back electrode.

4.2.1 Inverted Layer Sequence on Aluminum Substrates

For the comparison of an ACEL-device on an aluminum foil substrate to a device with a graphite electrode, the stack architecture has to be inverted. A conventional device is deposited on a PET foil with a transparent electrode and an opaque electrode on top. If an aluminum substrate is used for the opaque electrode, the nanowire electrode has to be deposited on top of the device. In order to compare the luminance of a conventional ACEL-device with the layer sequence PET/Ag-NW/EL-Particles/dielectric/silver-graphite to an inverted structure with the layer structure PET/silver-graphite/dielectric/EL-Particles/Ag-NW devices using both architectures are fabricated (stack sequence is shown in Figure 4.4).

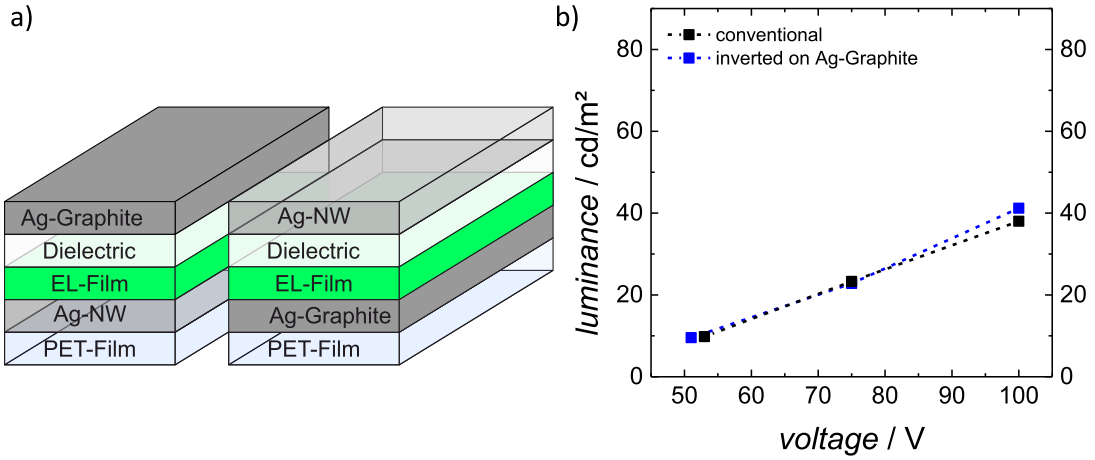

Figure 4.4: *Comparison between a conventional ACEL-device and an inverted layer sequence a) Schematic drawing of the layer sequences b) Luminance vs. voltage characteristics.*

As shown in Figure 4.4 the luminance of an inverted device is equal to the luminance of a conventional device. Therefore, it can be assumed that the layer sequence has no influence on the luminance of a device. In the next step, an inverted device was casted on top of an aluminum substrate and characterized. As shown in Figure 4.5 the overall luminance of an inverted device with a reflecting aluminum bottom electrode is 1.5 times higher than the luminance of a device with a graphite electrode. It can be assumed that both the high reflectance of the aluminum substrate is responsible for this higher luminance.

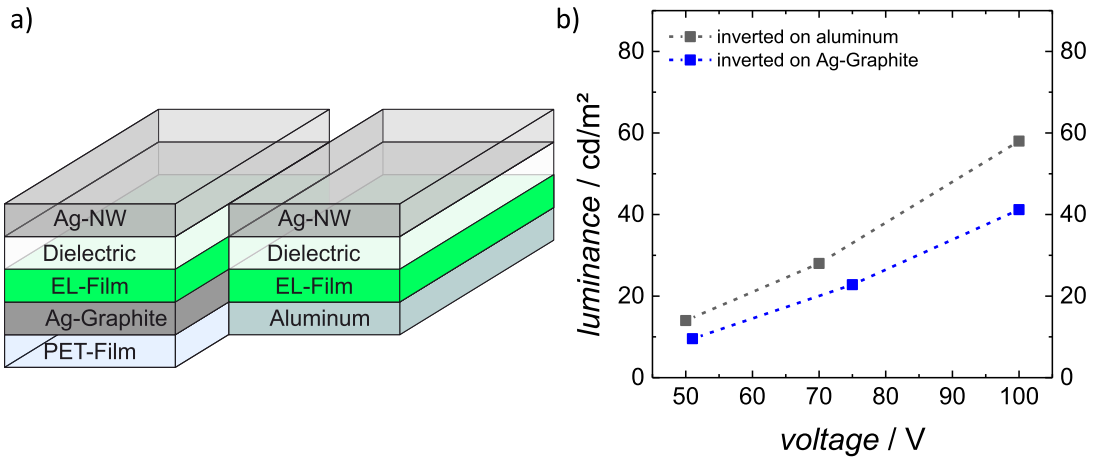

Figure 4.5: *Comparison of an inverted ACEL-device with Ag-Graphite electrode and an ACEL-device on aluminum substrate. a) Schematic drawing of the layer sequences b) Luminance vs. voltage characteristics.*

Thus, the usage of aluminum foil as substrates offers a promising base to increase the luminance of EL-devices.

4.2.2 Bifacial Device Architecture

The bifacial emitter device was the next architectural modification that was tested for its overall luminance. Hereby, both electrodes are made from Ag-NW and they are therefore semitransparent. Figure 4.6 shows the layer structure and the luminance of the devices that were compared.

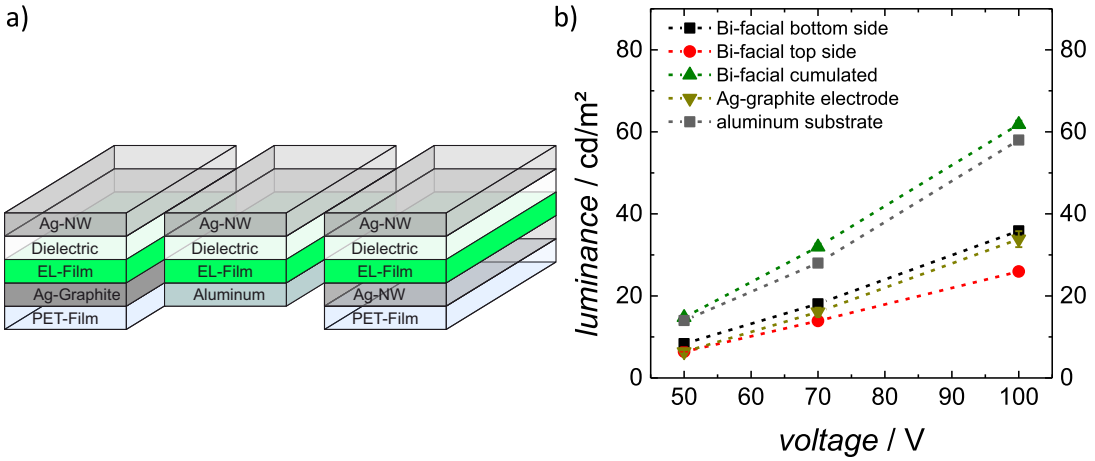

Figure 4.6: *Comparison of either side of the bifacial device with two Ag-NW electrodes, the cumulated luminance of the bifacial ACEL-device and the ACEL-devices with opaque aluminum or Ag-Graphite electrode. a) Schematic drawing of the layer sequences b) Luminance vs. voltage characteristics. Published in [104].*

The cumulated luminance of the bifacial devices reaches $61\,cd/m^2$ at $100\,V, 500\,Hz$. Thus, compared with both single sided devices, the bifacial device has an overall higher luminance than to devices with an opaque electrode. Nevertheless, the difference to the single sided device with an aluminum substrate is relatively small. To further investigate the losses inside the device, transmittance, reflectance and absorption of the dielectric layer, and the dielectric/EL-particle multilayer were measured. The losses are mostly due to the high reflectance of the dielectric interlayer and the low transmission of the EL-particles, as shown in Figure 4.7.

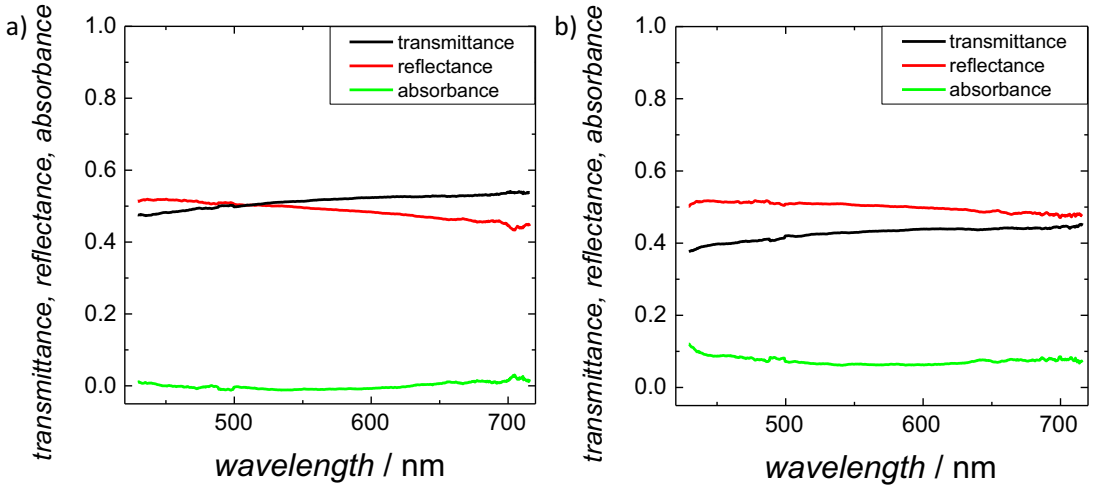

Figure 4.7: *Transmittance, reflectance and absorbance graph of the a) dielectric layer b) dielectric and EL-layer. Published in [104].*

The highly diffuse reflectance of the dielectric layer results from the composite of polyurethane and Titanium-oxide (TiO_2) particles. The high refractive index of TiO_2 provides this composite dielectric with a diffuse reflectance, as reported in a number of previous publications [107, 108]. In contrast to that there are numerous reports on semi-transparent ACEL-devices where the dielectric and light emitting layers were prepared by sputtering [109] or atomic layer deposition [110] affording smooth layers with a high specular transmittance.

The relatively high diffuse reflectance of the dielectric layer and EL-Layer severely limits the specular transparency of the bifacial devices which appear rather hazy translucent (Figure 4.8).

Figure 4.8: *Photograph of the bifacial ACEL-device placed on a computer screen which displays the logo of the University of Wuppertal. The device is clearly translucent with a high degree of haze. Published in [104].*

Notably the emission spectrum is not changing by the dielectric interlayer which is shown in Figure 4.9.

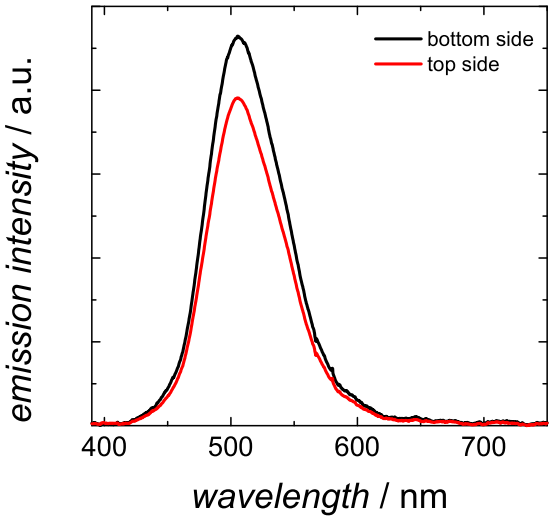

Figure 4.9: *Emission spectra of the bifacial device (using nanowires for both electrodes), measured from both sides. Published in [104].*

Nevertheless both architectural modifications increase the overall luminance by more than a factor of 1.5 and build a platform for further improvements of the devices.

4.3 Tandem Alternating Current Electroluminescent Devices

The results in section 4.1 pave the way to a new device architecture. Devices with Ag-NW top electrodes serve as building blocks to realize stacked devices with two emission layers. By casting a second ACEL-device on top of a device with Ag-NW top electrode, a tandem structure, using the middle electrode as joint electrode, is achieved enabling the individual operation of both sub-devices.

4.3.1 Green/Green Tandem Devices on Aluminum Substrate

To increase the luminance of the ACEL-device, a tandem structure, using the single device with aluminum electrode, was produced. Figure 4.10 shows the layer sequence and the resulting luminance/voltage graph.

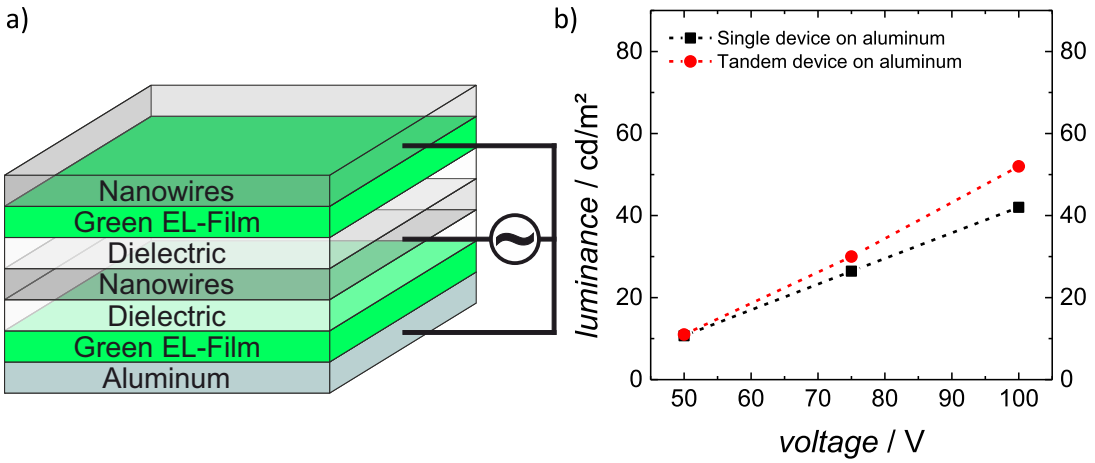

Figure 4.10: *a) Layer sequence and b) Luminance vs. voltage characteristics of the tandem device on aluminum substrate.*

Contrary to the expectation, the luminance is not increased by a factor of 2 but only by a factor of 1.25. It seems, that most of the light emitted by the bottom sub-device is absorbed by the upper EL-device. To further investigate the properties of a tandem stack, and the influence of a second ACEL-device on top of a first one, two green emitting ACEL-devices were stacked on top of each other with three Ag-NW electrodes (bottom, middle, top). The results are presented in the following section.

4.3.2 Green/Green, Bifacial Tandem Devices

To further investigate the layer sequence with three Ag-NW electrodes, a Focussed Ion Beam cut (FIB-cut) was performed, to look at a sharp cross section of the device. Figure 4.11 shows the resulting layer sequence of the device.

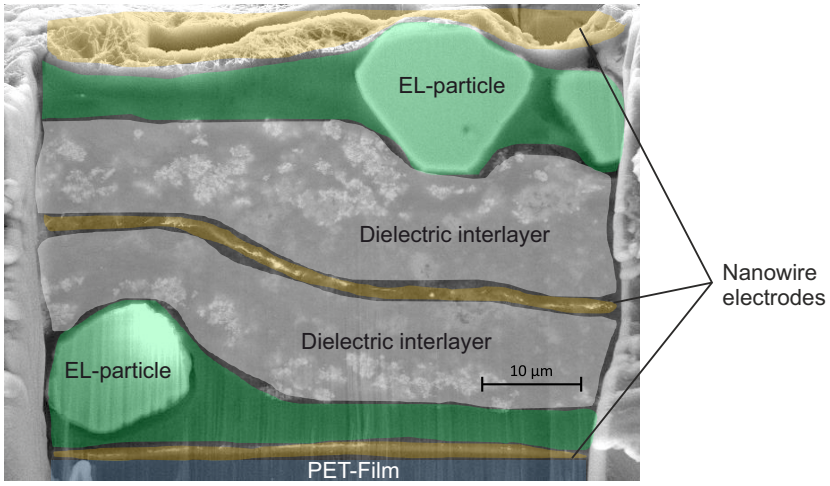

Figure 4.11: *Focused Ion Beam(FIB) cut of the green/green bifacial tandem device with three silver nanowire electrodes. Highlighted as following: PET substrate - light blue, Ag-NW electrode - orange, EL-Layer - green, dielectric layer - white. Published in [104].*

As marked in the image, the nanowire electrode (highlighted in yellow) is sandwiched by the two dielectric interlayers (highlighted in grey/white). The emitting layer (highlighted in green) consists of large EL-particles. To provide access to possible sources of optical losses in the tandem stack that may be related to (diffuse) reflectance and absorption in the various functional layers of the device, several experiments were designed. In the first test, both the top and bottom device were operated simultaneously with the same RMS-voltage $V_{top} = V_{bottom}$ at $500\,Hz$. As already seen for the tandem device on an aluminum substrate, only a $25\,\%$ increase of the luminance at $100\,V$ and $500\,Hz$ was found.

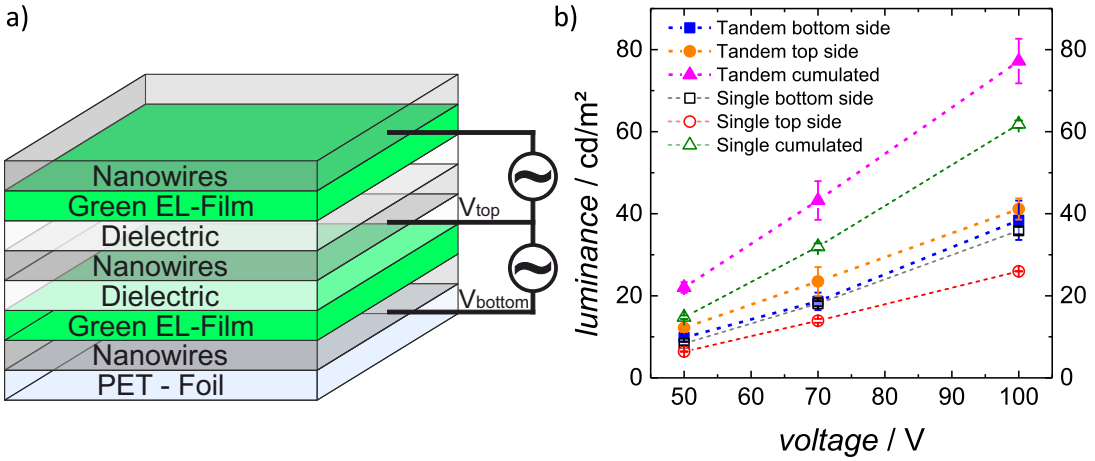

Figure 4.12: *a) Layer sequence and b) Luminance vs. voltage characteristics of the bifacial tandem device with all electrodes made from Ag-NW, compared to the single bifacial device. Published in [104].*

To better understand the origin of this lower than expected increase of the total luminance, the tandem device was further analyzed. At first the sub-devices were operated individually while the other one was left unbiased. Thereby, it is possible to determine the transmittance of the adjacent unbiased device for the light emitted by the operated device. All given cases for operation states and measurements are shown in Figure 4.13 as well as the results for this experiment.

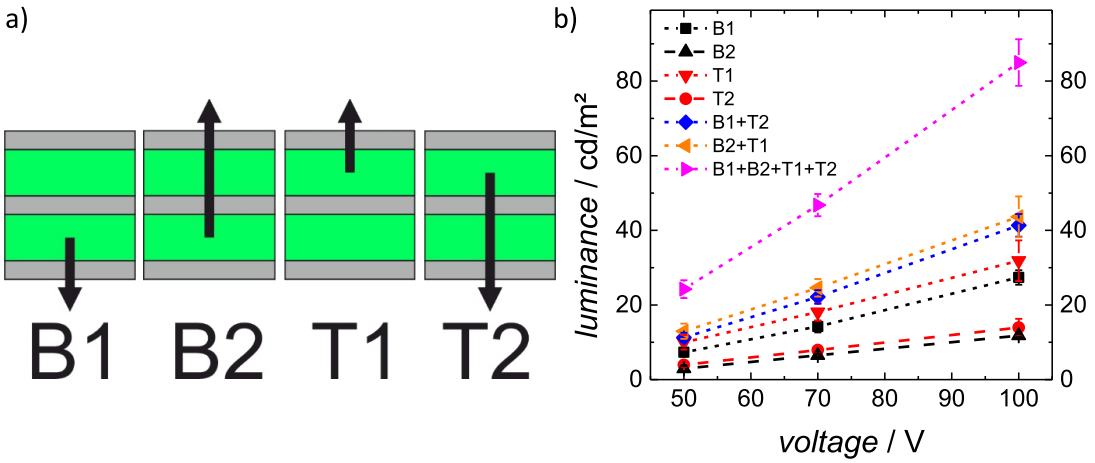

Figure 4.13: *a) Schematic and b) plots for all operation modes of the bifacial tandem device, operating only one sub-device and measuring from either side. Published in [104].*

As expected, the light that propagates through the adjacent (non-operated) device suffers notable losses. As an example, the luminance of the top device emitted via the

bottom electrode, with passage through the bottom device, is only around 40 % of the luminance emitted through the top electrode. The same applies to the luminance of the bottom device emitted via the top electrode. Owing to the notably diffuse reflectance of the layers, no specular reflectance or transmittance is measured in Figure 4.7, and the displayed graphs show 100 % diffuse values. As Fresnel calculations cannot be readily applied. Therefore in this case, a simplified transfer matrix model has been developed. The model is based on the transmittance of layers and layer stacks, which have been measured separately. Hereby the transmittance of the dielectric/EL-Layer stack has been as measured (spectra shown in Figure 4.7 b)), while the reflectance of the dielectric layer in contact with the bottom ACEL-device is considered unknown. A more detailed explanation of the model can be found in the appendix A.3. Using the measured luminance of the bottom device transmitted through the top device (In relation to the top emission in a single device the luminance in the stacked device is only 46 %.), the unknown reflectance and thus the absorption related to the EL-device has been calculated.

Using this model the transmission, absorption and reflection probability of photons by the layers of the adjacent sub-device have been determined to be 43 %, 5 %, and 52 %, respectively. Thereby the result, that 46 % of the light initially emitted by the bottom sub-device towards the top side is actually transmitted and emitted via the top electrode can be comprehended. Concomitantly, 25 % of this light emitted towards the top side is reflected and emitted through the bottom side, and 29 % are ultimately absorbed. These values do not depend on whether the top sub-device is operated or not, as can be extracted from the comparison of Figure 4.12 b) and 4.13.

4.3.3 Orange/Blue, Bifacial Tandem Devices

Notwithstanding the previous discussion of apparent optical losses, stacked ACEL-devices provide an attractive avenue to achieve versatile color tunability. To this end, tandem structures containing a blue and an orange emitting sub-device are designed and fabricated. The layer structure is illustrated in Figure 4.14. In a similar sense as before, initially either the blue or the orange sub-device has been operated, and the respective luminance vs. voltage characteristics has been measured. For the reasons discussed in section 4.3.2, the passage of the generated photons through the adjacent (non operated) sub-device is subject to notable optical losses. Figure 4.14 shows the luminance vs. voltage characteristics for both sub-devices, operated individually, measured from either side.

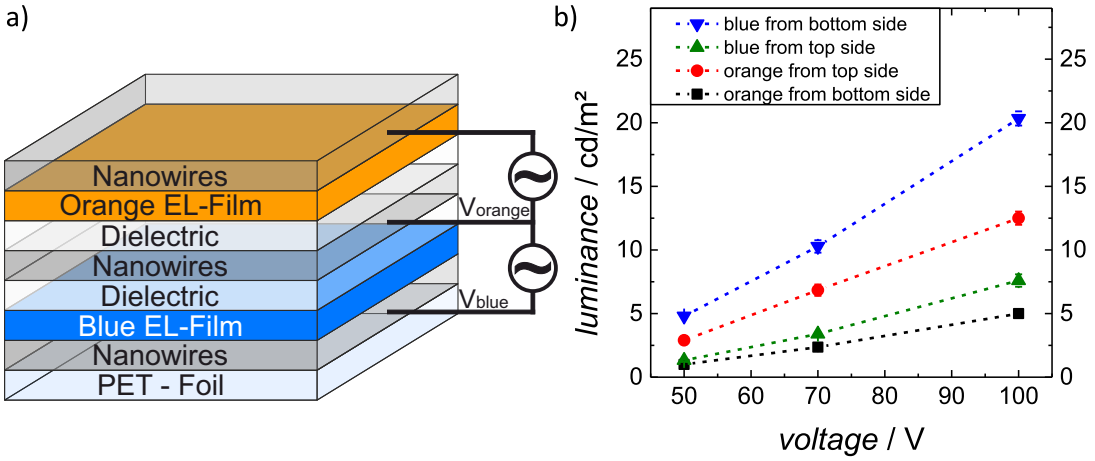

Figure 4.14: *a) Schematic drawing and plot of the bifacial tandem device with blue and orange emitting layer. b) Luminance vs. voltage plot operating only one device while measuring the luminance from either side. Published in [104].*

Both emission spectra of the blue and orange device are shown in Figure 4.15. The blue and orange emission spectra are peaked at 495 nm and 585 nm, respectively, and their shapes agree with reports in the literature for the respective phosphors [111, 112]. Hereby it is important to note that both emission spectra remain unaltered regardless if observed from the top or bottom side of the device. The spectra are shown in Figure 4.15.

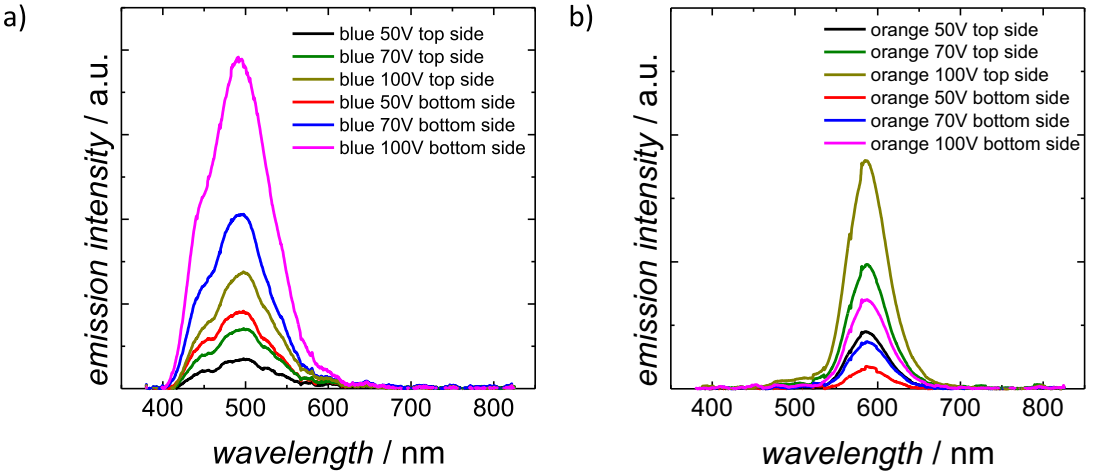

Figure 4.15: *Emission spectra of the blue and orange sub-devices operated with the other sub-device unbiased at different voltages. a) blue sub-device b) orange sub-device. Published in [104].*

It is obvious, that all spectra from top and bottom side at any voltage show the same peaks at 495 and 585 nm. Notably the luminance levels of the blue sub-device are

about a factor of two larger than that of the orange device, under the same conditions of operation. This is inherent to the different efficiency of the respective blue/orange phosphors, as reported in the literature [46]. In the next step, both sub-devices are operated at the same time. Hereby the luminance emitted from the top and bottom electrode is measured respectively. The operation voltage of the orange device is varied, while that of the blue device is keep constant at $50\,V$, $70\,V$ or $100\,V$.

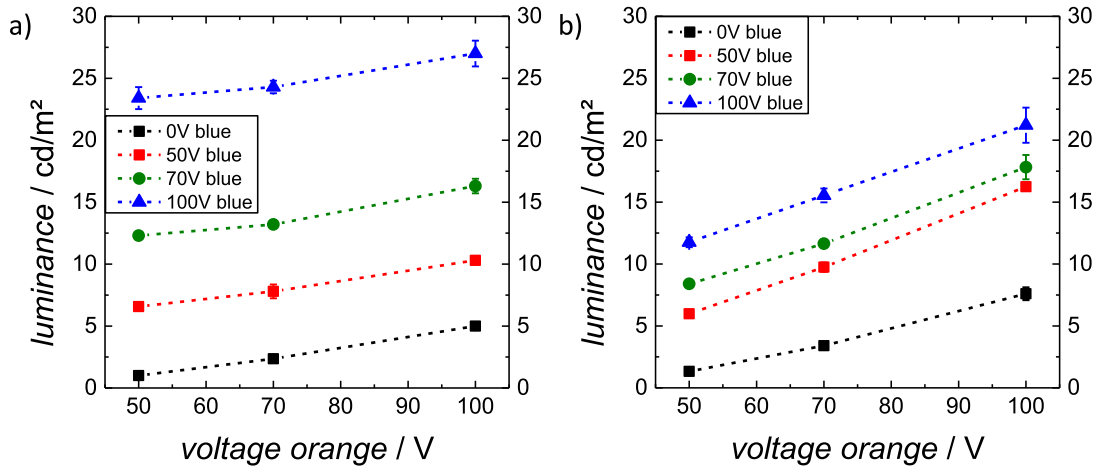

Figure 4.16: *Luminance of the bifacial blue/orange tandem device measured from either side. Bias voltage of the orange sub-device is varied between 50 V and 100 V @ 500 Hz while keeping the blue sub-device constant at 0 V, 50 V, 70 V and 100 V a) Measured from the blue side b) Measured from the orange side. Published in [104].*

The corresponting spectra for all shown voltage combinations can be found in the appendix Figure A.1. To achieve white emission, both blue and orange spectral contributions need to be properly balanced. The color coordinates of the light, emitted by the tandem ACEL-device from the respective spectra can be calculated as described in 2.3.2. With the resulting x and y coordinates each spectrum can be placed in the CIE chart as shown in Figure 4.17.

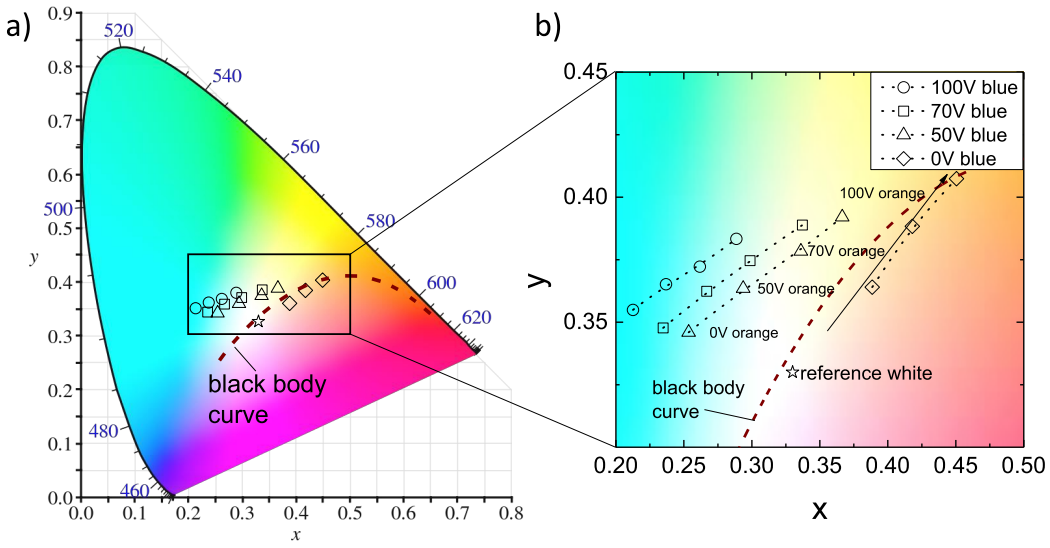

Figure 4.17: *a) CIE diagram of the blue/orange tangem ACEL-device. Color coordinates of all in Figure 4.16 shown setups measured from the top side. b) Zoomed in to the relevant area. The black body curve as well as the reference white point (0.33/0.33) are marked aswell. Published in [104].*

Due to the higher luminance of the blue sub-device, the bottom emission is generally dominated by spectral components emitted by the blue sub-device, as shown in Figure A.2 in the appendix. Therefore the emission from the top side allows for a more favorable balance of blue and orange due to the preferred out-coupling of the orange spectral components via the top electrode. Figure 4.17 shows the color tunability of the emission perceived via the top electrode with additional exemplary emission spectra. The shown spectra are located near the so called "Planck locus" denoting the color coordinates of a black body radiator of varied temperature and therefore perceived a white light by the human eye. Figure 4.18 shows two exemplary emission spectra for the most white color impressions.

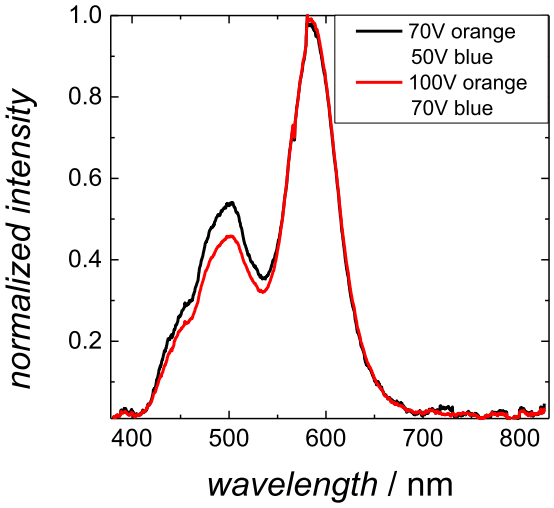

Figure 4.18: *Normalized emission spectra of the blue/orang tandem ACEL-device measured from the top side at two voltage configurations. The shown emission spectra are the ones that are closest to a color impression that can be assigned to the color temperature "warm white". Published in [104].*

Based on these emission spectra, the color temperature can be derived as reported in the literature [74]. For the operation of the blue device at $70\,V$ and $100\,V$ for the orange device, a color temperature of $5346\,K$ respectively $5375\,K$ for $50\,V$ blue and $70\,V$ orange can be derived.

Figure 4.19 shows photographs of the light emission from the top/bottom side at selected bias settings.

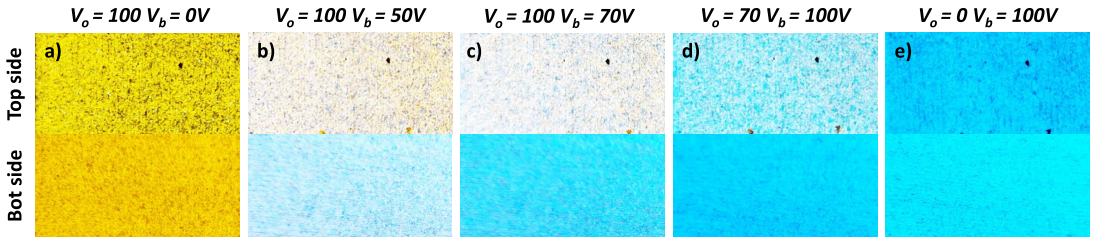

Figure 4.19: *Photographs of the blue/orange tandem ACEL-device at certain voltage ratios taken from both sides (500 Hz). a) Shows the orange sub-device at 100 V with the blue device at 0 V. b) Shows the orange sub-device at 100 V with the blue sub-device at 50V. Its visible, that even at a low Voltage the blue sub-device dominates from the bottom side, while shifting the color impression from the top side to a white color impression. c) Shows the highest luminance while still reaching a white color impression from the topside ($V_{orange} = 100\,V; V_{blue} = 70\,V$). From the bottom side the blue sub-device completely dominates the color impression. d) Shows how a further increase of the blue sub-device's voltage to 100 V while lowering the voltage of the orange sub-device orange device to 70 V. e) Shows the blue sub-devices voltage at 100 V with the orange sub-device unbiased. Published in [104].*

These results demonstrate the facile voltage controlled color tunability of the tandem ACEL-devices. The Janus-type character, i.e. different color of top and bottom emission of the bifacial devices opens interesting opportunities for signage applications.

4.4 Conclusion

In summary the necessity of low sheet resistance electrodes for large area ACEL-devices has been shown. Furthermore, a novel ACEL-device architecture that allows for facile color tunability was demonstrated. Specifically, a three-terminal tandem device with monolithically stacked orange and blue sub-devices that can be individually operated to tune the emission color was introduced. Moreover, semitransparent bottom and top electrodes based on networks of silver nanowires afford bifacial Janus-type emission. A detailed analysis of the sources of optical losses in single and tandem ACEL-devices was provided. In contrast to previously published concepts where the luminance for certain colors can not be changed, the three terminal tandem allows for color tuning independent of the luminance. The three terminal tandem allows similar emission spectra with higher luminance, keeping the voltage ratio at the same level while increasing the amplitude of both emission zones. Therefore, the three terminal tandem presented here offer major advantages over the reported ones in the literature. It can be anticipated that the devices proposed in this work will inspire further developments in the field of ACEL-devices for novel applications in signage and lighting. In general, the results act as a proof of-concept that provides ample space for improvements, predominantly with respect to more efficient orange phosphors, the use of dielectric materials with a high transmittance and the possible combination of other colors in the sub-devices.

5

Semitransparent Organic Solar Cells

Organic solar cells have shown a huge potential as renewable energy source, especially in terms of simple fabrication techniques, mechanical flexibility and low weight. [113–116]. A notable characteristic of organic solarcells is their general semitransparency, if equipped with semitranspatent electrodes [6]. This allows for applications as energy harvesting windows for buildings, automobiles, fashion and architecture. As a common layer structure, organic solarcells are processed on a substrate with a semitransparent electrode (typically ITO), ending with a reflecting metal electrode which renders the entire device opaque [117]. To achieve a semitransparent device the top electrode has to semitransprent as well, e.g. a thin metal electrode [4, 118–122] or a silver nanowire electrode [123–125]. By the introduction of non-fullerene acceptors for organic photovoltaics a new level of efficiency was achievable as discussed in section 2.5.1. At that time PBDB-T in a bulk hetero junction with the acceptor molecule ITIC paved the way for organic single junction solar cells with an efficiency of 11.21 % [80], and is therefore as active material used in this work. At the time this work was conducted, there were already reports on semitransparent devices utilizing a molybdenum oxide (MoO_3)/silver/MoO_3 layer structure as semitransparent electrode [4], but no reports could be found on non-fullerene solar cells with solution processed silver nanowire electrodes, which would enable fully solution processed devices. This chapter will show semitransparent non-fullerene solar cells based on the PBDB-T:ITIC bulk

hetero junctions. At first, the thermally evaporated MoO_3 is replaced with liquid processed PEDOT:PSS comparing opaque devices with either MoO_3 or PEDOT:PSS as hole extraction layer. In a next step, semitransparent devices using the established MoO_3/Ag/MoO_3 electrodes are shown. Ultimately the thermally evaporated silver electrode is replaced by a spray coated nanowire electrode, resulting in the, at that time, first non-fullerene, semitransparent solar cells with fully liquid processed semitransparent top electrode. Previous work on semitransparent devices with non-fullerene acceptor solely use thermally evaporated electrodes which disqualifies this layer sequence for vacuum free liquid processing [4]. Figure 5.1 shows a schematic drawing of the general device architecture. The layer sequence including the bulk hetero junction is hereby the same for all used devices. Merely the hole extraction layer and the top electrode is varied in the following sections.

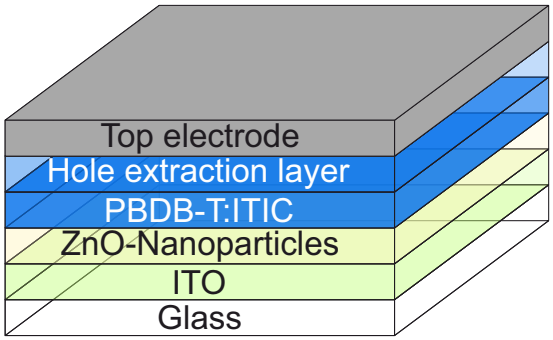

Figure 5.1: *Schematic drawing of the non-fullerene solar cell stack used as a platform in this chapter. The focus hereby is laid on the hole extraction layer on top of the bulk hetero junction and the top electrode.*

5.1 Evaporated Molybdenum Oxide and Liquid Processed PEDOT:PSS

Thermally evaporated MoO_3 is frequently used as hole extraction layer on top of organic solar cells [126]. To avoid the complex vacuum processing of MoO_3 it can be replaced by the solution processable PEDOT:PSS. Even if PEDOT:PSS brings some well known disadvantages in regards to stability it is likewise readily available and suitable for upscaling. Reported problems regarding the acidity of PEDOT:PSS can be avoided by using a special formulation called "Clevios™ HTL-Solar" by Heraeus [127–129]. As HEL MoO_3 and "Clevios™ HTL-Solar" will be used on top of solar cells, at first in opaque devices with evaporated Ag-electrode. Regardless of the slightly different EQE characteristics of the respective devices due to the different optical properties of MoO_3

and PEDOT:PSS, the PCE of is just slightly below 10 % for both devices which offers an encouraging platform for semitransparent OSCs.

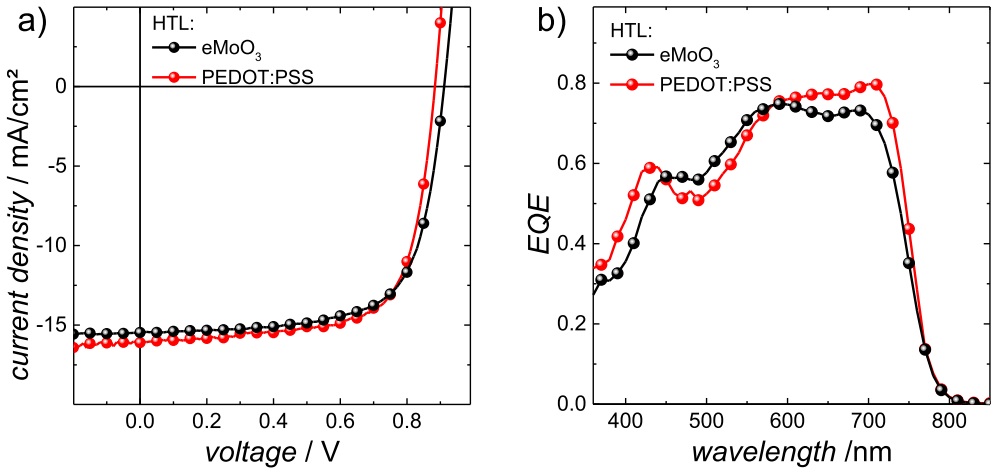

Figure 5.2: *J/V (a) and EQE (b) characteristics of opaque organic solar cells using PEDOT:PSS and $eMoO_3$ as extraction layer.*

Table 5.1: *Full device characteristics of opaque and semitransparent organic solar cells using $eMoO_3$ as extraction layer and 100 nm thermally evaporated silver for the opaque, and 7 nm evaporated silver for the semitransparent device.*

	PCE [%]	**FF** [%]	$\mathbf{V_{OC}}$ [V]	$\mathbf{J_{SC}}$ [$\mathbf{mA/cm^2}$]
MoO_3 / 100nm eAg	9.8	70	0.91	15.4
PEDOT:PSS / 100nm eAg	9.9	70	0.88	16.1

5.2 Semitransparent Solar Cells Using Molybdenum Oxide

To achieve a semi transparent OSC, the top electrode has to be modified. It is reported, that by sandwiching a thin $7\,nm$ Ag-electrode with two metal oxide layers a semi transparent electrode can be achieved [4]. The transmittance of the semitransparent device can be optimized by an optical simulation of the layer sequence, and by adjusting the thickness of the top MoO_3 layer. Therefore a simulation with the software SETFOS (Fluxim AG) has been carried out, and the optimal layer thickness has been determined to $7\,nm$ of Ag and $10\,nm$ for both MoO_3 layers. The resulting device characteristics are illustrated in Figure 5.3.

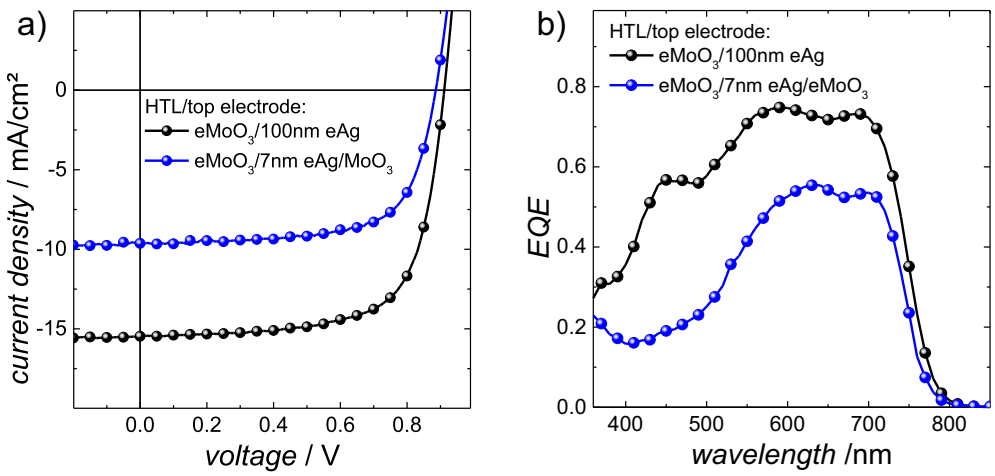

Figure 5.3: *J/V (a) and EQE (b) characteristics of opaque organic solar cells using $eMoO_3$ as extraction layer and a thermally evaporated silver electrode.*

Compared to the opaque device, the short circuit current density in the semitransparent device is 38 % lower. While still achieving a PCE of over 5.5 % the average transmittance of the device still attains 45 %, which is responsible for the lower current density. The literature shows similar results using slightly different active materials or top electrodes [4, 119, 120]. By further improving the active materials Jiang et al. showed semitransparent solarcells with an average transmittance ot 36.2 % and a PCE of 8.1 % using PTB7-Th:IEICO-4F and a transmittance of 28.6 % with a PCE of 10.2 % using a ternary blend of $PM6 : Y6 : PC_{71}BM$ [121]. The $PM6 : Y6 : PC_{71}BM$ blend was further improved by Lu et al. by replacing the $PC_{71}BM$ with a non-fullerene acceptor $DIBC$ achieving a transmitance of 21.6 % with a PCE of 14 % [122], showing the enormous progress that was made in the meantime.

Table 5.2: *Full device characteristics of opaque and semitransparent organic solar cells using $eMoO_3$ as extraction layer and 100 nm thermally evaporated silver for the opaque, and 7 nm evaporated silver for the semitransparent device.*

	PCE [%]	**FF** [%]	$\mathbf{V_{OC}}$ [V]	$\mathbf{J_{SC}}$ [$\mathbf{mA/cm^2}$]
MoO_3 / 100nm eAg	9.8	70	0.91	15.4
MoO_3 / 7nm eAg / MoO_3	5.8	68	0.89	9.6

While these results are promising for a semitransparent OPV-structure, the semitransparent electrode layer sequence is deposited in high vacuum which renders them not

suitable for low cost roll-to-roll processes. Therefore a different material is desired for the semitransparent electrode.

5.3 Fully Solution Processed Semitransparent Solar Cells

As discussed earlier, most reports on semitransparent devices utilize evaporated electrodes. Opposed to that Silver nanowires are a frequently used semi transparent electrode material casted from liquid phase. By spray coating the nanowires on top of the device stack, the whole device is processed from commercially available, liquid processed materials, which was unprecedented for non-fullerene solar cells at that time.

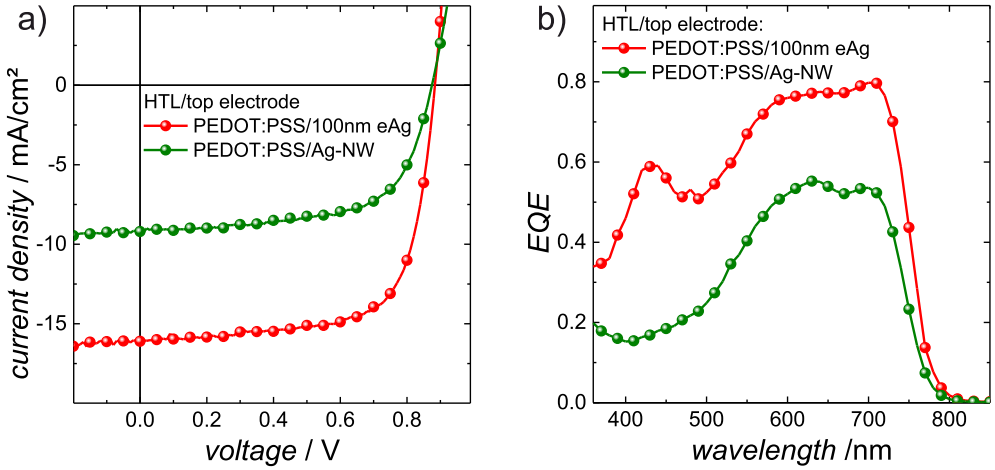

Figure 5.4: *J/V (a) and EQE (b) characteristics of opaque organic solar cells using PEDOT:PSS as extraction layer and 100 nm thermally evaporated silver for the opaque, silver nanowires for the semitransparent device.*

Table 5.3: *Full device characteristics of opaque organic solar cells using PEDOT:PSS as extraction layer and 100 nm thermally evaporated silver for the opaque, silver nanowires for the semitransparent device.*

	PCE [%]	**FF** [%]	$\mathbf{V_{OC}}$ [V]	$\mathbf{J_{SC}}$ [$\mathbf{mA/cm^2}$]
PEDOT:PSS / 100nm eAg	9.8	70	0.88	16.1
PEDOT:PSS / Ag-NW	5.1	64	0.87	9.2

For the solar cells a semitransparent electrode with a sheet resistance around $16\,\Omega/sq$, and therefore comparable to the ITO electrode, was chosen, and therefore a transmit-

tance of around 72 % could be acquired. As shown before, the change from MoO_3 to "Clevios™ HTL-Solar" PEDOT:PSS shows no negative influence on the device characteristics. Using Ag-NW instead of evaporated silver layers leads to an overall lower PCE of 5.1 %. The average transmittance of such a fully liquid processed OSC is around 37.5 % in the visible spectrum. The lower overall efficiency with a lower transmittance is mostly to the lack of optical tuning which can not be done like with the metal oxide/silver/metal oxide layer structure and the higher series resistance in the silver nanowire electrode. The larger difference in fill factor can be derived from the first quadrant of the J/V characteristics. Figure 5.5 shows a zoom in to the first quadrant of the J/V characteristics of all shown devices. As pictured in Table 5.2 the difference in fill factor for the semi transparent device with thermally evaporated MoO_3 to the opaque one is not significant. Also the J/V characteristics in Figure 5.5 a) show a similar behaviour. Opposed to that the fill factor for the semi transparent device using PEDOT:PSS and the silver nanowire electrode is lower. The J/V characteristics in the first quadrant show a clear sign for a higher series resistance for the device with Ag-NW electrode as discussed in figure 2.7 and reported in the literature [130]. Extracting the series resistance from the J/V characteristics shows, that the series resistance for the semitransparent device with evaporated electrode is higher by a factor of 1.5 while the series resistance of the Ag-NW device is higher by a factor of 3 compared to the opaque device with PEDOT:PSS HTL.

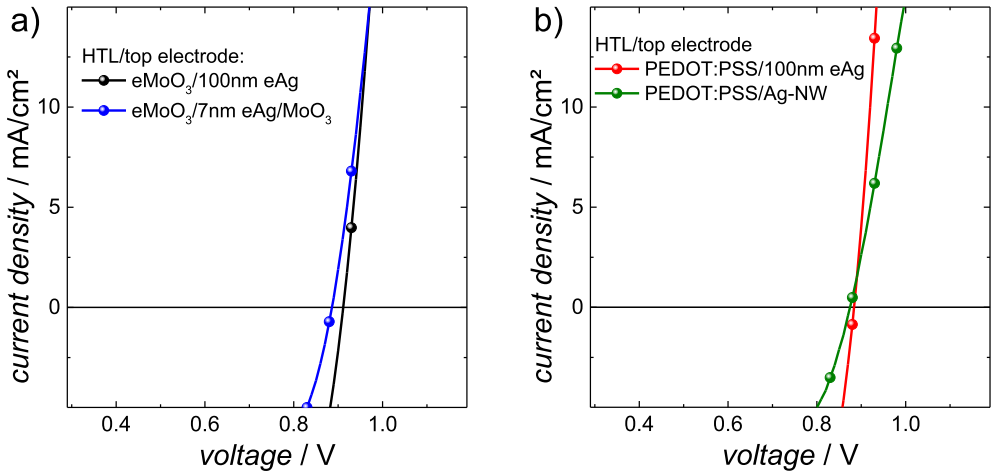

Figure 5.5: *J/V characteristics of organic solar cells using a) $eMoO_3$ or b) PEDOT:PSS as extraction layer. The axis range was zoomed in to the first quadrant to show the influence of the series resistance.*

To decrease the series resistance, without lowering the transmittance, it is possible to decrease the contact resistance between the single nanowires via annealing as discussed earlier [93, 95]. Another approach that was made in the past, is the filling of gaps with conductive oxides to enhance the extraction between the nanowires and the overall conductivity of the Ag-NW electrode [41]. The transmittance spectra and a photography of an exemplary device is shown in Figure 5.6.

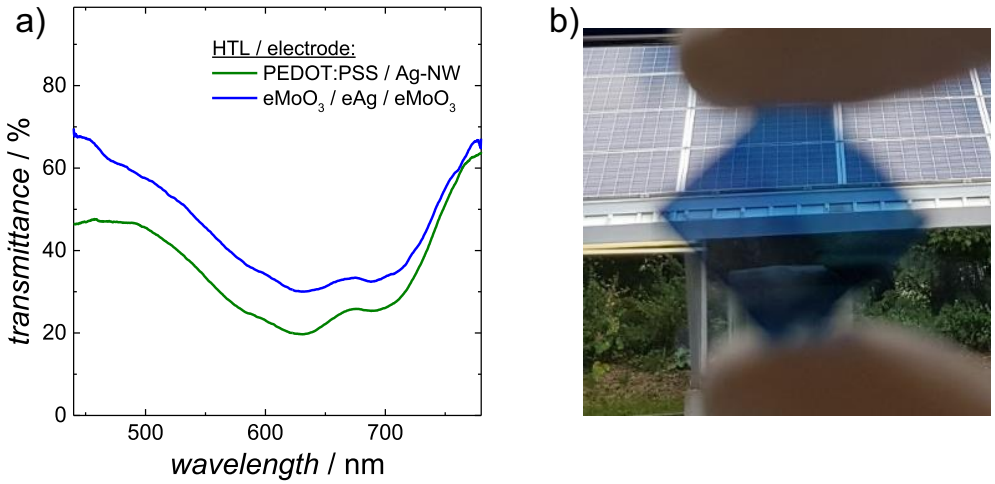

Figure 5.6: *Transmittance spectra (a) and photograph (b) of the semitransparent devices. The image shows a full area device using silver nanowires as an electrode. It has to be noted, that the higher transmittance for the device affording the higher PCE is solely due to the optical tuning of the metal oxide/metal/metal oxide layer structure.*

Still these results show the possibility of using liquid processable and highly available materials for roll-to-roll processable OSCs. Comparing the results presented in this chapter to the literature shows, that these results surpass previous work in terms of efficiency and/or transmittance, (Figure 5.7). Other reported devices with silver nanowire top electrode such as Lu et al. [124] use a similar layer sequence, with lower efficient active materials and an inkjet printed silver nanowire electrode, which show much lower efficiencies, due to the chosen active material.

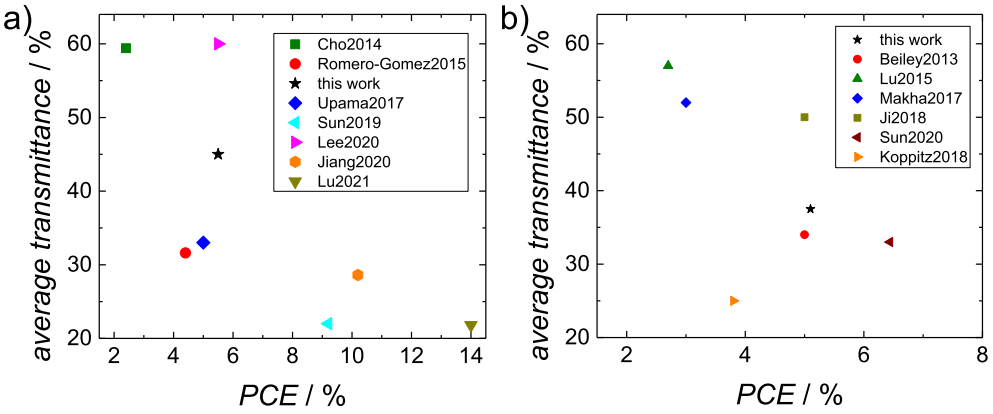

Figure 5.7: *Comparison of semitransparent organic solar cells in the literature with a) All shown devices use thermally evaporated electrodes. Note that the solar cells reported in [119–122] are based on higher efficient polymers. Solar cells reported in [131, 132] are fullerene based bulk hetero junctions b) All shown devices use solution processed silver Nanowire electrodes [123–125, 133–135].*

5.4 Conclusion

In summary this chapter showed the transition from an opaque organic solar cell to a semitransparent solar cell by replacing the thick silver electrode by a 7 nm thick silver layer and a 10 nm MoO_3 layer to enhance the transmission of the device stack. The shown devices line perfectly with previous and recent publications. Furthermore, by replacing the thermally evaporated MoO_3 electrode and using spray coated silver nanowires, an all solution processed device that surpasses even recent publications in terms of efficiency was introduced. The immense potential of organic solar cells using non-fullerene acceptors is shown in the literature, where organic solar cells with a PCE of over 18 % are reported in 2021 [86]. With these results the proof of concept was provided for the fabrication of non-fullerene solar cells completely via solution processable, roll-to-roll compatible materials at atmospheric pressure which was unprecedented at the time this work was conducted.

6

Semitransparent Perovskite Solar Cells

The content of this chapter has already been published in Adv. Energy Mater. 2020, 10, 1903897 [97]. My contribution has been the fabrication, and characterisation of the electrodes, test devices and the overall investigation of the interface effects. Kai Oliver Brinkmann has contributed the perovskite solar cells expertise.

In recent years perovskite solar cells have seen a remarkable increase of cell efficiency [136]. As discussed earlier, PSCs require semitransparent top electrodes in cases, where building integration (windows), multi-junction architectures, or opaque substrates (i.e., top-illuminated devices) are envisaged. As mentioned in Section 2.1.2 the most widely established semitransparent electrodes based on ITO are prepared by sputtering followed by a high-temperature annealing step (around $450\,^{\circ}C$) to achieve a high optical transmittance paired with a low sheet resistance. As semitransparent top electrode for a PSC, annealing temperatures in excess of $100\,^{\circ}C$ would thermally decompose the perovskite. Therefore silver nanowire networks are a promising alternative semitransparent electrode, that can be processed at low temperature from liquid dispersions. Although Ag-NW are mostly casted from alcoholic dispersions, water is an especially favorable dispersing medium as it is environmentally friendly and does not impose safety concerns typically associated with alcohols, such as flammability. Unfortunately water is a widely known threat to the stability of lead-halide perovskites [22–24]. Therefore, a

protection layer would be required, that simultaneously forms an electronic interface between the device and the Ag-NW electrode, which is why well established but electrically insulating permeation barriers like Al_2O_3/TiO_2 cannot be used [137]. On the other hand electron transport layers grown by ALD have been integrated into PSC device stacks to protect the perovskite against the detrimental impact of ambient gases or high-energy particles of sputtering processes [26, 138–140]. In this chapter these impermeable electron transport layers are shown to unlock the opportunity to spray coat a semitransparent Ag-NW electrode from an aqueous dispersion on top of the PSC device stack without detrimental impact on the perovskite active layer.

Device Characteristics

To compare the results of the PSCs with a solution processed semitransparent electrode, p-i-n perovskite solar cells with opaque 100 nm silver electrode were fabricated as presented in the experimental in section 3.3.3. As shown in Figure 6.1 a) and Table 6.1 the reference cells show a high PCE above 18 % with a low hysteresis. A short circuit current density of 23 mA/cm^2 has been measured via EQE measurement.

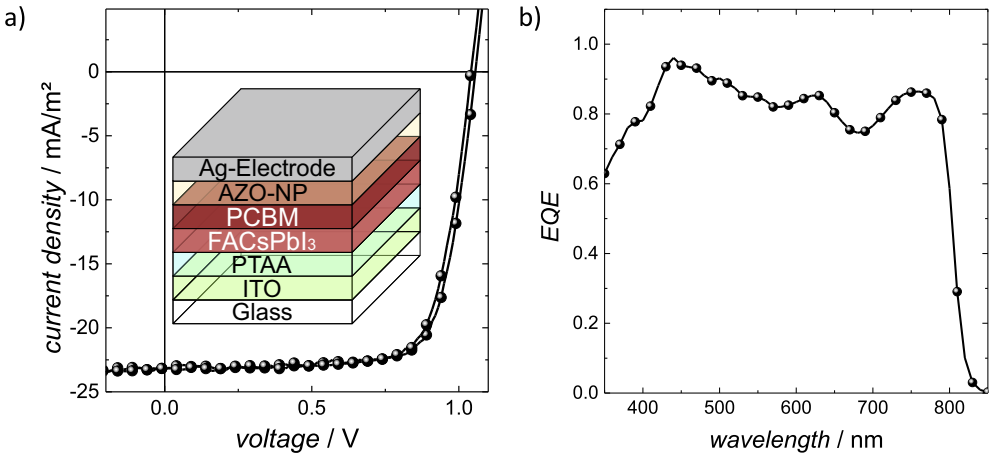

Figure 6.1: *J/V (a) and EQE (b) characteristics of a reference perovskite solar cell with 100 nm thermal evaporated silver electrode. Published in [97].*

Table 6.1: *Full device characteristics of a reference perovskite solar cell with 100 nm thermal evaporated silver electrode [97].*

	PCE [%]	**FF** [%]	**V_{OC}** [V]	**J_{EQE}** [mA/cm^2]
rev.	18.4	75	1.06	23.0
forw.	18.1	75	1.04	

In the following sections these PSCs act as a platform to evaluate the performance of the semitransparent nanowire elecrodes, and to detect potential harm to the PSC due to the deposition process.

6.1 Influence of Water on $FACsPbI_3$ Perovskite Layer

As described earlier, a deposition of silver nanowires from an aqueous dispersion is highly preferred. Unfortunately, perovskites tend to decompose in the presence of water, which leads to the full loss of the much desired photovoltaic characteristics [22–24]. To verify the detrimental influence of water exposure on the perovskite solar cell, and therefore to show the critical necessity of a protection barrier, a $FACsPbI_3$ solar cell, without top electrode, was deposited on full area substrates (see Figure 6.2 a)). To simulate a watery deposition process on the perovskite layer, a drop of water was placed on top of the layer stack. Figure 6.2 b) shows the $FACsPbI_3$ exposed to the water drop. As clearly noticeable the active layer changes its color significantly after being exposed to the water. Such altering in color can be traced back to the formation of PbI_2 in interaction with water which was also verified by XRD measurements (Figure 6.2 c)). Therefore a water based processing on top of such an unprotected cell would lead to a definitive change in characteristics and thus to no functional perovskite solar cell. To enable water based processing nonetheless, a protective barrier is of critical importance. As has been shown in earlier work, ALD-grown tin oxide (SnO_x) is capable of protecting perovskite solar cells against moisture, and hence leads to a significant increase in stability, whilst not altering the solar cell properties [26]. As a consequence, a $20\,nm$ SnO_x layer was established as a protective interlayer for the subsequent aqueous deposition of Ag-NWs. The same experiment, exposing the layer sequence to a drop of water, to verify the protective properties of the SnO_x layer was carried out. As shown in Figure 6.2, no change in color of the $FACsPbI_3$ occurs. To further examine the influence of water on the encapsulated $FACsPbI_3$ PSC a X-ray diffraction analysis was conducted on both the unprotected and the SnO_x protected PSC after exposure to a drop of water. A clear reflection associated with (PbI_2) occurs in the X-ray diffraction (Figure 6.2 c)) of the unprotected PSC layer, whilst reflections due to the perovskite have almost disappeared. On the contrary, for devices with an additional $20\,nm$ SnO_x layer no decomposition of the perovskite is observed.

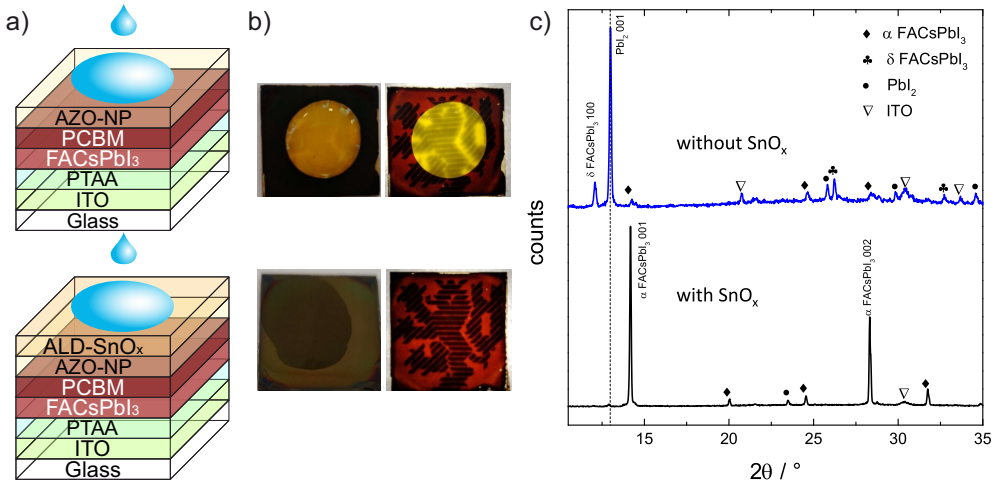

Figure 6.2: *Solar cell device stacks used to test the impact of water exposure a) without (top) and with (bottom) ALD-grown SnO_xlayer. b) Photographs of the respective samples with a drop of water dispensed on top (illuminated from top, left) and after drying (illuminated from the backside, right). Upon bottom illumination the seal of the University of Wuppertal (Lion) printed on the paper underneath the sample shines through. X-ray diffraction of the respective samples after water exposure. c) The graphs were vertically offset for clarity. Published in [97].*

Thus it can be concluded, that a $20\,nm$ layer of SnO_x is a suitable permeation barrier against the decomposing influence of a water based deposition process.

6.2 Comparison of Semitransparent Silver Nanowire Electrodes and ITO

For cost efficient upscaling and large area fabrication, liquid processed layers are highly preferred. In contrast to common deposition methods like sputtering and thermal evaporation, which require a high vacuum with pressures below $10^{-6}\,mbar$, solvent based layers can be deposited at atmospheric pressure. Furthermore, to achieve a sheet resistance around $10\,\Omega/sq$, an ITO layer thickness of i.e. $400\,nm$, sputtered at room temperature (without post annealing), is necessary. An ITO layer with that thickness shows a transmittance of $81\,\%$ in the spectral range of $350-1040\,nm$. These properties lead to a figure of merit of $1.0\times10^{-2}\,\Omega^{-1}$. In order to increase the figure of merit, the ITO sputtering process is typically followed by a high-temperature annealing step of $450\,°C$ as mentioned earlier [8–10]. An annealing step at temperatures in this range would lead to a thermal decomposition of the perovskite [138, 141].

As an alternative, a silver nanowire electrode was fabricated in air via spray coating from a $0.25\,mg\,mL^{-1}$ aqueous Ag-NW dispersion with an ultrasonic spray coater. The Ag-NWs had a diameter of 20 - 30 nm and comprised a PVP capping. The Ag-NW electrodes deposited on glass substrates show an average transmittance (T) of 87 % in the spectral range of $350nm - 1040\,nm$ with a R_{sh} of $12\,\Omega sq^{-1}$. The transmission and reflection spectra in comparison to that of ITO are shown in Figure 3.11. The FOM of the used Ag-NW electrode ($FOM_{NW} = 2.1 \times 10^{-2}\,\Omega^{-1}$) surpasses that of the ITO layer ($FOM_{ITO} = 1.0 \times 10^{-2}\,\Omega^{-1}$) by almost a factor of 2.

6.3 Ag-NW Based Electrodes for $FACsPbI_3$ Solar Cells

Encouraged by these promising results and the barrier properties of the SnO_x a semi-transparent Ag-NW-based electrode as described in chapter 2.2.2 was spray coated from aqueous a dispersion on top of the $FACsPbI_3$ stack with $20\,nm$ SnO_x protection barrier. The resulting semitransparent PSCs were illuminated with an AM1.5 solar spectrum and the J/V characteristics were obtained. The J/V characteristics of the PSC illuminated from the top side, shows a high fill factor of $> 75\,\%$ resulting in a reasonably high PCE of 13.4 %. Surprisingly the J/V characteristics illuminated from the bottom side of the device, differ notably from that under top illumination. The bottom side illumination leads to a strong s-shape in the J/V characteristics with a significant hysteresis. The devices show a fill factor of $< 40\,\%$ and a PCE of about 6 %. The full solar cell characteristics, including the opaque reference are summarized in Table 6.2.

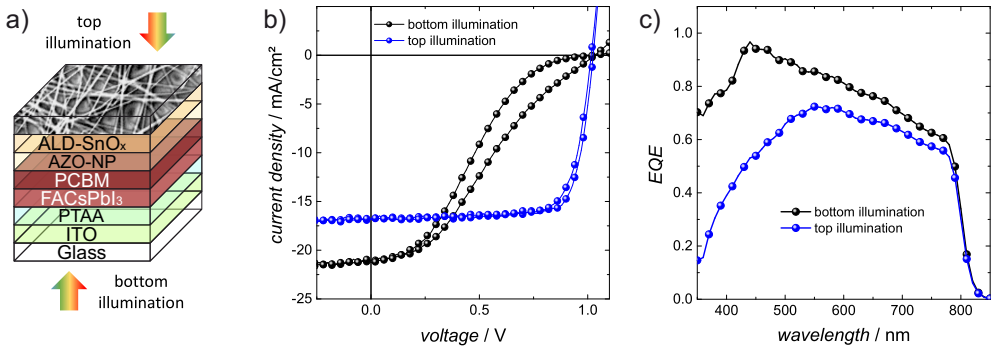

Figure 6.3: *a) Layer sequence of the PSC with a spray coated Ag-NW top electrode. b) J/V characteristics of solar cells with Ag-NW top electrode upon illumination form the bottom or top (Ag-NW) side. c) Corresponding EQE spectra. Published in [97].*

Table 6.2: *Cell characteristics of representative solar cells with Ag-NW top electrodes processed from water on solar cell stacks with an ALD SnO_x electron extraction layer and a reference cell with evaporated silver electrodes. J_{EQE} is the short circuit current density determined from the EQE data. Published in [97].*

		PCE [%]	**FF** [%]	$\mathbf{V_{OC}}$ [V]	$\mathbf{J_{SC}}$ [$\mathbf{mA/cm^2}$]
Ag-NW bottom illumination	rev.	6.4	30	1.03	21.1
	forw.	5.6	25	1.03	
Ag-NW top illumination	rev.	13.4	79	1.02	16.7
	forw.	12.7	75	1.02	
evaporated Ag opaque reference cell	rev.	18.4	75	1.06	23.0
	forw.	18.1	75	1.04	

As shown in Figure 6.3 c) the short current density of the top illuminated cell is on average $4.4\,mA\,cm^{-2}$ lower than under bottom illumination. To determine the origin of this lower current density an optical simulation was carried out. As shown in Figure 6.4 the contribution of the electron transport layer to this loss is $2.5\,mA\,cm^{-2}$. The Ag-NW top electrode causes $1.9\,mA\,cm^{-2}$ of this loss.

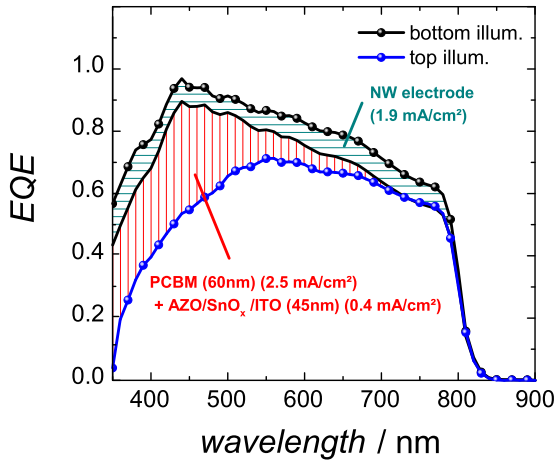

Figure 6.4: *Optical simulation of the loss of current in the PCBM/AZO/SnO_x/ITO ETL and the Nanowire electrode. Upon top illumination the light has to propagate through the nanowire electrode, the AZO/SnO_x/ITO and the PCBM layer. As simulated, the loss in current is $1.5\,mA/cm^2$ in the nanowire electrode, $0.4\,mA/cm^2$ in the AZO/SnO_x/ITO layer and $2.6\,mA/cm^2$ in the PCBM layer. These values add up to the real difference between top and bottom illumination. Published in [97].*

To further investigate the origin of the different cell characteristics depending on top/bottom illumination, a test structure was designed. Due to the fact, that no such behaviour was observed for solar cells with an opaque silver electrode, the interface of SnO_x and Ag-NW has been suspected as the origin of the s-shape. As shown in Figure 6.5 a), a layer structure without the active material of the perovskite was prepared to study the SnO_x/Ag-NW interface. The J/V characteristics of the test device show a clear rectifying behaviour for the SnO_x/nanowire interface while a device with an evaporated Ag electrode shows an ohmic behaviour. Under AM1.5 illumination, the rectifying behaviour vanishes and shows an almost linear (ohmic) characteristic, as can be seen in Figure 6.5.

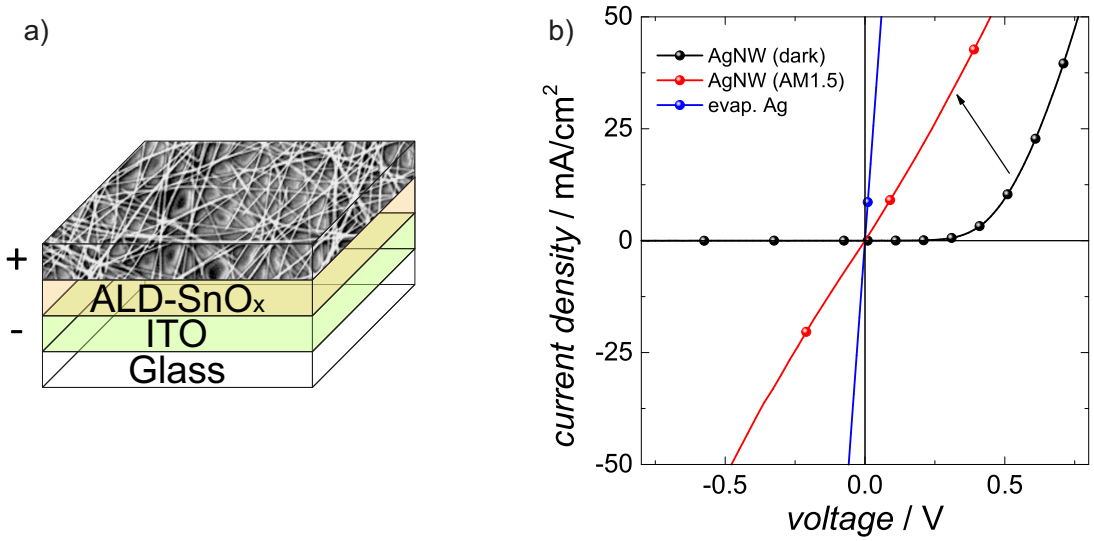

Figure 6.5: *a) Schematic illustration of the test stack used to investigate the SnO_x/Ag-NW interface. b) J/V characteristics of test devices in darkness and under AM1.5 illumination, compared to an evaporated silver electrode with and w/o PVP interlayer. Published in [97].*

In order to find an explanation of this diode-like behaviour for the Ag-NW electrode, it is essential to consider, that polyvinylpyrrolidone (PVP) is used as capping agent to disperse the Ag-NWs in liquids. It is reported, that PVP can lower the work function of oxide-based electrodes [142]. To verify this as explanation for the rectifying behaviour a thin intentional PVP coating of the SnO_x layer was casted via spin coating. This additional layer lowers the work function by $0.3\,eV$ (measured via Kelvin probe measurement). Consequently, test devices with an PVP interlayer and thermally evaporated Ag electrode (ITO/SnO_x/PVP/eAg) show no longer ohmic behaviour (Figure 6.6). These results can explain the formation of a rectifying contact between SnO_x and the PVP capped Ag-NWs.

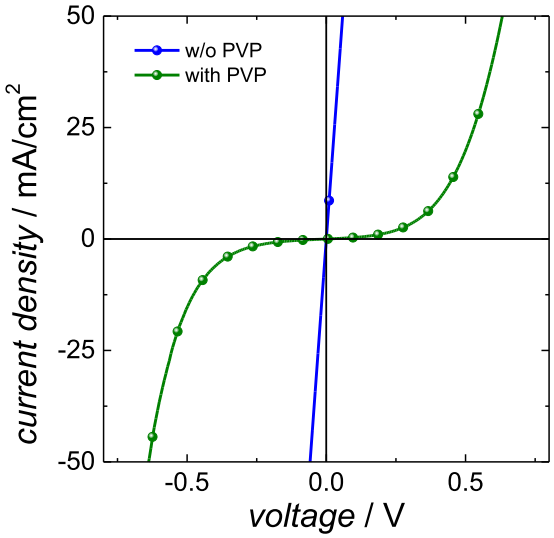

Figure 6.6: *J/V characteristics of test devices with an evaporated silver electrode with and w/o PVP interlayer. Published in [97].*

Furthermore, it can be observed, that the effect of illumination on the J/V characteristics of the test devices is reversible if illumination is switched off. As shown in Figure 6.7 the test devices return to their diode-like behaviour within 10 minutes of storage in darkness. Persistent photo-conductivity following illumination has been frequently observed for metal oxides [143–145]. This leads to the assumption, that the J/V behaviour is strongly dependent on the charge carrier density of the SnO_x adjacent to the Ag-NWs.

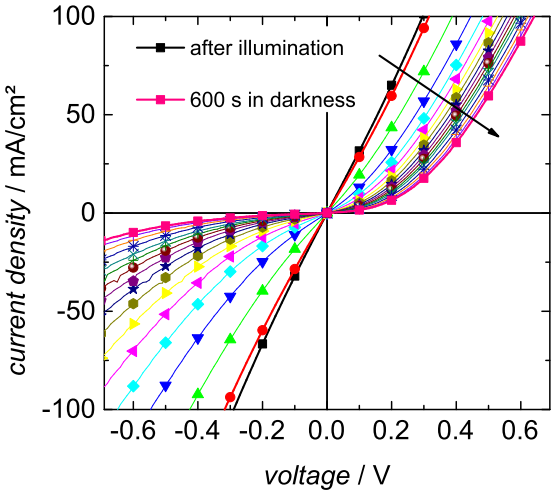

Figure 6.7: *J/V characteristics of a representative test device ITO/SnO_x/Ag-NW test devices kept in darkness after AM1.5 illumination. Published in [97].*

While the charge carrier density accumulated in the SnO_x due to illumination is hard to obtain, its possible to deliberately vary the charge carrier density in the SnO_x, to determine the influence of carrier density on the rectifying behaviour. It is well known, that the carrier density of ALD grown metal oxides is high on their growth conditions. By tuning these growth conditions (temperature, choice of oxidant, as shown in Table 6.3) we varied the carrier density of the SnO_x (all layers grown from TDMA-Sn) in the test devices deliberately in the range of $10^{16}\,cm^{-3}$ up to $10^{21}\,cm^{-3}$.

Table 6.3: *Carrier density in dependence of temperature and oxygen source for different ALD-grown SnO_x layer. Published in [97].*

T [C°]	**oxygen source**	**carrier density** $[cm^{-3}]$
80	H_2O	$<10^{16}$
100	H_2O	$\approx 10^{17}$
150	O_3	$\approx 10^{18}$
150	O_2-Plasma	$\approx 10^{19}$
200	O_3	$\approx 10^{21}$

As shown in Figure 6.8 a), the J/V characteristics are indeed highly dependent on the charge carrier density of the SnO_x layer [25]. For better visibility the rectifying ratio $(J(0.5\,V)/J(-0.5\,V))$ of the different test devices was calculated and shown in Figure 6.8 b). For a carrier density $10^{18}\,cm^{-3}$ or higher, the rectifying ratio of the J/V curve of the test devices becomes equal to 1, meaning an ohmic behaviour can be assumed.

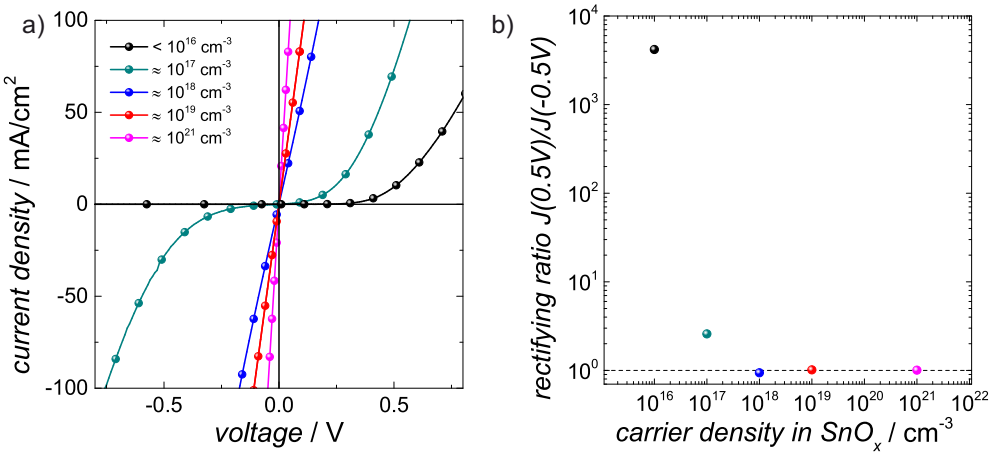

Figure 6.8: *a) J/V characteristics of Ag-NW test devices based on SnO_x with varied charge carrier density and b) the resulting rectification ratios J(0.5 V)/J(-0.5 V). Published in [97].*

The absence of an s-shape in the J/V curve of top illuminated PSCs is analogous to the situation found in the test structures, that turn ohmic upon illumination with AM1.5 simulated sunlight (Figure 6.5 b)) or by using a SnO_x layer with a high charge carrier density. The vanishing of the rectify behaviour under illumination can be explained either by the charge generation in the SnO_x via direct band-band absorption due to the illumination of the SnO_x/Ag-NW structure, or by the transfer of hot carriers from the Ag-NWs [146, 147].

To explain the strong dependence on the charge carrier density, the SnO_x/Ag-NW interface has to be considered as a metal-semiconductor junction. According to text-book semiconductor physics, in a rectifying metal-semiconductor interface, the width of the depletion region correlates with the Debye length. The Debye length (L_D) can be described with formula 6.1 (with ε being the Vacuum permittivity and for solids $\varepsilon_0 \cdot \varepsilon_r$).

$$L_D = \sqrt{\frac{\varepsilon \cdot U_T}{e \cdot n}}. \tag{6.1}$$

Thus L_D directly depends on the carrier density n in the semiconductor ($L_D \sim n^{-0,5}$). Consequently significantly lower Debye lengths for high charge carrier densities in the SnO_x are supposably the explanation for the strong dependence of the charge carrier density of the SnO_x on the J/V characteristics of the test devices.

As shown in Table 6.3 the carrier density in SnO_x is mostly dependent on the temperature and the used oxidant. Unfortunately, the growth conditions of SnO_x to achieve a carrier density $\geq 10^{18} cm^{-3}$ are not compatible with the deposition on top of the PSC, because they require highly corrosive precursors such as ozone or O-plasma and a growth temperature of $150\,°C$. Most perovskite solar cell architectures are unable to withstand these harsh conditions [138, 141].

While, as discussed previously, ITO also requires high temperature post processing to achieve the highly desired FOMs with high transparency and low sheet resistance, ITO deposited at room temperature still provides a charge carrier density of $10^{21} cm^{-3}$. Therefore, a $5\,nm$ ITO interlayer has been implemented to mitigate the formation of a barrier at the interface. Hereby, the ALD grown SnO_x provides efficient protection of the underlying PSC against the detrimental impact of the sputter process.
Comparing now the J/V characteristics of the PSC with a silver nanowire electrode and an ITO interface modification, the influence of the high charge carrier density interlayer

is obvious. A well-behaved ohmic contact, evidenced by high fill factors in excess of 77 % as well as PCEs up to 17.4 % upon illumination from the bottom (substrate), is achieved (see Figure 6.9).

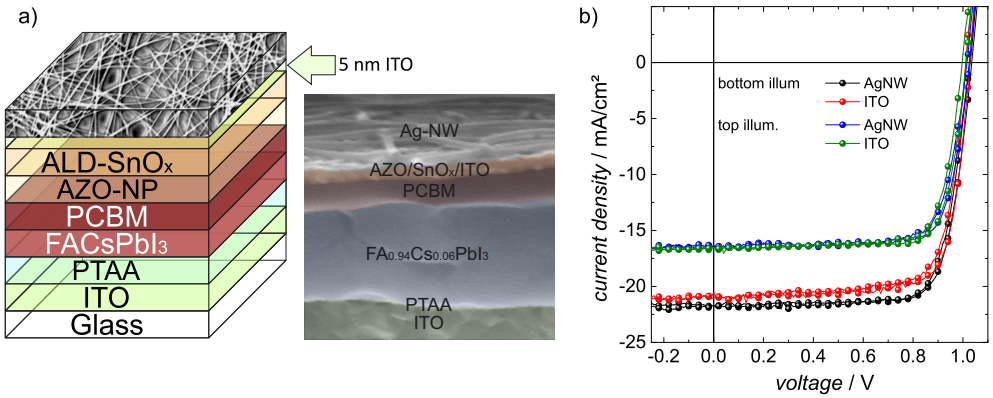

Figure 6.9: *a) Layer sequence and SEM cross section image b) J/V characteristics of the PSC with a spray coated Ag-NW top electrode and a thin ITO interlayer. Published in [97].*

Compared to PSCs with a 400 nm thick sputtered ITO top electrode, the devices based on Ag-NWs show similar or even superior characteristics under bottom illumination. Opposed to that, the J_{sc} under top illumination is somewhat higher for the cells based on thick ITO compared to the Ag-NW devices, even though the reflectance of the Ag-NW is slightly lower than of ITO (see Table 6.4).

To compare the potential J_{sc} of a PSC with either an ITO or Ag-NW electrode, an optical simulation of a full device stack has been carried out. As discussed previously, in order to achieve the same R_{sh} of 12 Ω/sq as the Ag-NW electrode, the room temperature processed ITO electrode needs to be 400 nm thick. As shown in Figure 6.10, the difference in J_{sc} for a PSC with a 400 nm ITO electrode compared with a Ag-NW electrode with a comparable sheet resistance is expected.

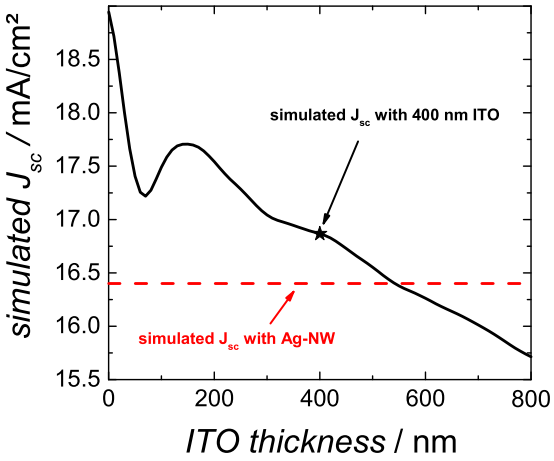

Figure 6.10: *Optical simulation of the loss of current in the PCBM/AZO/SnO_x/ITO ETL and the nanowire electrode for top side illumination. Published in [97].*

The full EQE characteristics for both devices as well as the transmittance of the full device stacks and the stabilized power output for operation at the maximum power point are illustrated in Figure 6.11. From the transmittance spectra we can determine the average transmittance of the PSC with $5\,nm$ ITO interlayer and Ag-NW electrode of 16 % in the region of $550 - 820\,nm$ and 68 % in the near infrared ($> 820\,nm$).

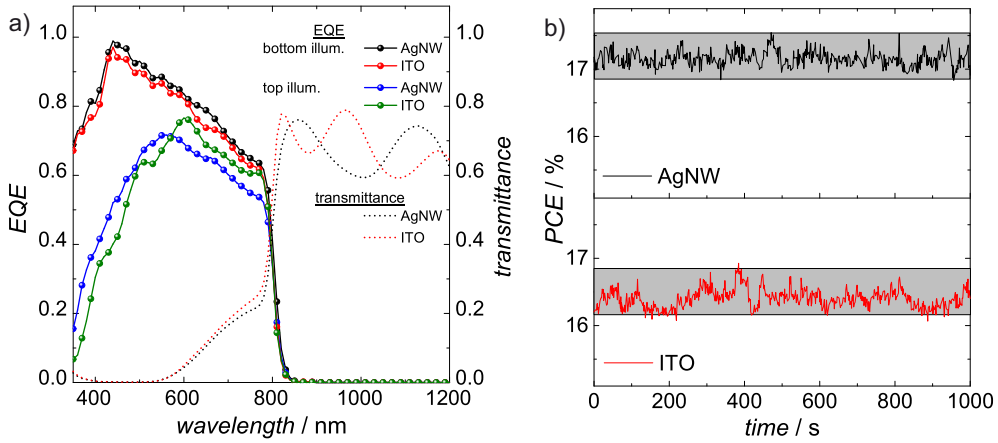

Figure 6.11: *a) EQE data, transmittance spectra and b) stabilized power output of semitransparent perovskite solar cells. Published in [97].*

Ultimately, ITO layers sputtered this thick happen to come with significant internal stress [148]. This stress occasionally leads to the formation of wrinkles or cracks and eventually to delamination. Figure 6.12 shows this devastating consequence of the internal stress on the PSC.

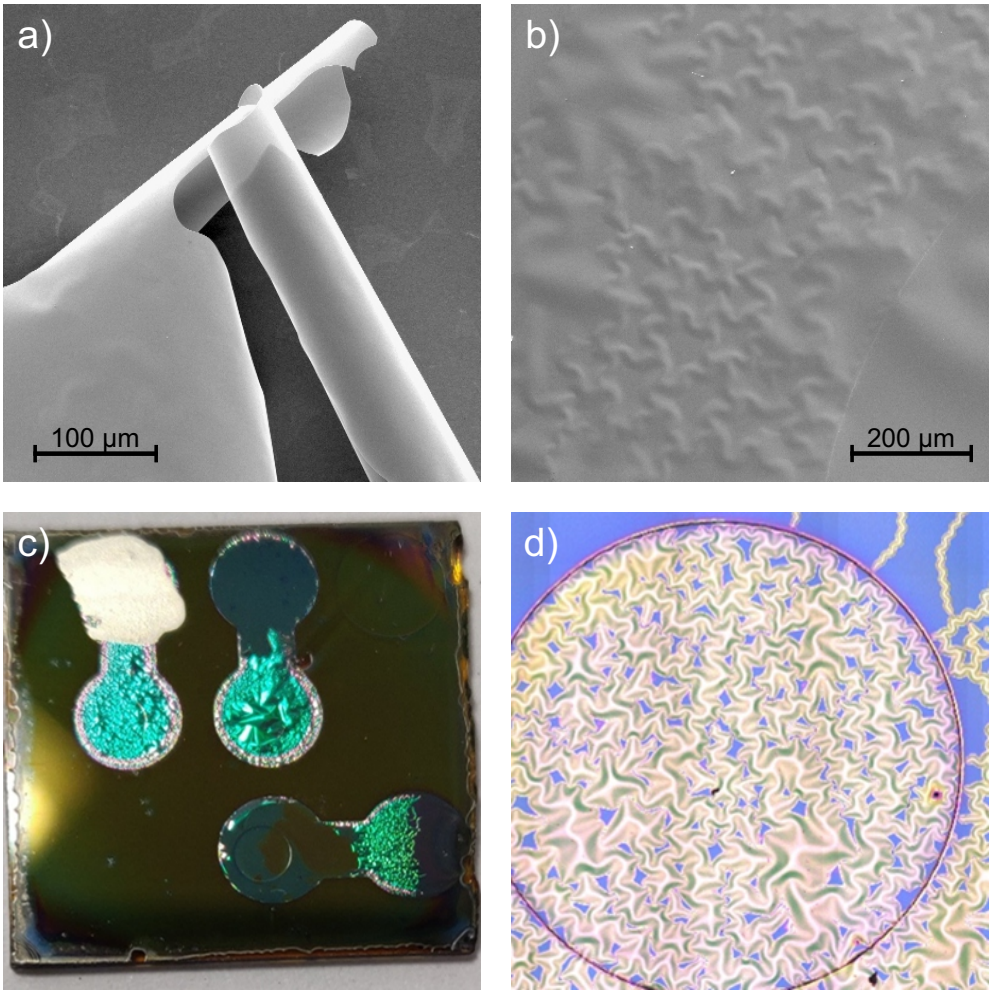

Figure 6.12: *Pictures of the wrinkling and delaminating ITO electrode a) SEM image of the delaminating ITO electrode. b) SEM image of the wrinkling ITO electrode. c) Image of the PSC substrate with delaminating ITO electrode. d) Microscopy image of the PSC with wrinkling ITO electrode. Published in [97].*

In contrast to that, the Ag-NW electrodes not only reduce the use of indium but also obviate the mechanical issues inferred by thick metal oxide layers. This preparation of the Ag-NW electrode from an environmentally friendly aqueous dispersion on top of the PSC was enabled by the impermeability of the ALD grown SnO_x ETL. To verify that the aqueous processing has no negative, delayed influence (e.g. remanescent water slowly penetrating through the SnOx) on the PSC at all, the PSC was measured before and after $1500\,h$ storage in nitrogen. As shown in Figure 6.13 a) the device characteristics remain unchanged. Therefore it can be concluded that the water-based deposition process of the Ag-NW electrode does not compromise the intrinsic device stability.

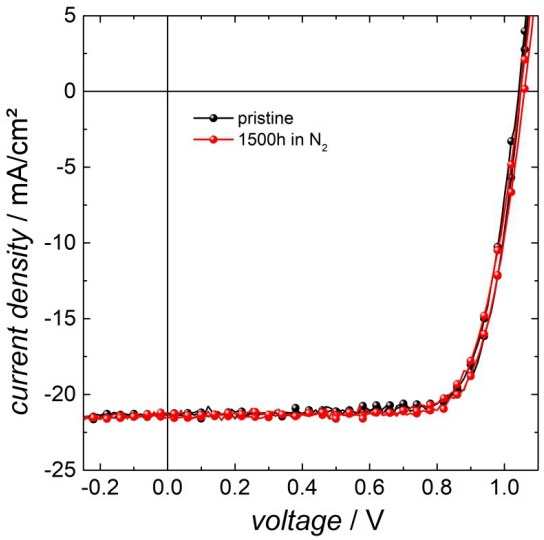

Figure 6.13: *Representative J/V characteristics of a PSC with water processed Ag-NW electrode pristine and after storage in N2 for 1500h. Published in [97].*

Table 6.4: *Characteristics of solar cells with 5 nm ITO + Ag-NWs (labelled "Ag-NW") top electrode compared with PSCs with 400 nm thick sputtered ITO top electrode (labelled "ITO"). Champion cells are presented in brackets. Statistics were acquired from 12 cells each, except EQE data of PSCs with thick ITO electrodes, where only four cells were measured.* J_{EQE} *is the short circuit current density determined from the EQE data. Published in [97]*

	Top Electrode	**PCE** [%]	**FF** [%]	$\mathbf{V_{OC}}$ [V]	$\mathbf{J_{SC}}$ [$\mathbf{mA/cm^2}$]
Bottom illum.	Ag-NW rev.	16.8 ± 0.5 (17.4)	75 ± 2 (77)	1.04 ± 0.01 (1.04)	21.4 ± 0.4 (21.9)
	Ag-NW forw.	16.5 ± 0.5 (17.2)	74 ± 1 (76)	1.04 ± 1.02 (1.03)	
	ITO rev.	16.4 ± 0.4 (16.8)	75 ± 1 (76)	1.03 ± 0.02 (1.05)	21.2 ± 0.1 (21.3)
	ITO forw.	15.9 ± 0.4 (16.3)	74 ± 1 (75)	1.01 ± 0.02 (1.01)	
Top illum.	Ag-NW rev.	13.0 ± 0.3 (13.4)	77 ± 1 (78)	1.02 ± 0.01 (1.03)	16.4 ± 0.3 (16.6)
	Ag-NW forw.	12.6 ± 0.4 (13.1)	76 ± 1 (79)	1.01 ± 0.01 (1.03)	
	ITO rev.	13.3 ± 0.4 (13.6)	77 ± 1 (78)	1.01 ± 0.02 (1.03)	16.8 ± 0.2 (16.8)
	ITO forw.	12.6 ± 0.5 (12.8)	75 ± 2 (75)	0.99 ± 0.02 (1.01)	

6.4 Conclusion

In summary, it can be concluded that an impermeable electron transport layer based on SnO_x allows the spray coating deposition of semitransparent Ag-NW electrodes from aqueous dispersions on top of perovskite solar cells without causing any damage to the notoriously moisture sensitive photo-active material. Specifically, the impermeable ETL consists of a bilayer of AZO-NPs and a dense SnO_x layer grown by low temperature ALD, which provides efficient protection for the perovskite against water. The formation of an electronic barrier at the interface of the SnO_x and the Ag-NW, which initially caused s-shaped J/V characteristics has been pinpointed to a shift in work function between the SnO_x and the Ag-NW due to the PVP capping agent of the Ag-NW. This barrier has been successfully mitigated by an elevated carrier density in the SnO_x higher than $10^{18} cm^{-3}$. Alternatively, a $5\,nm$ thin interfacial layer of ITO with a carrier density of $10^{21} cm^{-3}$ has been applied between the SnO_x and the Ag-NW to achieve well behaved device characteristics. This work demonstrates a general strategy, where impermeable charge transport layers in the PSC stack unlock novel processing options.

7

ALD-Grown Indium Oxide as Semitransparent Conductive Gas Diffusion Barrier

As elaborated in the previous chapter, ALD-permeation barriers can prevent the degradation of perovskite solar cells due to environmental influences and even further from the devastating influence of water based processes on top of the fragile perovskite. Though common gas diffusion barriers like Al_2O_3 or nanolaminates of TiO_2 and Al_2O_3 [149] provide excellent barrier properties with a water vapor transmission rate up to $10^{-6} gm^{-2} day^{-1}$ at $70\,°C/70\,\%rh$ [149, 150], these metal oxides are insulators. Therefore they are not suitable as functional charge transport layers in solar cells. While ALD-grown SnO_x layers are already used for such a purpose in solar cells their electrical conductivity excludes them as electrode material [150]. Opposed to that, indium oxide (InO_x) has been reported to show high charge carrier densities and low sheet resistances [31] and is therefore a potential candidate for the use as an ALD-grown protection layer which is used as an electrode at the same time. In this section the potential of ALD-grown indium oxide for perovskite solar cells is presented as a starting point for future improvements. All ALD-processes in this chapter were performed at $80\,°C$.

As reported in the literature it is possible to grow InO_x by ALD using Cyclopentadienylindium(I) (CpIn) as precursor at low temperatures with high charge carrier densities around $10^{20}\,cm^{-3}$ [31]. In these processes it was found, that a thin Al_2O_3 seed layer is necessary to facilitate nucleation and to afford a homogeneous layer. Since Al_2O_3 is a dielectric material it is not preferred to use Al_2O_3 as interlayer in a solar cell, which is why in this work the use of SnO_x as seed layer is explored. At first the growth of InO_x on a reference stack using AZO-nanoparticles (see Figure 7.1 a), and a varying thickness of SnO_x was used to verify the ALD-growth of 240 cycles InO_x on the seed layer. Hereby the number of ALD-cycles to grown SnO_x from TDMA-Sn and H_2O were varied between 17 cycles ($3\,nm$) up to 16 cycles ($20\,nm$). As shown in Figure 7.1 b) a minimum of 40 cycles ($5\,nm$) is needed to ensure a steady growth of InO_x. Layer thicknesses were measured via ellipsometry. Without any SnO_x seed layer, no growth of InO_x could be measured.

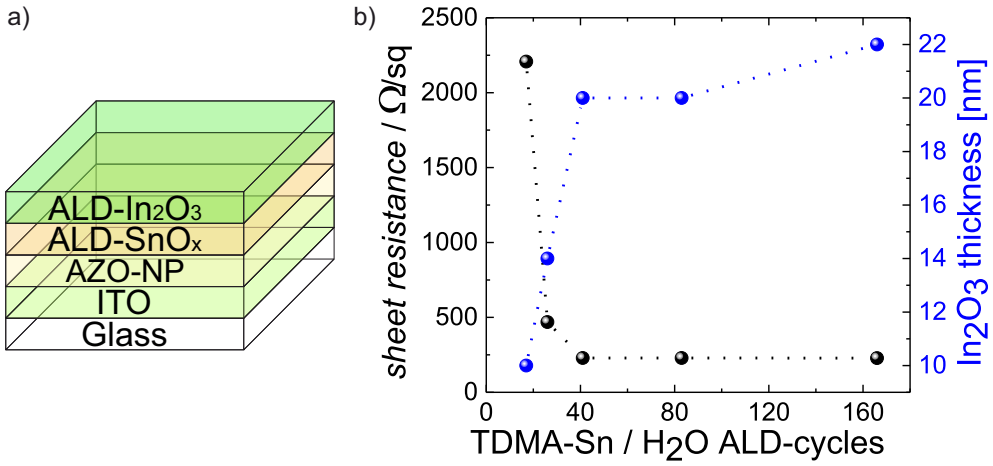

Figure 7.1: *a) Layer sequence b) Thickness and sheet resistance of a layer grown from 240 cycles of CpIn and H_2O/O_2 on SnO_x. Supervised master thesis [151]*

As pictured in Figure 7.1 b) 240 cycles of InO_x provide layers with a thickness of around $20\,nm$. To further investigate the properties of the grown layers either 20 and $100\,nm$ were grown and their properties were characterized. As shown in Table 7.1 the electrical properties, like charge carrier density and work function are not changing with thickness.

Table 7.1: *Properties of ALD-grown InO_x at 240 and 1200 cycles on an ITO substrate with an AZO-nanoparticle/ALD-SnO_x seed layer.*

CpIn/H_2O/O_2 - cycles	R_{sh} [Ω/**sq**]	**carrier density** [cm^{-3}]	**thickness** [**nm**]	**work function** [**eV**]
240	240	10^{20}	20	4.6 ± 0.1
1200	40	10^{20}	100	4.6 ± 0.1

To characterize the optical properties of the ALD InO_x 100 nm thick layers were deposited on a 2 nm Al_2O_3 seed layer on quartz-glass. The resulting spectra for reflectance, transmittance and absorbance are shown in Figure 7.2.

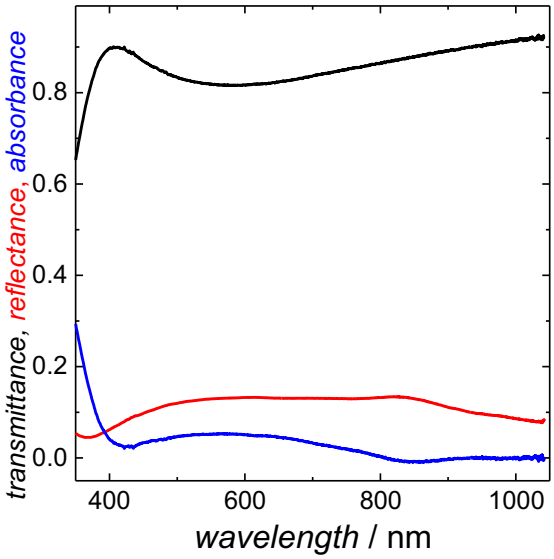

Figure 7.2: *Reflectance, transmittance and absorbance spectra of a 100 nm InO_x layer on quartz-glass. Layer thicknesses were measured via ellipsometry.*

These high transmittance, paired with the low sheet resistance and high charge carrier density identify the InO_x as an interesting candidate for a transparent electrode, which could potentially act as a gas diffusion barrier itself without the need of an additional functional layer.

To compare the barrier properties of the 100 nm InO_x layer with a 100 nm SnO_x layer as used in [26] an optical calcium test has been carried out as reported in the literature [152].

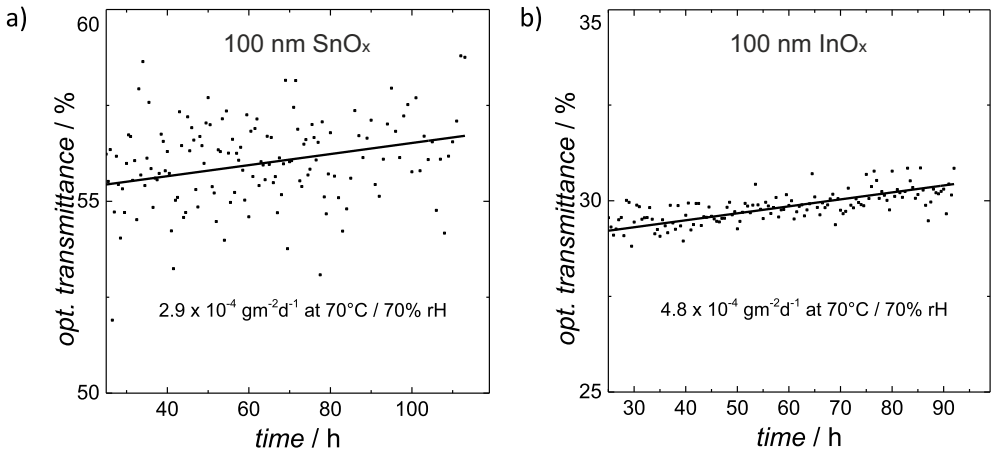

Figure 7.3: *Change of optical transmittance of the calcium pads, encapsulated with a) 100 nm SnO_x and b) 100 nm InO_x. The slope of the linear fit yields the water vapor transmission rate.*

As shown in Figure 7.3, the barrier properties of 80 $°C$ grown InO_x and SnO_x are within the same order of magnitude. Therefore ALD grown InO_x is a potential candidate for the use as semitransparent electrode in perovskite solar cells. Figure 7.4 shows a comparison of the InO_x electrode compared to the Ag-NW and ITO electrodes also shown in this work. As pictured clearly, the figure of merit is substantially lower, than that of ITO, mostly due to the sheet resistance that is higher by a factor of three. However, the barrier properties lets the InO_x electrode stand out to the other electrodes, and brings benefits that can compensate the lower figure of merit.

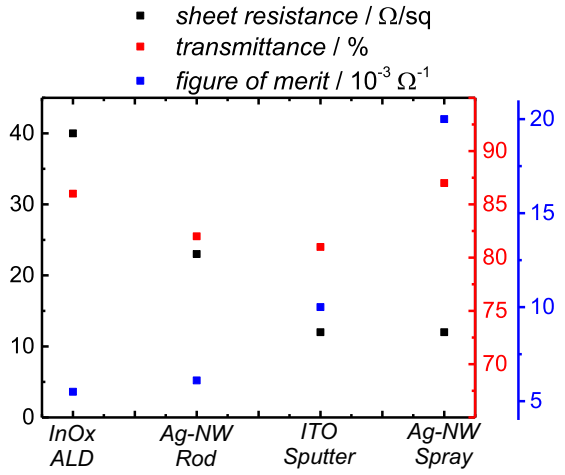

Figure 7.4: *Sheet resistance, transmittance and figure of merit of electrodes, shown in this work.*

To verify the use in perovskite solar cells as transparent electrode, standard PSCs using $MAPbI_3$ [100] as active material are used. Figure 7.5 compares the J/V-characteristics of a solar cell using InO_x as an electrode to an opaque reference using thermally evaporated silver as an electrode.

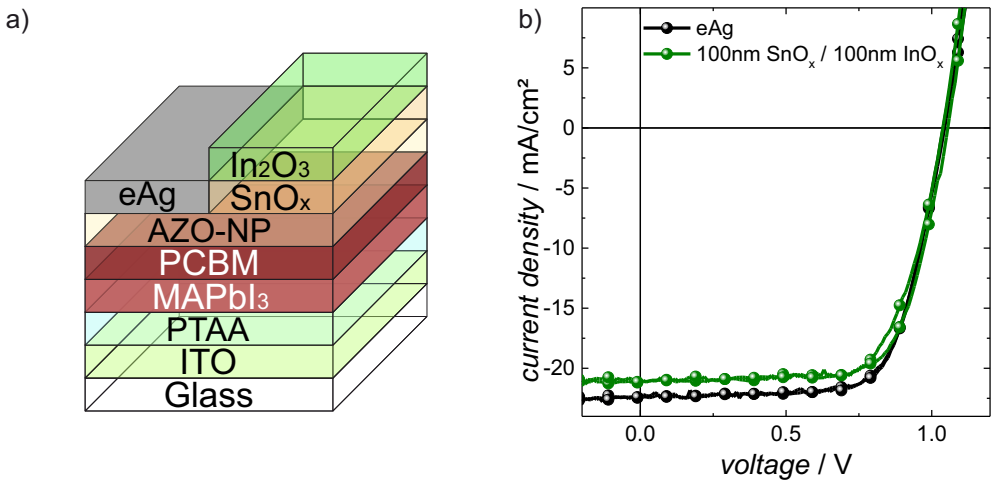

Figure 7.5: *a) Layer sequence b) J/V characteristics of $MAPbI_3$ perovskite solar cells using evaporated silver or ALD-layer as electrode.*

Table 7.2: *Cell characteristics of representative solar cells with Ag-NW top electrodes processed from water on solar cell stacks with an ALD SnO_x electron extraction layer and a reference cell with evaporated silver electrodes measured from the bottom side.*

		PCE [%]	**FF** [%]	$\mathbf{V_{OC}}$ [V]	$\mathbf{J_{SC}}$ [$\mathbf{mA/cm^2}$]
AZO-NP/eAg	rev.	16.5	71	1.04	22.4
	forw.	16.4	70	1.04	22.5
AZO-NP/SnO_x/InO_x	rev.	15.7	71	1.05	21.1
	forw.	15.3	70	1.04	21

As displayed in Figure 7.5 b) and Table 7.2 the characteristics of a PSC using opaque silver tend to be similar to the ones with an InO_x electrode, except the current which is naturally lower in semitransparent devices (see Section 5 and 6).

Conclusion and Future Prospects

As shown in this chapter ALD-grown InO_x shows excellent barrier properties against humidity. Furthermore their electric and optical properties are promising for the use in opto-electronic devices. The use as interface modification as shown in chapter 6 is possible. Ultimately it is possible to use InO_x as semitransparent conductive gas diffusion barrier as shown in this chapter. As long term stability studies were beyond the scope of this work, it remains to be clarified to what extent the barrier properties of the InO_x electrode afford an improved long term stability of the perovskite cells.

8

Conclusion

In this work, semitransparent electrodes based on silver nanowires were successfully implemented in multiple opto-electronic devices. Hereby it was possible to show the flexibility in processing ranging from meyer rod coating (as a laboratory replacement for slot dye coating) to ultrasonic spray coating which are both suitable for industrial fabrication. Moreover, the use case for electroluminescent devices was elaborated in depth. The notable advantages of Ag-NWs as semi-transparent electrode material compared to established PEDOT:PSS electrodes was demonstrated in regard to brightness and homogeneity, especially for larger area devices. By using Ag-NWs electrodes it was possible to transfer the device architecture into a bifacially emitting and overall translucent device. This bifacial device was used as a platform to place a second electroluminescent device on top to realize a bifacial, color-tunable electroluminescent device. The main feature of this device is the possibility to operate two emission zones individually and therefore achieve a mix of both colors, whose ratio can be changed according to the application. By the use of orange and blue emission zones it is possible to perform a color transition from orange to blue while receiving a bright white emission with the right ratio.

In the field of solar cells, a fully liquid processed layer sequence for semitransparent organic solar cells, which is suitable for large area industrial roll to roll processing, was presented.
For semitransparent perovskite solar cells, the deposition of a semitransparent Ag-NW top electrode from an aqueous dispersion, was enabled by using an ALD SnO_x protection barrier. Thereby, it was possible to achieve semitransparent perovskite solar cells with high efficiencies of over 16 % with an overall transmittance of 68 % in the near infrared ($> 820\,nm$), once again by using a roll-to-roll suitable semitransparent silver nanowire electrode. This enables the usage in tandem solar cell architectures e.g. on top of a narrow band gap bottom cell.
As a starting point for future work, semitransparent electrodes based on ALD-grown InO_x were demonstrated. Their electrical and optical properties are promising in regards to the use as semitransparent electrode, acting as gas permeation barrier at the same time.

Future prospects

Based on this work several subsequent studies are facilitated. For alternating current electroluminescent devices the usage of silver nanowires as an electrode has increased luminance and homogeneity significantly. The results in this work suggest, that by using dielectric materials with a high transmittance, the overall luminance can be increased noticeably. The transition to more efficient emitting materials can further increase the field of applications for alternating current electroluminescent devices especially the possibility of color tunability by adding a second layer with different colors and the related color tunability.
Furthermore the results in semitransparent thin film solar cells offer new fields of applications towards device integration for architecture. Large area, semitransparent solar cells could be integrated in skyscrapers or other urban buildings to enable energy harvesting in common and everyday objects without additional space used. Especially with the huge progress in regards to efficiency, the results presented in this work can make a huge contribution for urban energy harvesting.
The use of InO_x for perovskite solar cells, which was touched upon briefly, has to be investigated in the future. Especially the use of InO_x as functional interlayer or as highly conductive barrier is of interest, as no such use is reported until now.

Notation: The author gratefully acknowledges the financial support by the Federal Ministry for Education and Research BMBF (Grant No. 03EK3529E), The Deutsche Forschungsgemeinschaft DFG (Grant Nos. RI1551/4-3 and RI 1551/12-1) and the Zentrales Innovationsprogramm Mittelstand ZIM (Grand Nos. ZF4037801CK5 and ZF4037809DF8) In addition to that the author wants to thank the BASF SE for providing the silver nanowire dispersions, and InovisCoat GmbH for the help and expertise in regards to electroluminescent devices and materials

A

Appendix

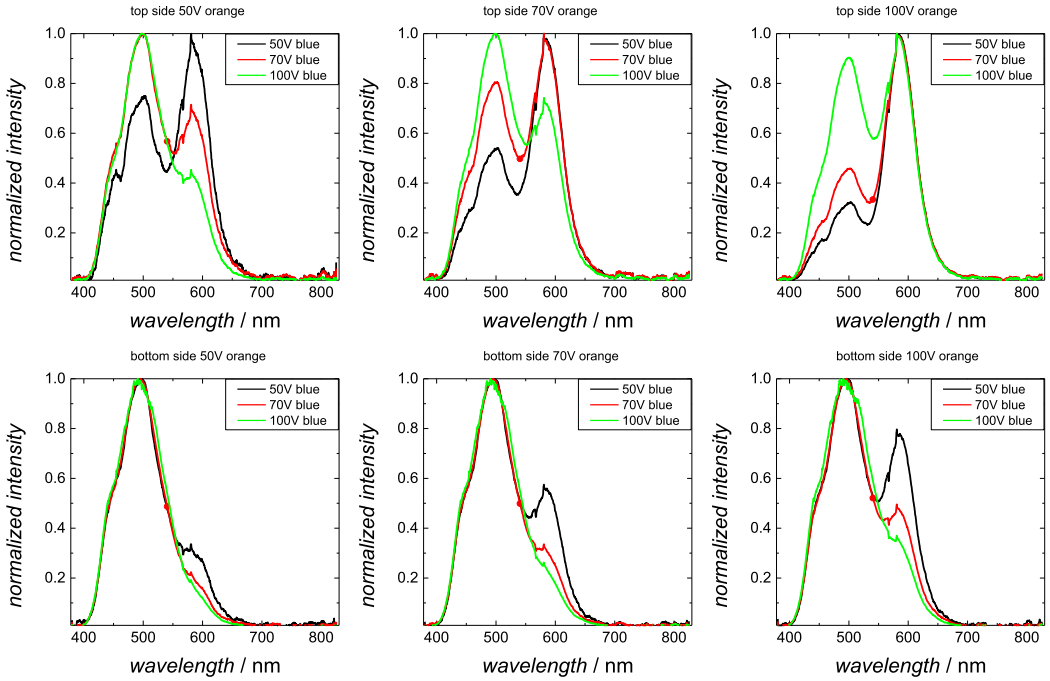

Figure A.1: *Emission spectra of all operation modes of the multicolor tandem ACEI device. Published in [104].*

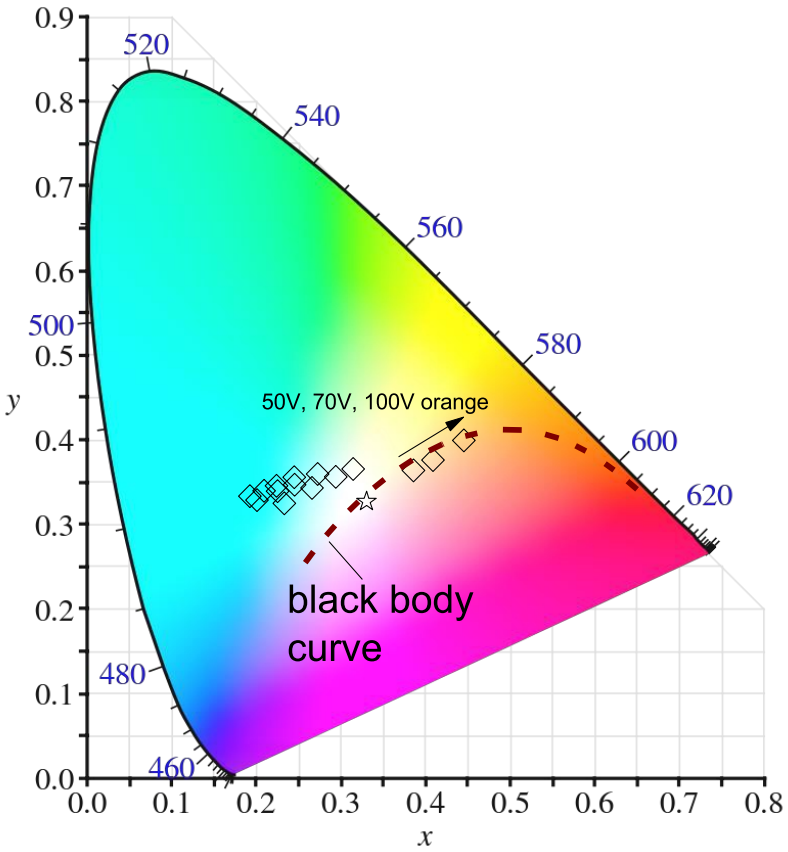

Figure A.2: *CIE diagram of the tandem ACEL device measured from the blue side of the device. Published in [104].*

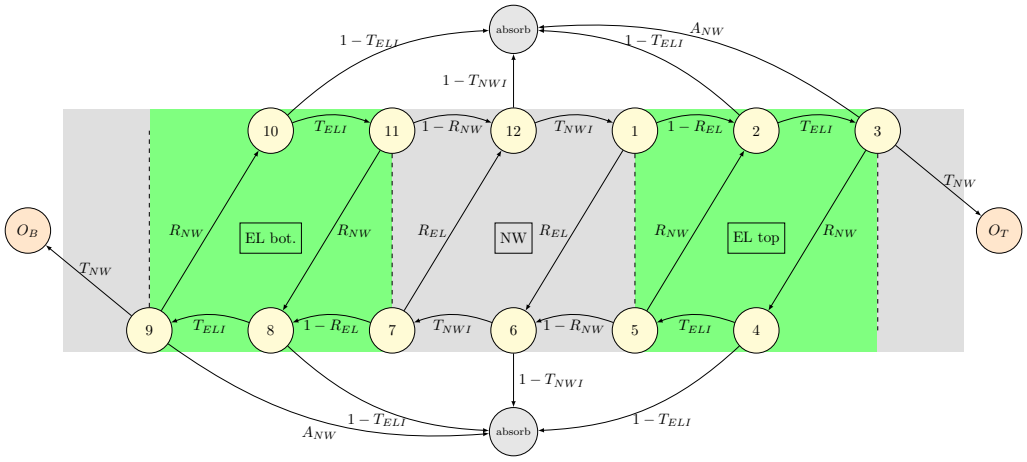

Figure A.3: *Schematic drawing of the modelation for the transfer Matrix. Published in [104].*

Transfer matrix model to calculate the loss of luminance in the non-operated EL sub device. The device structure has been simplified by combining the dielectric and the luminescent layer in one layer (denoted EL). Various nodes has been introduced (displayed as yellow circles, numbered 1-12). The nodes positioned at the interface represent the reflection at the interface, while the nodes in the center of a layer represent the absorption in the layer. The nodes (1-3; 10-12) in the upper half of the scheme represent the direction of light propagating from the left to the right. The other nodes (4-9) display the direction of light from the right to the left. The node labelled with 1 represents the light emitted from the bottom sub device that has passed the center Ag-NW electrode and now hits the Ag-NW/EL interface of the top sub-device, were the light is either reflected (with a propability of R_{EL}) or is able to propagate into the EL-layer with a probability of $1 - R_{EL}$. From there on the photons gets either transmitted (T_{ELI}) or absorbed ($1 - T_{ELI}$), and so on. The orange circles O_T and O_B on the right and left side represents the light coupled out to the top and the bottom electrode of the device. The grey circles, labelled "absorb", represent all the absorbed portion of light in the device.

$$M = \begin{pmatrix}
0 & 0 & 0 & 0 & 0 & 0 & 0 & 0 & 0 & 0 & 0 & T_{NWI} & 0 & 0 & 0 \\
1-R_{EL} & 0 & 0 & 0 & R_{NW} & 0 & 0 & 0 & 0 & 0 & 0 & 0 & 0 & 0 & 0 \\
0 & T_{ELI} & 0 & 0 & 0 & 0 & 0 & 0 & 0 & 0 & 0 & 0 & 0 & 0 & 0 \\
0 & 0 & R_{NW} & 0 & 0 & 0 & 0 & 0 & 0 & 0 & 0 & 0 & 0 & 0 & 0 \\
0 & 0 & 0 & T_{ELI} & 0 & 0 & 0 & 0 & 0 & 0 & 0 & 0 & 0 & 0 & 0 \\
R_{EL} & 0 & 0 & 0 & 1-R_{NW} & 0 & 0 & 0 & 0 & 0 & 0 & 0 & 0 & 0 & 0 \\
0 & 0 & 0 & 0 & 0 & T_{NWI} & 0 & 0 & 0 & 0 & 0 & 0 & 0 & 0 & 0 \\
0 & 0 & 0 & 0 & 0 & 0 & 1-R_{EL} & 0 & 0 & 0 & R_{NW} & 0 & 0 & 0 & 0 \\
0 & 0 & 0 & 0 & 0 & 0 & 0 & T_{ELI} & 0 & 0 & 0 & 0 & 0 & 0 & 0 \\
0 & 0 & 0 & 0 & 0 & 0 & 0 & 0 & R_{NW} & 0 & 0 & 0 & 0 & 0 & 0 \\
0 & 0 & 0 & 0 & 0 & 0 & 0 & 0 & 0 & T_{ELI} & 0 & 0 & 0 & 0 & 0 \\
0 & 0 & 0 & 0 & 0 & 0 & R_{EL} & 0 & 0 & 0 & 1-R_{NW} & 0 & 0 & 0 & 0 \\
0 & 1-T_{ELI} & A_{NW} & 1-T_{ELI} & 0 & 1-T_{NWI} & 0 & 1-T_{ELI} & A_{NW} & 1-T_{ELI} & 0 & 1-T_{NWI} & 1 & 0 & 0 \\
0 & 0 & 0 & 0 & 0 & 0 & 0 & 0 & T_{NW} & 0 & 0 & 0 & 0 & 1 & 0 \\
0 & 0 & T_{NW} & 0 & 0 & 0 & 0 & 0 & 0 & 0 & 0 & 0 & 0 & 0 & 1
\end{pmatrix}$$

Figure A.4: *Resulting transfer matrix for the schematic in Figure A.3. Published in [104].*

Resulting transfer matrix for the schematics in Figure S4. The "internal" transmission factors T_{ELI} and T_{NWI} has been calculated by using the measured transmission, factoring out the reflectance since the reflection and transmission in this model is split in different steps. The following equations show the calculation of the "internal transmission factors":

$$T_{EL} = 0.43, T_{NW} = 0.75, R_{NW} = 0.25.$$

$$T_{ELI} = \frac{T_{EL}}{1 - R_{EL}} = \frac{0.43}{1 - R_{EL}}.$$

$$T_{NWI} = \frac{T_{NW}}{1 - R_{NW}} = \frac{0.43}{1 - 0.2} = 0.8.$$

Each column represents a node and the propagation to the node represented by the row. For example the transfer from node 1 is represented by column 1. In the scheme figure A.3 it is shown that with a probability of R_{EL} light is reflected to node 6 (compare the matrix point column 1 row 6) or propagates with a probability of 1-REL to node 2 (Column 1 row 2). The rest follows accordingly. The matrix highlighted in red is the resulting matrix for the propagation and reflections between the nodes 1 - 12 in the scheme shown in Figure S4. The columns 13, 14, 15 highlighted in orange show the transfer from the internal reflections and transmissions to the final nodes (absorption, or emission to either side). Row 13 expresses the transfer of the nodes 1 - 12 to the absorption node, row 14 to the left side (representing the bottom side of the device) and row 15 to the right side (top side of the device). The identity matrix highlighted in green express the 3 final states for a photon. Row/column 13 represents the "absorb" node, Row/column 14 represents the emission from the bottom side of the device, row/column 15 the emission trough the top device. Taking the n-th power of the matrix M, i.e. M^n (where n is the number of steps the photon took inside of the device), with nß∞ results in a matrix where the first column shows the probability of a photon being at a certain position in the device after n steps in the device. The values at the rows 13, 14 and 15 represent the absorption, emission to the bottom side and emission to the top side. Note, the calculation converges for n = 20. We calculated the M^{20} matrix, using all known variables with R_{EL} as only unknown. From the comparison of the luminance from top side of the single bi-facial EL device and the luminance of the bottom device measured through the top electrode of the tandem device, a ratio of about 46 % can be determined. Therefore the value in column 1 row 15 of the M^{20} matrix (M^{20}(15,1)) has to be 0.46 (46 %). Solving the equation M^{20} (15,1)=0.46 for REL with GNU Octave results in 1 solution in the amount of solutions $[0; 1]$ for $R_{EL} = 0.52$ (52 %). In addition to the already known overall emission to the top side of 46 %, it is now possible to calculate the theoretical emission to the bot side of 24 % and the absorption in the device of 30 %. The Mathematical calculations were carried out with GNU Octave.

Publications

1. T. Gahlmann, T. Tschorn, T. Maschwitz, L. Gomell, T. Haeger, G. Grötsch, R. Heiderhoff, and T. Riedl: Bi-facial Color-Tunable Electroluminescent Devices *ACS Appl. Mater. Interfaces, 13, 24, 28514-28520 (2021)*

2. T. Gahlmann, K. O. Brinkmann, T. Becker, C. Tückmantel, C. Kreusel, F. van gen Hassend, S. Weber, and T. Riedl: Impermeable charge transport layers enable aqueous processing on top of perovskite solar cells *Adv. Energy Mater. 10, 1903897 (2020)*

3. K. O. Brinkmann, T. Gahlmann, and T. Riedl: Atomic Layer Deposition of Functional Layers in Planar Perovskite Solar Cells *Solar RRL 4, 1900332 (2020)*

4. T. Keller, T. Gahlmann, U. Scherf, and T. Riedl: Direct Arylation Polycondensation (DAP) Synthesis of Alternating Quaterthiophene-Benzothiadiazole Copolymers for Organic Solar Cell Applications *ChemPlusChem 34, 1249 (2019)*

5. Y. Forov, M. Paulus, S. Dogan, P. Salmen, C. Weis, T. Gahlmann, A. Behrendt, C. Albers, M. Elbers, W. Schnettger, S. Egger, E. Zwar, H. Rehage, I. Kiesel, T. Riedl, and M. Tolan: The adsorption behavior of lysozyme at titanium oxide-water interfaces *Langmuir 34, 5403 (2018)*

6. T. Hu, T. Becker, N. Pourdavoud, J. Zhao, K. Brinkmann, R. Heiderhoff, T. Gahlmann, Z. Huang, S. Olthof, K. Meerholz, D. Többens, B. Cheng, Y. Chen, and T. Riedl: Indium-Free Perovskite Solar Cells Enabled by Impermeable Tin-Oxide Electron Extraction Layers *Adv. Mater. 29, 1606656 (2017)*

7. J. Zhao, K. Brinkmann, T. Hu, N. Pourdavoud, T. Becker, T. Gahlmann, R. Heiderhoff, A. Polywka, P. Görrn, Y. Chen, B. Cheng, and T. Riedl: Self-Encapsulating Thermostable and Air-Resilient Semitransparent Perovskite Solar Cells *Adv. Energy Mater. 7, 1602599 (2017)*

8. K. Brinkmann, J. Zhao, N. Pourdavoud, T. Becker, T. Hu, S. Olthof, K. Meerholz, L. Hoffmann, T. Gahlmann, R. Heiderhoff, M. F. Oszajca, N. A. Luechinger, D. Rogalla, Y. Chen, B. Cheng, and T. Riedl: Suppressed decomposition of organo-metal halide perovskites by impermeable electron extraction layers in inverted solar cells *Nature Communications 7, 13938 (2017)*

9. A. Behrendt, J. Meyer, P. van de Weijer, T. Gahlmann, R. Heiderhoff, T. Riedl: Stress Management in Thin-Film Gas-Permeation Barriers *ACS Appl. Mater. & Interfaces 8, 4056 (2016)*

10. A. Behrendt, C. Friedenberger, T. Gahlmann, S. Trost, T. Becker, K. Zilberberg, A. Polywka, P. Görrn, and T. Riedl: Highly robust transparent and conductive gas diffusion barriers based on tin oxide *Adv. Mater. 27, 5961 (2015)*

Conference Contributions

1. K. O. Brinkmann, T. Gahlmann, J. He, C. Tückmantel, M. Theisen, T. Becker, J. Bahr, J. Song, J. Qu, and T. Riedl: Intrinsic ALD Barriers Enable Processing on Top of Perovskite Solar Cells from Environmentally Friendly Solvents *Proceedings of nanoGe Fall Meeting 19 (NGFM19), Berlin (Germany) (2019)*

2. T. Gahlmann, K. O. Brinkmann, C. Tückmantel, T. Becker, J. He, J. Bahr, C. Kreusel, and T. Riedl: Aqueous processing of Ag-nanowire electrodes on top of semi-transparent perovskite solar cells *SPIE Optics and Photonics, San Diego (USA), 110940D (2019)*

3. T. Becker, T. Gahlmann, N. Köhler, F. Zimmermann, F. Göbelsmann, K. O. Brinkmann, and T. Riedl: Suppressing the photo-induced degradation of inverted non-fullerene organic solar cells *MRS Fall Meeting, Boston (USA), EP05.03.50 (2018)*

4. K. O. Brinkmann, J. Zhao, T. Hu, N. Pourdavoud, T. Gahlmann, R. Heiderhoff, S. Olthof, K. Meerholz, A. Polywka, B. Cheng, Y Chen, P. Görrn and T. Riedl: Self-Encapsulating Air-Resilent Semitransparent Perovskite Solar Cells with Superior Thermal Stability Beyond 2000h *MRS Spring Meeting, Phoenix (USA) ES1.2.10 (2017)*

5. K. O. Brinkmann, J. Zhao, T. Hu, T. Becker, N. Pourdavoud, S. Olthof, K. Meerholz, L. Hoffmann, T. Gahlmann, R. Heiderhoff, M. Oszajca, D. Rogalla, N. A. Lüchinger, Y. Chen, B. Cheng, T. Riedl: Pushing the lifetime of perovskite solar cell beyond 4500 h by the use of impermeable tin oxide electron extraction layers *SPIE Optics and Photonics, San Diego (USA) 10363-32 (2017)*

6. K. O. Brinkmann, T. Hu, T. Becker, N. Pourdavoud, J. Zhao, R. Heiderhoff, T. Gahlmann, Z. Huang, S. Olthof, K. Meerholz, D. Többens, B. Cheng, Y. Chen, T. Riedl: Interface Electronic Structure of ALD-Grown SnOx and MAPbI3 in In-Free

Perovskite Solar Cell *10th International Summit on Stability of Organic and Perovskite Solar Cells (ISOS-10), (Malta) ID13 (2017)*

7. K. Brinkmann, N. Pourdavoud, T. Becker, T. Hu, J. Zhao, Y. Chen, S. Olthof, K. Meerholz, L. Hoffmann, T. Gahlmann, R. Heiderhoff, M. Oszajca, N. Luechinger, and T. Riedl: Suppressed Decomposition of Organo-Metal Halide Perovskites by Impermeable Electron Extraction Layers in Inverted Solar Cells (Best Poster Award Winner) *MRS Fall Meeting, Boston (USA) ES3.9.09 (2016)*

8. A. Behrendt, T. Becker, S. Trost, T. Gahlmann, and T. Riedl: Transparent and Conductive Thin-Film Permeation Barriers - Towards Self-Encapsulating Organic Opto-Electronics (Invited) *16th Int. Meeting Inf. Display (IMID 2016), A57-4, Jeju (Korea) (2016)*

9. A. Behrendt, T. Gahlmann, S. Trost, A. Polywka, P. Görrn, and T. Riedl: Transparent conductive thin-film encapsulation layers *Proc. SPIE, San Diego(USA) 9567, 95671C (2015)*

10. A. Behrendt, C. Friedenberger, T. Gahlmann, S. Trost, A. Polywka, P. Görrn, T. Riedl: Transparent conductive gas diffusion barriers *25th Eur. Symp. on Reliability of Electr. Dev. and Failure Analysis, Berlin (Germany), Tue-C-13:50 (2014)*

11. A. Behrendt, T. Gahlmann, M. Fakhri, S. Trost, K. Zilberberg, and T. Riedl: Highly robust transparent conductive gas diffusion barriers based on tin oxide prepared by low-temperature atomic layer deposition *MRS Fall Meeting, Boston (USA) M1.06 (2013)*

Supervised Student Thesis

1. Katharina Galla: Ink-Jet-Druck von Silber-Gittern als transparente Elektroden für organische Solarzellen
Master Thesis (2016)

2. Roman Fichtner: Herstellung und Charakterisierung von transparenten Silbernanodraht Elektroden auf Polyethylen-Therephtalat-Folien
Bachelor Thesis (2016)

3. Ioannis Papadopoulos: Sprühbeschichtung transparenter, leitfähiger Elektroden auf Basis von Silber-Nanodrähten für semi-transparente organische Solarzellen
Bachelor Thesis (2016)

4. Oliver Koch: Flüssigprozessierte Ladungsträgerextraktionsschichten für Rolle-zu-Rolle prozessierbare organische Solarzellen
Bachelor Thesis (2017)

5. Niklas Köhler: Metalloxid-basierte Elektronenextraktionsschichten für fullerenfreie organische Solarzellen
Master Thesis (2018)

6. Manuel Runkel: Flüssigprozessierte Metalloxid basierte Ladungsträgerextraktionsschichten für fullerenfreie organische Solarzellen
Master Thesis (2019)

7. Florian Zimmermann: Abscheidung von Indiumoxid mittels ALD für Perowskitsolarzellen
Master Thesis (2020)

8. Berhad Sammu Hussein: Oxidische Hybridstrukturen als Gasdiffusionsbarrieren
Bachelor Thesis (2021)

Bibliography

[1] K. L. Chopra, P. D. Paulson, V. Dutta, *Progress in Photovoltaics: Research and Applications* **2004**, *12*, 69–92.

[2] Y. Xu, J. Wang, L. Sun, H. Huang, J. Han, H. Huang, L. Zhai, C. Zou, *Journal of Materials Chemistry C* **2021**, *9*, 9102–9123.

[3] S.-P. Cho, S.-I. Na, S.-S. Kim, *Solar Energy Materials and Solar Cells* **2019**, *196*, 1–8.

[4] M. B. Upama, M. Wright, N. K. Elumalai, M. A. Mahmud, D. Wang, C. Xu, A. Uddin, *ACS Photonics* **2017**, *4*, 2327–2334.

[5] M. Mujahid, C. Chen, J. Zhang, C. Li, Y. Duan, *InfoMat* **2021**, *3*, 101–124.

[6] A. Colsmann, A. Puetz, A. Bauer, J. Hanisch, E. Ahlswede, U. Lemmer, *Advanced Energy Materials* **2011**, *1*, 599–603.

[7] W. Cao, J. Li, H. Chen, J. Xue, *Journal of Photonics for Energy* **2014**, *4*, 040990.

[8] S. Uekusa, R. Nakano, K. Yokogawa, *Japanese Journal of Applied Physics* **1994**, *33*, 302.

[9] W. F. Wu, B. S. Chiou, *Applied Surface Science* **1993**, *68*, 497–504.

[10] V. K. Jain, A. P. Kulshreshtha, *Solar Energy Materials* **1981**, *4*, 151–158.

[11] R. Søndergaard, M. Hösel, D. Angmo, T. T. Larsen-Olsen, F. C. Krebs, *Materials Today* **2012**, *15*, 36–49.

[12] S. M. Bergin, Y.-H. Chen, A. R. Rathmell, P. Charbonneau, Z.-Y. Li, B. J. Wiley, *Nanoscale* **2012**, *4*, 1996.

[13] J. Y. Lee, S. T. Connor, Y. Cui, P. Peumans, *Nano Letters* **2008**, *8*, 689–692.

[14] S. J. Lee, Y. H. Kim, J. K. Kim, H. Baik, J. H. Park, J. Lee, J. Nam, J. H. Park, T. W. Lee, G. R. Yi, J. H. Cho, *Nanoscale* **2014**, *6*, 11828–11834.

[15] D. J. Kim, H. I. Shin, E. H. Ko, K. H. Kim, T. W. Kim, H. K. Kim, *Scientific Reports* **2016**, *6*, 1–12.

[16] Y. J. Kang, D. G. Kim, J. K. Kim, W. Y. Jin, J. W. Kang, *Organic Electronics: physics materials applications* **2014**, *15*, 2173–2177.

[17] S. B. Kang, Y. J. Noh, S. I. Na, H. K. Kim, *Solar Energy Materials and Solar Cells* **2014**, *122*, 152–157.

[18] J. Jung, H. Cho, R. Yuksel, D. Kim, H. Lee, J. Kwon, P. Lee, J. Yeo, S. Hong, H. E. Unalan, S. Han, S. H. Ko, *Nanoscale* **2019**, *11*, 20356–20378.

[19] A. Al-Ashouri, E. Köhnen, B. Li, A. Magomedov, H. Hempel, P. Caprioglio, J. A. Márquez, A. B. M. Vilches, E. Kasparavicius, J. A. Smith, N. Phung, D. Menzel, M. Grischek, L. Kegelmann, D. Skroblin, C. Gollwitzer, T. Malinauskas, M. Jošt, G. Matič, B. Rech, R. Schlatmann, M. Topič, L. Korte, A. Abate, B. Stannowski, D. Neher, M. Stolterfoht, T. Unold, V. Getautis, S. Albrecht, *Science* **2020**, *370*, 1300–1309.

[20] M. Hrabal, I. Zhivkov, P. Guricova, G. Dobrikov, R. Yordanov, M. Vala, *Proceedings of the International Spring Seminar on Electronics Technology* **2019**, 1–5.

[21] Y. Zuo, X. Shi, X. Zhou, X. Xu, J. Wang, P. Chen, X. Sun, H. Peng, *Advanced Functional Materials* **2020**, *30*, 2005200.

[22] L. Zhang, P. H. Sit, *Journal of Physical Chemistry C* **2015**, *39*, 22370–22378.

[23] J. S. Manser, M. I. Saidaminov, J. A. Christians, O. M. Bakr, P. V. Kamat, *Accounts of Chemical Research* **2016**, *49*, 33–338.

[24] T. Leijtens, G. E. Eperon, N. K. Noel, S. N. Habisreutinger, A. Petrozza, H. J. Snaith, *Advanced Energy Materials* **2015**, *5*, 1500963.

[25] A. Behrendt, C. Friedenberger, T. Gahlmann, S. Trost, T. Becker, K. Zilberberg, A. Polywka, P. Görrn, T. Riedl, *Advanced Materials* **2015**, *27*, 5961.

[26] K. Brinkmann, J. Zhao, N. Pourdavoud, T. Becker, T. Hu, S. Olthof, K. Meerholz, L. Hoffmann, T. Gahlmann, R. Heiderhoff, M. F. Oszajca, N. A. Luechinger, D. Rogalla, Y. Chen, B. Cheng, T Riedl, *Nature Communications* **2017**, *8*, 13938.

[27] John Daintith, *A Dictionary of Chemistry*, Oxford University Press, **2008**.

[28] G. Haacke, *Journal of Applied Physics* **1976**, *47*, 4086–4089.

[29] J. De Wit, *Journal of Solid State Chemistry* **1977**, *20*, 143–148.

[30] W. Seiler, M. Nistor, C. Hebert, J. Perrière, *Solar Energy Materials and Solar Cells* **2013**, *116*, 34–42.

[31] J. A. Libera, J. N. Hryn, J. W. Elam, *Chemistry of Materials* **2011**, *23*, 2150–2158.

[32] G. B. González, T. O. Mason, J. S. Okasinski, T. Buslaps, V. Honkimäki, *Journal of the American Ceramic Society* **2012**, *95*, (Ed.: P. Gouma), 809–815.

[33] G. Frank, H. Köstlin, *Applied Physics A Solids and Surfaces* **1982**, *27*, 197–206.

[34] R Latz, K Michael, M Scherer, *Japanese Journal of Applied Physics* **1991**, *30*, L149–L151.

[35] H. Kim, C. M. Gilmore, A. Piqué, J. S. Horwitz, H. Mattoussi, H. Murata, Z. H. Kafafi, D. B. Chrisey, *Journal of Applied Physics* **1999**, *86*, 6451–6461.

[36] H. H. Park, *Electronic Materials Letters* **2021**, *17*, 18–32.

[37] S. Nanowire, L. Hu, H. S. Kim, J.-y. Lee, P. Peumans, Y. Cui, *ACS nano* **2010**, *4*, 2955–2963.

[38] R. Banica, D. Ursu, P. Svera, C. Sarvas, S. F. Rus, S. Novaconi, A. Kellenberger, A. V. Racu, T. Nyari, N. Vaszilcsin, *Particulate Science and Technology* **2016**, *34*, 217–222.

[39] F. Selzer, N. Weiß, D. Kneppe, L. Bormann, C. Sachse, N. Gaponik, A. Eychmüller, K. Leo, L. Müller-Meskamp, *Nanoscale* **2015**, *7*, 2777–2783.

[40] W. Li, H. Zhang, S. Shi, J. Xu, X. Qin, Q. He, K. Yang, W. Dai, G. Liu, Q. Zhou, H. Yu, S. R. P. Silva, M. Fahlman, *Journal of Materials Chemistry C* **2020**, *8*, 4636–4674.

[41] K. Zilberberg, F. Gasse, R. Pagui, A. Polywka, A. Behrendt, S. Trost, R. Heiderhoff, P. Görrn, T. Riedl, *Advanced Functional Materials* **2014**, *24*, 1671–1678.

[42] F. Guo, N. Li, V. V. Radmilović, V. R. Radmilović, M. Turbiez, E. Spiecker, K. Forberich, C. J. Brabec, *Energy & Environmental Science* **2015**, *8*, 1690–1697.

[43] X. Dong, P. Shi, L. Sun, J. Li, F. Qin, S. Xiong, T. Liu, X. Jiang, Y. Zhou, *Journal of Materials Chemistry A* **2019**, *7*, 1989–1995.

[44] K. W. Park, H. S. Jeong, J. H. Park, G. Deressa, Y. T. Jeong, K. T. Lim, J. H. Park, S. H. Lee, J. S. Kim, *Journal of Luminescence* **2015**, *165*, 216–219.

[45] S. Duan, L. Zhang, Z. Wang, C. Li, *RSC Adv.* **2015**, *5*, 95280–95286.

[46] C. Zhao, Y. Zhou, S. Gu, S. Cao, J. Wang, M. Zhang, Y. Wu, D. Kong, *ACS Applied Materials and Interfaces* **2020**, *12*, 47902–47910.

[47] Y. Zhou, C. Zhao, J. Wang, Y. Li, C. Li, H. Zhu, S. Feng, S. Cao, D. Kong, *ACS Materials Letters* **2019**, *1*, 511–518.

[48] G. Liang, H. Hu, L. Liao, Y. He, *Adv. Electron. Mater.* **2017**, *3*, 1600535.

[49] C.-H. Liu, X. Yu, *Nanoscale Research Letters* **2011**, *6*, 75.

[50] V. Scardaci, R. Coull, P. E. Lyons, D. Rickard, J. N. Coleman, *Small* **2011**, *7*, 2621–2628.

[51] J. W. Strutt, *The Theory of Sound*, Cambridge University Press, **2011**.

[52] R. Rajan, A. Pandit, *Ultrasonics* **2001**, *39*, 235–255.

[53] S. Slegers, M. Linzas, J. Drijkoningen, J. D'Haen, N. Reddy, W. Deferme, *Coatings* **2017**, *7*, 208.

[54] K. Yasuda, Y. Bando, S. Yamaguchi, M. Nakamura, A. Oda, Y. Kawase, *Ultrasonics Sonochemistry* **2005**, *12*, 37–41.

[55] J. Kim, J. Kim, K. Ha, M. Kim, *Japanese Journal of Applied Physics* **2016**, *55*, 07KE03.

[56] D. Son, J. Kang, O. Vardoulis, Y. Kim, N. Matsuhisa, J. Y. Oh, J. W. To, J. Mun, T. Katsumata, Y. Liu, A. F. McGuire, M. Krason, F. Molina-Lopez, J. Ham, U. Kraft, Y. Lee, Y. Yun, J. B. Tok, Z. Bao, *Nature Nanotechnology* **2018**, *13*, 1057–1065.

[57] Y. Zhou, S. Cao, J. Wang, H. Zhu, J. Wang, S. Yang, X. Wang, D. Kong, *ACS Applied Materials & Interfaces* **2018**, *10*, 44760–44767.

[58] L. Wang, L. Xiao, H. Gu, H. Sun, *Advanced Optical Materials* **2019**, *7*, 1–30.

[59] W. A. D. M. Jayathilaka, A. Chinnappan, J. N. Tey, J. Wei, S. Ramakrishna, *Journal of Materials Chemistry C* **2019**, *7*, 5553–5572.

[60] X. Zhang, F. Wang, *APL Materials* **2021**, *9*.

[61] C. Larson, B. Peele, S. Li, S. Robinson, M. Totaro, L. Beccai, B. Mazzolai, R. Shepherd, *Science* **2016**, *351*, 1071–1074.

[62] E. H. Kim, H. Han, S. Yu, C. Park, G. Kim, B. Jeong, S. W. Lee, J. S. Kim, S. Lee, J. Kim, J. U. Park, W. Shim, C. Park, *Advanced Science* **2019**, *6*.

[63] G. O. Müller, *Physica Status Solidi (a)* **1984**, *81*, 597–608.

[64] P Benalloul in Electroluminescence, (Eds.: S. Shionoya, H. Kobayashi), Springer Berlin Heidelberg, Berlin, Heidelberg, **1989**, pp. 36–43.

[65] V. Maxia, C. Muntoni, M. Murgia, *Lettere al Nuovo Cimento* **1971**, *1*, 151–156.

[66] B. Allieri, S. Peruzzi, L. Antonini, A. Speghini, M. Bettinelli, D. Consolini, G. Dotti, L. E. Depero, *Journal of Alloys and Compounds* **2002**, *341*, 79–81.

[67] J. Ibañez, E. Garcia, L. Gil, M. Mollar, B. Marí, *Displays* **2007**, *28*, 112–117.

[68] L. N. Tripathi, B. R. Chaubey, C. P. Mishra, *Pramana* **1981**, *16*, 155–164.

[69] M. K. Jayaraj, C. P. G. Vallabhan, *Journal of The Electrochemical Society* **1991**, *138*, 1512–1516.

[70] J. L. Gillson, F. J. Darnell, *Physical Review* **1962**, *125*, 149–158.

[71] H. Yang, P. H. Holloway, B. B. Ratna, *Journal of Applied Physics* **2003**, *93*, 586–592.

[72] R. Schmidt, A. Schmuck, Luminous elements with an electroluminescent arrangement and method for producing a luminous element. *European Patent WO 2013/091604*, **2013**.

[73] A. C. Harris, I. L. Weatherall, *Journal of the Royal Society of New Zealand* **1990**, *20*, 253–259.

[74] C. S. McCamy, *Color Research & Application* **1992**, *17*, 142–144.

[75] B. Kippelen, J.-L. Brédas, *Energy & Environmental Science* **2009**, *2*, 251.

[76] W. Tress, *Organic Solar Cells*, Springer International Publishing, Cham, **2014**.

[77] H Klumbies in, **2013**.

[78] F. C. Krebs, J. Fyenbo, M. Jørgensen, *Journal of Materials Chemistry* **2010**, *20*, 8994–9001.

[79] M Hösel, D Angmo, F. C. Krebs in *Handbook of Organic Materials for Optical and (Opto)electronic Devices*, (Ed.: O. Ostroverkhova), Woodhead Publishing Series in Electronic and Optical Materials, Woodhead Publishing, **2013**, pp. 473–507.

[80] S. Li, L. Ye, W. Zhao, S. Zhang, S. Mukherjee, H. Ade, J. Hou, *Advanced Materials* **2016**, *28*, 9423–9429.

[81] A. Armin, W. Li, O. J. Sandberg, Z. Xiao, L. Ding, J. Nelson, D. Neher, K. Vandewal, S. Shoaee, T. Wang, H. Ade, T. Heumüller, C. Brabec, P. Meredith, *Advanced Energy Materials* **2021**, *11*, 2003570.

[82] W. Zhao, S. Li, H. Yao, S. Zhang, Y. Zhang, B. Yang, J. Hou, *Journal of the American Chemical Society* **2017**, *139*, 7148–7151.

[83] B. Fan, D. Zhang, M. Li, W. Zhong, Z. Zeng, L. Ying, F. Huang, Y. Cao, *Science China Chemistry* **2019**, *62*, 746–752.

[84] Q. Liu, Y. Jiang, K. Jin, J. Qin, J. Xu, W. Li, J. Xiong, J. Liu, Z. Xiao, K. Sun, S. Yang, X. Zhang, L. Ding, *Science Bulletin* **2020**, *65*, 272–275.

[85] L. Perdigón-Toro, H. Zhang, A. Markina, J. Yuan, S. M. Hosseini, C. M. Wolff, G. Zuo, M. Stolterfoht, Y. Zou, F. Gao, D. Andrienko, S. Shoaee, D. Neher, *Advanced Materials* **2020**, *32*, 1906763.

[86] A. Karki, A. J. Gillett, R. H. Friend, T. Nguyen, *Advanced Energy Materials* **2021**, *11*, 2003441.

[87] A. Kojima, K. Teshima, Y. Shirai, T. Miyasaka, *Journal of the American Chemical Society* **2009**, *131*, 6050–6051.

[88] J.-H. Im, C.-R. Lee, J.-W. Lee, S.-W. Park, N.-G. Park, *Nanoscale* **2011**, *3*, 4088.

[89] W. E. I. Sha, X. Ren, L. Chen, W. C. H. Choy, *Applied Physics Letters* **2015**, *106*, 221104.

[90] J. Jeong, M. Kim, J. Seo, H. Lu, P. Ahlawat, A. Mishra, Y. Yang, M. A. Hope, F. T. Eickemeyer, M. Kim, Y. J. Yoon, I. W. Choi, B. P. Darwich, S. J. Choi, Y. Jo, J. H. Lee, B. Walker, S. M. Zakeeruddin, L. Emsley, U. Rothlisberger, A. Hagfeldt, D. S. Kim, M. Grätzel, J. Y. Kim, *Nature* **2021**, *592*, 381–385.

[91] N.-G. Park, *Materials Today* **2015**, *18*, 65–72.

[92] T. Bu, J. Li, H. Li, C. Tian, J. Su, G. Tong, L. K. Ono, C. Wang, Z. Lin, N. Chai, X.-L. Zhang, J. Chang, J. Lu, J. Zhong, W. Huang, Y. Qi, Y.-B. Cheng, F. Huang, *Science* **2021**, *372*, 1327–1332.

[93] S. Zhang, X. Liu, T. Lin, P. He, *Journal of Materials Science: Materials in Electronics* **2019**, *30*, 18702–18709.

[94] A. Kiran Kumar, C. wan Bae, L. Piao, S.-H. Kim, *Materials Research Bulletin* **2013**, *48*, 2944–2949.

[95] Y. Kim, Y. E. Sul, H. Kang, Y. Choi, H. S. Lim, S. Lee, L. Pu, G.-R. Yi, S. M. Cho, J. H. Cho, *Nanoscale* **2018**, *10*, 18627–18634.

[96] R. D. Deegan, O. Bakajin, T. F. Dupont, G. Huber, S. R. Nagel, T. A. Witten, *Nature* **1997**, *389*, 827–829.

[97] T. Gahlmann, K. O. Brinkmann, T. Becker, C. Tückmantel, C. Kreusel, F. V. Hassend, S. Weber, T. Riedl, *Advanced Energy Materials* **2020**, *10*, 1903897.

[98] G. Groetsch, R. Schmidt, T. Tschorn, Composition for producing an electrically conductive layer, in particular for an electroluminescence device. *World Intellectual Property Organization WO/2019/105726*, **2019**.

[99] W. Zhao, D. Qian, S. Zhang, S. Li, O. Inganäs, F. Gao, J. Hou, *Advanced Materials* **2016**, 4734–4739.

[100] K. O. Brinkmann, J. He, F. Schubert, J. Malerczyk, C. Kreusel, F. van gen Hassend, S. Weber, J. Song, J. Qu, T. Riedl, *ACS Applied Materials and Interfaces* **2019**, *11*, 40172 –40179.

[101] A. Babayigit, J. D'Haen, H. G. Boyen, B. Conings, *Joule* **2018**, *2*, 1205 –1209.

[102] B. Conings, A. Babayigit, M. T. Klug, S. Bai, N. Gauquelin, N. Sakai, J. T. W. Wang, J. Verbeeck, H. G. Boyen, H. J. Snaith, *Advanced Materials* **2016**, *28*, 10701 –10709.

[103] M. Zhang, J. S. Yun, Q. Ma, J. Zheng, C. F. J. Lau, X. Deng, J. Kim, D. Kim, J. Seidel, M. A. Green, S. Huang, A. W. Ho-Baillie, *ACS Energy Letters* **2017**, *2*, 438 –444.

[104] T. Gahlmann, T. Tschorn, T. Maschwitz, L. Gomell, T. Haeger, G. Grötsch, R. Heiderhoff, T. Riedl, *ACS Applied Materials & Interfaces* **2021**, *13*, 28514–28520.

[105] J. Cameron, P. J. Skabara, *Materials Horizons* **2020**, *7*, 1759–1772.

[106] C. Ionescu-Zanetti, A. Mechler, S. A. Carter, R. Lal, *Advanced Materials* **2004**, *16*, 385–389.

[107] R. K. Gupta, B. Bills, M. Dubey, D. Galipeau, Q. H. Fan, *IEEE International Conference on Electro Information Technology* **2013**, 2–6.

[108] H. Lu, M. Huang, K. S. Shen, J. Zhang, S. Q. Xia, C. Dong, Z. G. Xiong, T. Zhu, D. P. Wu, B. Zhang, X. Z. Zhang, *Nanoscale Research Letters* **2018**, *13*.

[109] C. Tsakonas, S. Wakeham, W. M. Cranton, M. Thwaites, G. Boutaud, C. Farrow, D. C. Koutsogeorgis, R. Ranson, *IEEE Journal of the Electron Devices Society* **2016**, *4*, 22–29.

[110] M. Leskelä, M. Mattinen, M. Ritala, *Journal of Vacuum Science & Technology B* **2019**, *37*, 030801.

[111] L. Wen, N. Liu, S. Wang, H. Zhang, W. Zhao, Z. Yang, Y. Wang, J. Su, L. Li, F. Long, Z. Zou, Y. Gao, *Optics Express* **2016**, *24*, 23419.

[112] C. D. Brubaker, K. N. Newcome, G. K. Jennings, D. E. Adams, *Journal of Materials Chemistry C* **2019**, *7*, 5573–5578.

[113] M. Kaltenbrunner, M. S. White, E. D. Głowacki, T. Sekitani, T. Someya, N. S. Sariciftci, S. Bauer, *Nature Communications* **2012**, *3*, 770.

[114] S. R. Forrest, *Nature* **2004**, *428*, 911–918.

[115] H. Ma, H.-L. Yip, F. Huang, A. K.-Y. Jen, *Advanced Functional Materials* **2010**, *20*, 1371–1388.

[116] W. Guo, Z. Xu, F. Zhang, S. Xie, H. Xu, X. Y. Liu, *Advanced Functional Materials* **2016**, *26*, 8855–8884.

[117] M. Giannouli, *International Journal of Photoenergy* **2021**, *2021*, (Ed.: K. Sudhakar), 1–19.

[118] L. Shi, Y. Cui, Y. Gao, W. Wang, Y. Zhang, F. Zhu, Y. Hao, *Nanomaterials* **2018**, *8*, 473.

[119] G. Sun, M. Shahid, Z. Fei, S. Xu, F. D. Eisner, T. D. Anthopolous, M. A. McLachlan, M. Heeney, *Materials Chemistry Frontiers* **2019**, *3*, 450–455.

[120] S. Lee, J. Jang, T. Park, Y. M. Park, J. S. Park, Y. K. Kim, H. K. Lee, E. C. Jeon, D. K. Lee, B. Ahn, C. H. Chung, *ACS Applied Materials and Interfaces* **2020**, *12*, 6169–6175.

[121] B.-H. Jiang, H.-E. Lee, J.-H. Lu, T.-H. Tsai, T.-S. Shieh, R.-J. Jeng, C.-P. Chen, *ACS Applied Materials & Interfaces* **2020**, *12*, 39496–39504.

[122] X. Lu, L. Cao, X. Du, H. Lin, C. Zheng, Z. Chen, B. Sun, S. Tao, *Advanced Optical Materials* **2021**, *9*, 2100064.

[123] Z. M. Beiley, M. G. Christoforo, P. Gratia, A. R. Bowring, P. Eberspacher, G. Y. Margulis, C. Cabanetos, P. M. Beaujuge, A. Salleo, M. D. McGehee, *Advanced Materials* **2013**, *25*, 7020–7026.

[124] H. Lu, J. Lin, N. Wu, S. Nie, Q. Luo, C.-Q. Ma, Z. Cui, *Applied Physics Letters* **2015**, *106*, 093302.

[125] M. Makha, P. Testa, S. B. Anantharaman, J. Heier, S. Jenatsch, N. Leclaire, J.-N. Tisserant, A. C. Véron, L. Wang, F. Nüesch, R. Hany, *Science and Technology of Advanced Materials* **2017**, *18*, 68–75.

[126] S. Trost, K. Zilberberg, A. Behrendt, T. Riedl, *Journal of Materials Chemistry* **2012**, *22*, 16224.

[127] L. Huo, T. Liu, X. Sun, Y. Cai, A. J. Heeger, Y. Sun, *Advanced Materials* **2015**, *27*, 2938–2944.

[128] X. Yang, J. Loos, S. C. Veenstra, W. J. H. Verhees, M. M. Wienk, J. M. Kroon, M. A. J. Michels, R. A. J. Janssen, *Nano Letters* **2005**, *5*, 579–583.

[129] S. H. Park, A. Roy, S. Beaupré, S. Cho, N. Coates, J. S. Moon, D. Moses, M. Leclerc, K. Lee, A. J. Heeger, *Nature Photonics* **2009**, *3*, 297–302.

[130] B. Qi, J. Wang, *Physical Chemistry Chemical Physics* **2013**, *15*, 8972.

[131] J. M. Cho, S. K. Lee, S.-J. Moon, J. Jo, W. S. Shin, *Current Applied Physics* **2014**, *14*, 1144–1148.

[132] P. Romero-Gomez, R. Betancur, A. Martinez-Otero, X. Elias, M. Mariano, B. Romero, B. Arredondo, R. Vergaz, J. Martorell, *Solar Energy Materials and Solar Cells* **2015**, *137*, 44–49.

[133] G. Ji, Y. Wang, Q. Luo, K. Han, M. Xie, L. Zhang, N. Wu, J. Lin, S. Xiao, Y.-Q. Li, L.-Q. Luo, C.-Q. Ma, *ACS Applied Materials & Interfaces* **2018**, *10*, 943–954.

[134] M. Koppitz, E. Wegner, T. Rödlmeier, A. Colsmann, *Energy Technology* **2018**, *6*, 1275–1282.

[135] X. Sun, W. Zha, T. Lin, J. Wei, I. Ismail, Z. Wang, J. Lin, Q. Luo, C. Ding, L. Zhang, Z. Su, B. Chu, D. Zhang, C.-Q. Ma, *Journal of Materials Science* **2020**, *55*, 14893–14906.

[136] NREL, NREL Best Research-Cell Efficiencies, **2021**.

[137] J. Idígoras, F. J. Aparicio, L. Contreras-Bernal, S. Ramos-Terrón, M. Alcaire, J. R. Sánchez-Valencia, A. Borras, Á. Barranco, J. A. Anta, *ACS Applied Materials and Interfaces* **2018**, *10*, 11587–11594.

[138] K. A. Bush, A. F. Palmstrom, Z. J. Yu, M. Boccard, R. Cheacharoen, J. P. Mailoa, D. P. McMeekin, R. L. Hoye, C. D. Bailie, T. Leijtens, I. M. Peters, M. C. Minichetti, N. Rolston, R. Prasanna, S. Sofia, D. Harwood, W. Ma, F. Moghadam, H. J. Snaith, T. Buonassisi, Z. C. Holman, S. F. Bent, M. D. McGehee, *Nature Energy* **2017**, *2*, 17009.

[139] I. S. Kim, D. H. Cao, D. B. Buchholz, J. D. Emery, O. K. Farha, J. T. Hupp, M. G. Kanatzidis, A. B. Martinson, *Nano Letters* **2016**, *16*, 7786–7790.

[140] K. O. Brinkmann, T. Gahlmann, T. Riedl, *Solar RRL* **2019**, *1900332*.

[141] B. Conings, J. Drijkoningen, N. Gauquelin, A. Babayigit, J. D'Haen, L. D'Olieslaeger, A. Ethirajan, J. Verbeeck, J. Manca, E. Mosconi, F. De Angelis, H. G. Boyen, *Advanced Energy Materials* **2015**, *5*, 1500477.

[142] J. W. Shim, H. Cheun, J. Meyer, C. Fuentes-Hernandez, A. Dindar, Y. H. Zhou, D. K. Hwang, A. Kahn, B. Kippelen, *Applied Physics Letters* **2012**, *101*, 073303.

[143] E. R. Viana, J. C. González, G. M. Ribeiro, A. G. De Oliveira, *Journal of Physical Chemistry C* **2013**, *117*, 7844–7849.

[144] V. Brinzari, *Applied Surface Science* **2017**, *411*, 437 –448.

[145] A. Dixit, R. P. Panguluri, C. Sudakar, P. Kharel, P. Thapa, I. Avrutsky, R. Naik, G. Lawes, B. Nadgorny, *Applied Physics Letters* **2009**, *94*, 252105.

[146] S. Trost, T. Becker, K. Zilberberg, A. Behrendt, A. Polywka, R. Heiderhoff, P. Görrn, T. Riedl, *Scientific Reports* **2015**, *5*, 7765.

[147] J. Cheng, Y. Li, M. Plissonneau, J. Li, J. Li, R. Chen, Z. Tang, L. Pautrot-d'Alençon, T. He, M. Tréguer-Delapierre, M. H. Delville, *Scientific Reports* **2018**, *8*, 14136.

[148] T. Sasabayashi, P. K. Song, Y. Shigesato, K. Utsumi, A. Kaijo, A. Mitsui, *MRS Proceedings* **2001**, *666*, F2.4.

[149] A. Behrendt, J. Meyer, P. Van De Weijer, T. Gahlmann, R. Heiderhoff, T. Riedl, *ACS Applied Materials and Interfaces* **2016**, *8*, 4056.

[150] L. Hoffmann, K. O. Brinkmann, J. Malerczyk, D. Rogalla, T. Becker, D. Theirich, I. Shutsko, P. Görrn, T. Riedl, *ACS Applied Materials & Interfaces* **2018**, *10*, 6006–6013.

[151] F. Zimmermann, *Abscheidung von Indiumoxid mittels ALD für Perowskitsolarzellen* **2020**, Master Thesis.

[152] P. F. Carcia, R. S. McLean, M. H. Reilly, M. D. Groner, S. M. George, *Applied Physics Letters* **2006**, *89*, 031915.